

Structural, Optical and Transport Properties of Copper Chalcogenide Nanocrystal Superlattices

Dissertation

der Mathematisch-Naturwissenschaftlichen Fakultät
der Eberhard Karls Universität Tübingen
zur Erlangung des Grades eines
Doktors der Naturwissenschaften (Dr. rer. nat.)

vorgelegt von

Sonam Maiti

aus Haldia/Indien

Tübingen

2019

Gedruckt mit Genehmigung der Mathematisch-Naturwissenschaftlichen Fakultät der
Eberhard Karls Universität Tübingen.

Tag der mündlichen Qualifikation:	28.05.2019
Dekan:	Prof. Dr. Wolfgang Rosenstiel
1. Berichterstatter:	Prof. Dr. Frank Schreiber
2. Berichterstatter:	Prof. Dr. Martin Oettel

Table of Contents

Preface.....	5
Abstract.....	7
Zusammenfassung.....	9
Part I.....	11
Scientific Background.....	11
1. Introduction.....	12
1.1. What are nanocrystals?.....	13
1.2. Why are colloidal nanocrystals interesting?.....	14
1.3. Copper chalcogenide nanocrystals	17
1.4. Coupled organic-inorganic nanostructures (COINs)	20
1.5. Self-Assembly of Nanocrystals.....	22
1.6. Characterization of NCs and their superlattices.....	25
1.7. Grazing incidence small angle X-ray scattering (GISAXS).....	26
1.8. Charge transport in NCs superlattices.....	29
1.9. Photodetection.....	32
1.10. Application in Vapor Sensing.....	34
Part II	36
Results and discussion	36
2. Publication 1	37
Electronically Coupled, Two-Dimensional Assembly of Cu _{1.1} S Nanodiscs for Selective Vapor Sensing Applications	37
3. Publication 2	52
Dye-Sensitized Ternary Copper Chalcogenide Nanocrystals: Optoelectronic Properties, Air Stability and Photosensitivity	52
4. Publication 3	66
<i>In Situ</i> Formation of Electronically Coupled Superlattice of Cu _{1.1} S Nanodiscs at the Liquid/Air Interface	66
Conclusions.....	75
Part III.....	77
Collaborated Publications	77

5. Collaborated Publication 1.....	78
Understanding the Formation of Conductive Mesocrystalline Superlattices with Cubic PbS Nanocrystals at the Liquid/Air Interface.....	78
6. Collaborated Publication 2.....	81
Correlated, Dual-Beam Optical Gating in Coupled Organic–Inorganic Nanostructures	81
Appendix A.....	84
Appendix B.....	89
Appendix C.....	97
List of Symbols and Abbreviations.....	104
List of Tables	107
List of Figures	108
List of Publications	113
Acknowledgments.....	114
References.....	116

Preface

The majority of experimental work in this dissertation has been carried out between November 2016 and March 2019 in the Institute of Applied Physics and Institute of Physical and Theoretical Chemistry at the University of Tübingen in the group of Prof. Dr. Frank Schreiber and Dr. Marcus Scheele. The X-ray scattering measurements have been performed at the P08, The Deutsches Elektronen-Synchrotron (DESY) and vapor sensing measurements have been carried out in the Institute of Electronic and Sensor Materials at Freiberg University of Mining and Technology in the group of Prof. Dr. Yvonne Joseph.

The theoretical section in this dissertation is mainly excerpted from:

(i) Boris I. Shklovskii and Alexei L. Efros, “Electronic Properties of Doped Semiconductors”, Springer-Verlag Berlin Heidelberg, **1984**.

(ii) Winfried Mönch, “Semiconductor Surfaces and Interfaces”, Springer-Verlag Berlin Heidelberg, New York, **1993**.

(iii) Leonid I. Glazman and Michael Pustilnik, “Nanophysics: Coherence and Transport”, Vol 81, 1st Ed., Elsevier Science, San Diego, CA, **2005**.

as well as from the following research and review articles:

(i) Coughlan, C.; Ibáñez, M.; Dobrozhan, O.; Singh, A.; Cabot, A.; Ryan, K.M. Compound Copper Chalcogenide Nanocrystals. *Chem. Rev.* **2017**, 117, 9, 5865-6109.

(ii) Khosousi, A. Z.; and Dhirani, A. A. Charge Transport in Nanoparticle Assemblies. *Chem. Rev.* **2008**, 108, 4072–4124.

(iii) Sun, S.; Li, P.; Liang, S.; Yang, Z. Diversified copper sulfide (Cu_{2-x}S) micro-/nanostructures: a comprehensive review on synthesis, modifications and applications. *Nanoscale*, **2017**, 9, 11357.

(iv) Renauda, G.; Lazzari, R.; Leroy, F. Probing surface and interface morphology with Grazing Incidence Small Angle X-Ray Scattering. *Surface Science Reports*, **2009**, 64, 255-380.

(v) Talapin, D. V.; Lee, J. S.; Kovalenko, M. V.; Shevchenko, E. V. Prospects of Colloidal Nanocrystals for Electronic and Optoelectronic Applications. *Chem. Rev.* **2010**, 110, 389–458.

Funding has been provided partly by a scholarship from the German Research Foundation (DFG).

This thesis is organized in three parts as follows:

In the **first part**, an introduction to the subject, the theoretical background of the observed physical processes, and the relevant techniques used this thesis are introduced and described. This part is kept as short as possible in order to provide the necessary fundamental information.

Second part is the results and discussion part which combine the copy of three publications:

Publication 1 by S. Maiti, S. Maiti, Y. Joseph, A. Wolf, W. Brütting, D. Dorfs, F. Schreiber, and M. Scheele titled “Electronically Coupled, Two-Dimensional Assembly of Cu_{1.1}S Nanodiscs for Selective Vapor Sensing Applications” published in *J. Phys. Chem. C* **2018**, 122, 23720–23727.

Publication 2 by S. Maiti, S. Maiti, A. H. Khan, A. Wolf, D. Dorfs, I. Moreels, F. Schreiber and Marcus Scheele titled “Dye-Sensitized Ternary Copper Chalcogenide Nanocrystals: Optoelectronic Properties, Air Stability and Photosensitivity” published in *Chem. Mater.* **2019**, 31, 7, 2443-2449.

Publication 3 by S. Maiti, S. Maiti, A. Maier, R. Banerjee, C. Shen, B. M. Murphy, Marcus Scheele and Frank Schreiber titled ‘In situ formation of electronically coupled superlattices of Cu_{1.1}S Nanodiscs at the Liquid/Air Interface’ published in *Chem. Comm.* **2019**, 55, 4805-4808.

Finally, **third part** describes a summary of the contribution of the author to the following papers:

Understanding the formation of conductive mesocrystalline superlattices with cubic PbS nanocrystals at the liquid/air interface; S. Maiti, S. Maiti, A. Maier, J. Hagenlocher, A. Chumakov, F. Schreiber, and M. Scheele. *J. Phys. Chem. C* **2019**, 123, 1519–1526.

Correlated, Dual-Beam Optical Gating in Coupled Organic-Inorganic Nanostructures; K.M. Wurst, M. Bender, J. Lauth, S. Maiti, T. Chassé, A. Meixner, L. D. A. Siebbeles, U. H. F. Bunz, K. Braun, M. Scheele; *Angew. Chem.* **2018**, 130, 36.

Abstract

This cumulative thesis is based on three publications. It investigates the self-assembly of nanocrystal (NC) superlattices, charge transport in NC assembly, and application of these superlattices in optoelectronic and vapor sensing.

The materials of choice are copper chalcogenide NCs such as binary copper sulfide $\text{Cu}_{1.1}\text{S}$ NCs, binary copper selenide Cu_2Se NCs and ternary $\text{Cu}_{2-x}\text{Se}_y\text{S}_{1-y}$ NCs and the organic semiconductors metal (Cu or Co) centered -4,4',4'',4''',4''''-tetraaminophthalocyanine (Cu/CoTAPc). Macroscopic superlattices of NCs are prepared by Langmuir-type self-assembly at the air/liquid interface followed by simultaneous ligand exchange with an organic semiconductor. To enhance interparticle coupling, we cross-link the nanocrystals with the organic π -system Cu-4,4',4'',4''',4''''-tetraaminophthalocyanine and observe a significant increase in electrical conductivity. Ultraviolet-visible-near-infrared (UV-vis-NIR) and Raman spectroscopy are used to track the chemical changes on the nanocrystals' surface before and after ligand exchange and develop a detailed picture of the various components which dominate the surface chemistry of this material. Grazing-incidence small-angle X-ray scattering (GISAXS) serve to study the importance of electronic conjugation in the organic π -system vs interparticle spacing for efficient charge transport. Transport measurements reveal that Cu4APc provides efficient electronic coupling for neighboring $\text{Cu}_{1.1}\text{S}$ NCs. The electrical properties of monolayers of this hybrid ensemble are consistent with a two-dimensional semiconductor and exhibit two abrupt changes at discrete temperatures (120 and 210 K), which may be interpreted as phase changes. This material provides the opportunity to apply the hybrid ensemble as a chemiresistor in organic vapor sensing. The vapor sensing experiments exhibits a strong selectivity between polar and nonpolar analytes, which we discuss in light of the role of the organic π -system and its metal center.

Next, we choose ternary alloyed Cu-based chalcogenide NCs $\text{Cu}_2\text{Se}_y\text{S}_{1-y}$ and checked the effect of ligand exchange with the organic π -system Cobalt β -tetraaminophthalocyanine (CoTAPc) along with its binary counterpart Cu_2Se NCs. We analysed changes in the structural, optical as well as electric properties of thin films of these hybrid materials. Strong ligand interaction with the surface of the NCs is revealed by UV/vis absorption and Raman spectroscopy. GISAXS studies show a significant contraction in the interparticle distance upon ligand exchange. For copper-deficient Cu_{2-x}Se , this contraction has a negligible effect on electric transport, while for copper-deficient $\text{Cu}_{2-x}\text{Se}_y\text{S}_{1-y}$, the conductivity increases by eight orders of magnitude and

results in metal-like temperature-dependent transport. We discuss these differences in the light of varying contributions of electronic vs. ionic transport in the two materials and highlight their effect on the stability of the transport properties under ambient conditions. With photocurrent measurements, we demonstrate high optical responsivities of 200-400 A/W for CoTAPc-capped $\text{Cu}_2\text{Se}_y\text{S}_{1-y}$ and emphasize the beneficial role of the organic π -system in this respect, which acts as an electronic linker and an optical sensitizer at the same time.

Finally, we report on the in-situ monitoring of the formation of conductive superlattices of $\text{Cu}_{1.1}\text{S}$ nanodiscs via cross-linking with semiconducting Co-4,4',4'',4'''-tetraaminophthalocyanine (CoTAPc) molecules at the liquid/air interface by real-time grazing incidence small angle X-ray scattering (GISAXS). We determine the structure, symmetry and lattice parameters of the superlattices, formed during solvent evaporation and ligand exchange on the self-assembled nanodiscs. $\text{Cu}_{1.1}\text{S}$ nanodiscs self-assemble into two-dimensional hexagonal superlattice with a minor in-plane contraction (~ 0.2 nm) in the lattice parameter. A continuous contraction of the superlattice has been observed during ligand exchange, preserving the initial hexagonal symmetry. We estimate a resultant decrement of about 5% in the in-plane lattice parameters. The contraction is attributed to the continuous replacement of the native oleylamine surface ligands with rigid CoTAPc. The successful cross-linking of the nanodiscs is manifested in terms of the high electrical conductivity observed in the superlattices. This finding provides a convenient platform to understand the correlation between the structure and transport of the coupled superstructures of organic and inorganic nanocrystals of anisotropic shape.

Zusammenfassung

Diese kumulative Arbeit basiert auf drei Publikationen. Es wird die Selbstassemblierung von Nanokristall-Übergittern (engl. nanocrystal, NC), deren Ladungstransport und die Anwendung dieser Übergitter in der Optoelektronik und Dampfsensorik untersucht.

Die Materialien der Wahl sind Kupferchalkogenid-Nanokristalle, wie binäre Kupfersulfid $\text{Cu}_{1.1}\text{S}$ -NCs, binäre Kupferselenid Cu_2Se -NCs und ternäre $\text{Cu}_{2-x}\text{Se}_y\text{S}_{1-y}$ -NCs und die organischen Halbleiter 4,4',4'',4'''-Tetraaminophthalocyanin mit Cu oder Co als metallisches Zentrum (CuTAPc/CoTAPc) als Liganden. Makroskopische NC-Übergitter werden durch die Selbstassemblierung an der Luft-/Flüssigkeitsgrenze hergestellt, gefolgt von einem Ligandenaustausch mit organischen Halbleitermolekülen.

Um die interpartikuläre Kopplung zu verbessern, vernetzen wir die Nanokristalle mit dem π -konjugierten Molekül Cu-4,4',4'',4'''-tetraaminophthalocyanin (CuTAPc) und beobachten eine signifikante Erhöhung der elektrischen Leitfähigkeit. Mit UV-VIS-NIR-Spektroskopie und Raman-Spektroskopie werden die chemischen Veränderungen auf der Oberfläche der Nanokristalle vor und nach dem Ligandenaustausch verfolgt und ein detailliertes Bild über die verschiedenen Komponenten entwickelt, die die Oberflächenchemie dieses Materials dominieren. Röntgen-Kleinwinkelstreuung unter streifendem Einfall (engl. grazing-incidence small-angle X-ray scattering, GISAXS) dient der Untersuchung des Interpartikelabstandes, welcher mit einer Kopplung der NCs durch die π -konjugierten Moleküle und einem effizienteren Ladungstransport korreliert werden kann. Transportmessungen zeigen, dass Cu4APc eine effiziente elektronische Kopplung zwischen benachbarten $\text{Cu}_{1.1}\text{S}$ -NCs ermöglicht. Die elektrischen Eigenschaften von Monolagen dieses hybriden Materials stimmen mit denen eines zweidimensionalen Halbleiters überein und zeigen bei diskreten Temperaturen (120 und 210 K) zwei abrupte Veränderungen, die als Phasenänderungen interpretiert werden können. Dieses assemblierte Hybridmaterial kann als Chemiresistor eingesetzt werden, um Dämpfe organischer Moleküle zu detektieren. Dampfsensor-Experimente zeigen eine starke Selektivität zwischen polaren und unpolaren Analyten, die wir im Zusammenhang mit der Rolle des π -konjugierten Moleküls und dessen Metallzentrum diskutieren.

Außerdem wählen wir Cu-basierte ternär legierte Chalkogenid-NCs ($\text{Cu}_2\text{Se}_y\text{S}_{1-y}$) und binäre Cu_2Se -NCs und untersuchen den Effekt des Ligandenaustausches mit dem π -konjugierten Molekül Co-4,4',4'',4'''-tetraaminophthalocyanin (CoTAPc). Wir analysieren

Veränderungen in den strukturellen, optischen und elektrischen Eigenschaften von dünnen Schichten dieser Hybridmaterialien. Durch UV/VIS-Absorption und Raman-Spektroskopie decken wir starke Wechselwirkung der Liganden mit der Oberfläche der NCs auf. GISAXS-Untersuchungen zeigen eine signifikante Kontraktion des interpartikulären Abstandes während des Ligandenaustauschs. Bei Cu_2Se -NCs hat diese Kontraktion einen vernachlässigbaren Einfluss auf den elektrischen Transport, während bei $\text{Cu}_{2-x}\text{Se}_y\text{S}_{1-y}$ -NCs die Leitfähigkeit um acht Größenordnungen steigt und zu einem metallartigen, temperaturabhängigen Transport führt. Wir diskutieren diese Unterschiede im Zusammenhang der unterschiedlichen Beiträge des elektronischen und ionischen Transports in den beiden hybriden Materialien und zeigen ihren Einfluss auf die Stabilität der Transporteigenschaften unter Umgebungsbedingungen. Mit Photostrom-Messungen demonstrieren wir hohe optische Responsivitäten von 200-400A/W für CoTAPc-funktionalisierte $\text{Cu}_2\text{Se}_y\text{S}_{1-y}$ -NCs und heben die vorteilhafte Rolle des organischen π -Systems hervor, das gleichzeitig als elektronischer Linker und optischer Sensibilisator wirkt.

Schließlich berichten wir über die in-situ-Untersuchung der Bildung von leitfähigen Übergittern aus scheibenförmigen $\text{Cu}_{1.1}\text{S}$ -NCs - durch die Vernetzung mit halbleitenden CoTAPc-Molekülen - an der Flüssig-Luft-Grenzfläche durch GISAXS-Messungen in Echtzeit. Wir bestimmen die Struktur-, Symmetrie- und Gitterparameter der selbstassemblierten NC-Übergitter, die durch Verdampfen des Lösungsmittels und dem Ligandenaustausch entstehen. Die scheibenförmigen $\text{Cu}_{1.1}\text{S}$ -NCs assemblieren sich zu einem zweidimensionalen hexagonalen Übergitter, mit einer geringen Kontraktion von $\sim 0,2$ nm des interpartikulären Abstandes. Eine kontinuierliche Kontraktion des Übergitters wurde während des Ligandenaustauschs beobachtet, wobei die ursprüngliche hexagonale Symmetrie erhalten blieb. Wir schätzen eine resultierende Abnahme der Gitterparameter in der Ebene um etwa 5%. Die Kontraktion wird auf den kontinuierlichen Ersatz der nativen Oleylamin-Oberflächenliganden durch starre CoTAPc-Liganden zurückgeführt. Die erfolgreiche Vernetzung der Nanoscheiben manifestiert sich in der hohen elektrischen Leitfähigkeit der Übergitter. Dieses Resultat bietet einen geeigneten Ansatz, um den Zusammenhang zwischen Struktur und Transport der gekoppelten Überstrukturen aus organischen Halbleitermolekülen und anorganischen Nanokristallen anisotroper Form zu verstehen.

(Sprachberaterin: Andre Maier)

Part I

Scientific Background

1. Introduction

This thesis focuses on copper chalcogenides nanocrystals, their structural, optical and electronic properties in thin films along with the information of how to use them to create electronic devices, particularly vapor sensors and optoelectronic devices. In the last few decades, a considerable amount of research has been focused on the study of copper chalcogenides materials due to their compositional and structural versatility. As one of the purposes was for the construction of Cu-based chalcogenide materials that have dimensions on the nanoscale, in particular towards the understanding of their unique optical and electronic properties that dramatically distinguishes them from their bulk counterparts.¹ Several successful attempts have been made towards synthesis, understanding electronic properties, and charge carrier concentration dependent localized plasmon resonance (LSPR) characteristics of these materials.²⁻⁸ Other sophisticated studies like formation of NCs superlattices at the interface, structural and optical characterization of the superlattices films, low-temperature transport mechanism, and application in optoelectronics and vapor sensing routes remain less studied. Inspired by the above, this research project seeks to explore the unique structural, optical and transport properties of the Cu chalcogenides nanocrystals thin films. We use $\text{Cu}_{1.1}\text{S}$, $\text{Cu}_2\text{Se}_y\text{S}_{1-y}$ and Cu_2Se nanocrystals as building blocks for larger superstructures, with the eventual goal of creating novel electronic devices out of them. So, to exploit interesting electronic properties of these nanocrystals (NCs) in thin film devices, replacement of the original bulky ligands attached on the NC surface to short ones is essential. The idea behind this is to cross-link the individual nanocrystals with a shorter organic molecule to provide an electronic coupling if their energy levels are located in a range near the nanoparticle's energy bands. We use the electronic coupling of binary copper sulfide $\text{Cu}_{1.1}\text{S}$ with the organic π -system Copper β -tetraaminophthalocyanine (Cu4APc) to create two-dimensional self-assembly for selective chemical vapor sensing. We investigate ligand exchange effect of ternary $\text{Cu}_2\text{Se}_y\text{S}_{1-y}$ as well as the binary Cu_2Se nanocrystals (NCs) with the organic molecule Cobalt β -tetraaminophthalocyanine (CoTAPc) and analyze changes in the structural, optical as well as electric properties of thin films of these hybrid materials. Furthermore, we study how the anisotropic shape $\text{Cu}_{1.1}\text{S}$ nanocrystals self-assembled at the liquid-air interface that is nanocrystals which 'spontaneously' form larger hierarchical structures in real time.

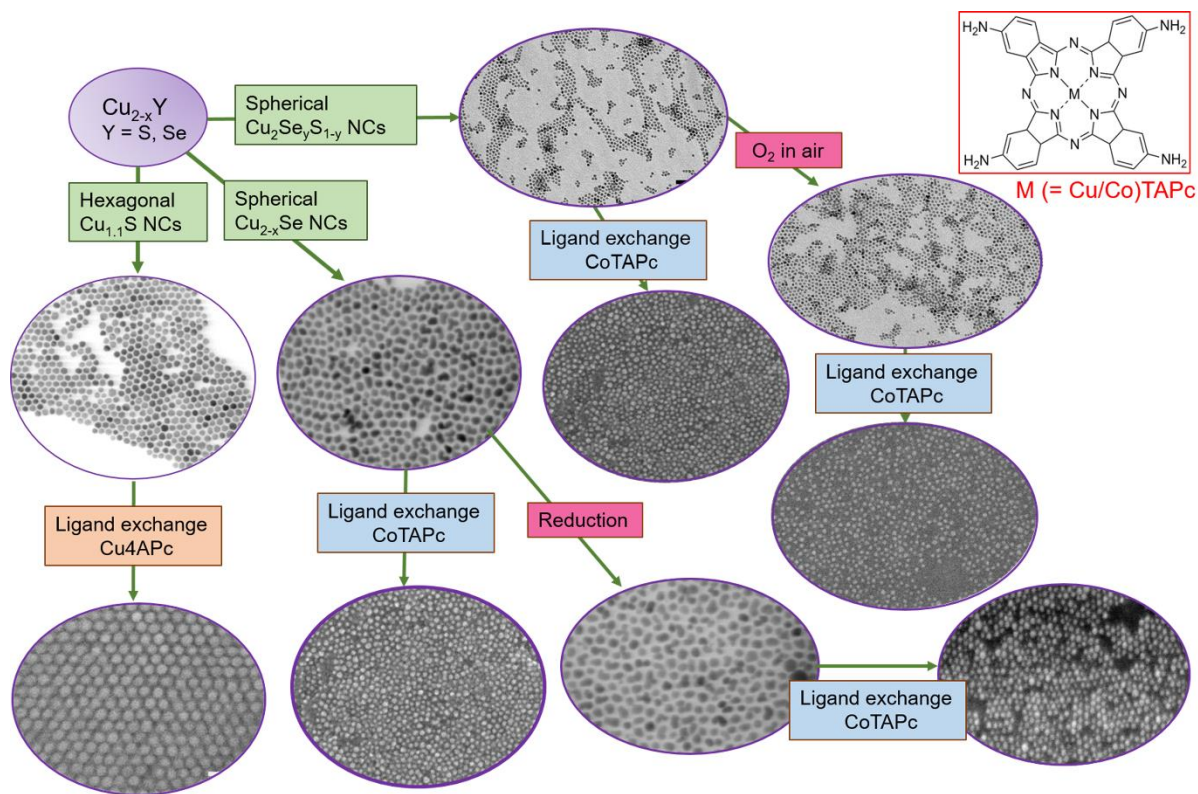


Figure 1. Overview of the thesis will describe.

1.1. What are nanocrystals?

Nanocrystals are small crystalline materials, having dimensions in the range of the 1–100 nm, which provide one of the greatest potentials for improving performance and extended capabilities of products in a number of industrial sectors.⁹⁻¹¹ There is a strong drive among researchers to explore the possibilities by down-sizing the existing material structures into the nanometre scale (<100 nm), or by making new types of nanostructures. This drive is caused by two factors. First of all, there is a great fundamental interest in the new electronic or optical properties that arise when a material becomes so small that it consists of only a few tens to thousands of atoms. Quantum mechanical effects start to dominate the properties of the bulk material when the size is typically a few nanometers. To develop highly sensitive techniques for investigating the morphological, electronic and optical properties of the (individual) nanocomponents is one part of the challenge in nanotechnology along with synthesizing these materials. Besides the scientific interest, the wide range of potential applications based on nanomaterials is an important driving force to push the size of materials to the smallest limits.

The term ‘nanocrystal’ encompasses a wide range of geometries and in general, they can be classified according to their configuration where their intrinsic properties arise from dimensional restrictions. This allows them to act as zero dimension (quantum dots and nanoparticles), one dimension (nanorods, nanowires, and nanotubes), two dimensions (ultra-thin films, nanosheets) or in all three dimensions (nanoprisms).^{12, 13} NCs are of immense scientific interest as they effectively bridge the gap between the small, individual molecules with discrete energy states and that of bulk, crystalline materials with continuous energy states.¹⁴⁻¹⁷ The nanocrystals we study in this thesis are all semiconductors: materials through which we can control the current by applying an external bias.

1.2. Why are colloidal nanocrystals interesting?

Nanocrystals are interesting for two main physical reasons: i) a relatively larger surface area in size range of nanostructure compared to the same mass of a material produced in a larger size affects their physical and chemical properties, and ii) quantum effects start to dominate the behavior of materials in the nanoscale form affecting the optical, electrical and magnetic behavior of matter. Interest in colloidal compound semiconductors originates from the search for photochemical catalysts to address high oil prices in the late 1970s.^{18, 19} Brus and co-workers in the 1980s first observed quantum size effects in colloidal semiconductors where they explained the term quantum confinement of free charges due to the finite size of the crystallite.²⁰⁻²³ The quantum confinement effect originates from the decoupling of molecular orbitals due to the decreasing amount of atoms within the semiconductor nanocrystals. Relative to the bulk, there are two primary ways in which the energy levels of a semiconductor nanocrystal are perturbed: 1) by a change in dielectric screening and carrier localization because of the finite crystal size²⁴ and 2) by confinement of the exciton into a region smaller than the Bohr radius.^{21, 25}

The first effect manifests as a change in the oxidation and reduction potentials of the valence and conduction bands, which opens the door to tuning the electrochemical behavior of semiconductors by varying the size. The confinement of the exciton manifests as an increase in the prominence of the exciton in the absorption spectrum as well as an increase in the exciton's energy relative to the bulk. In a bulk semiconductor, the essentially infinite number of atomic orbitals overlaps and forms continuous energy levels, leading to the formation of conduction and valence bands. In contrast to metallic materials, intrinsic semiconductors have

a completely separated conduction band and valence band with a constant band gap (HOMO-LUMO separation) in the range of 0.3 to 3.8 eV depending on the identity of the material.¹ In the case of a semiconductor of nanocrystalline size, the band gap energy increases as the physical size of the material decreases within a critical range. Specifically, when the size decreases below the bulk exciton Bohr radius, there are not a sufficient number of atoms to form the continuum of energy levels. Instead, electrons and holes are quantum confined in three dimensions by the nanocrystallite, resulting in the breakdown of continuous energy bands into discrete atomic-like energy states, as illustrated in **Figure 2**.

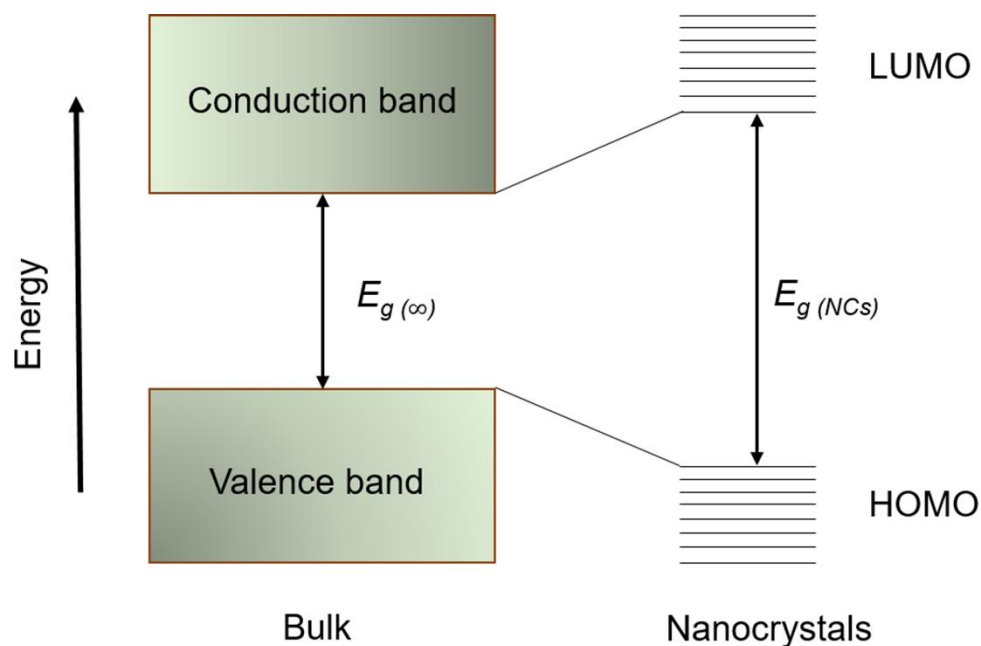


Figure 2. A schematic illustration of the change of the electronic properties when the size of a semiconductor decreases. At the left, an energy band diagram for a macrocrystalline semiconductor is shown, $E_{g(\infty)}$ being the bandgap. While the picture on the right represents the situation when the dimensions of the semiconductor are smaller than those of the exciton, $E_{g(NCs)}$ is the energy of the lowest excited state (adapted from Steigerwald and Brus)²⁶.

The energy of the electron or hole near the conduction or valence band edge can be approximated by a quadratic relationship between the wave-vector k and energy (equation 1, where m^* is the effective mass of the electron or hole). This means that carriers with energies near the band edge can be thought of as free, and move in response to applied electric fields according to their effective masses.

$$E = \frac{\hbar^2 k^2}{2m^*} \quad (1)$$

If a free electron and hole are brought near one another, they will begin to orbit one another, forming a Wannier exciton, in which the electron and hole are bound to one another. The exciton has, by analogy to the hydrogen atom model, a Bohr radius which provides a convenient conceptual touchstone for understanding the phenomenon of quantum confinement. Brus and co-workers considered what would happen to the energy of an exciton as the size of the nanocrystal was reduced, and found that the energy of the lowest transition increased with decreasing particle size following equation 2 where E_g is the bulk gap, R is the particle size, m_e and m_h and the electron and hole effective masses, e is the charge of an electron, and ϵ_∞ is the dielectric constant outside the nanocrystal.^{20, 21}

$$E(R) = E_g + \frac{\hbar^2 k^2}{2R^2} \left[\frac{1}{m_e} + \frac{1}{m_h} \right] - \frac{1.8e^2}{\epsilon_\infty R} \quad (2)$$

Comparing the functional form for the lowest excited state of a semiconductor nanocrystal (equation 2) with the energy levels for particle in a box (equation 3, where n is an integer, R is the size of the potential energy well, and the other symbols have their usual meanings.) gives a conceptual framework for considering the energy levels as a function of size. Both systems have a dependency on size $E \propto \frac{1}{R^2}$, such that the lowest state increases in energy as the box decreases in size.

$$E(n) = \frac{\hbar^2 k^2 \pi^2}{2R^2 m} n^2 \quad (3)$$

By solely varying the physical size of the NC, the percentage of atoms at the surface relative to the core significantly increases, causing pronounced internal disruptions to the electronic structure and resultant optical properties of the material. This essentially provides an effective means to tailor the electronic structure and optical properties, giving rise to size-dependent band gaps in semiconductor NCs. Depending on the identity of the semiconductor (IV, III-V, II-VI or IV-VI group), the critical radius can be widely different, ranging from 2 nm to 60 nm.¹ Copper chalcogenide materials with critical dimensions in the nanometer range have been of considerable interests because of their low-cost and unique physical and chemical properties with the capability of bandgap engineering for use in a diverse range of applications. These NCs show the advantages of low-temperature preparation, and economical and convenient

post-processing such as spin-casting, dip-coating, and printing, as well as high device performance from quantum confinement effect.^{3, 8, 16, 27, 28}

1.3. Copper chalcogenide nanocrystals

In recent years' copper chalcogenide NCs have attracted an increasing attention due to their potential application in energy related fields. The interest in those NCs resides in three key aspects: (i) their abundance, low cost, and reduced environmental and health impact, compared with cadmium- and lead-based compounds; (ii) their excellent intrinsic functional properties, including appropriate direct band gaps for solar light absorption, plasmonic properties, notable charge carrier mobilities, potential high carrier concentrations, and low thermal conductivity; and (iii) their structural, compositional, and stoichiometric versatility, including abundant non-stoichiometric phases, a wide range of solid solutions, and the related low energy of formation of defects. Even the simplest binary compounds, Cu_{2-x}Y (where $\text{Y} = \text{S}, \text{Se}, \text{Te}$), there are over 20 reported binary stoichiometries, polymorphs, and defect phases. Until now several dozens of ternary and multinary compounds of chalcogenides have been reported.²⁹

An interesting evolution in properties and applications as the number of elements increases, from the simplest binary elemental composition, of Cu and a chalcogen (S, Se, Te), to the more complex multinary compositions. The low size and electronegativity differences between the metals and chalcogens, the ability to form chalcogen-chalcogen bonds, and the possibility of Cu-Cu bonds within the structure, allows for a large diversity in stoichiometry and crystal structures and the resultant functional properties. The high defect concentration influences their charge transport properties, which greatly affects their electronic, thermoelectric, and optoelectronic properties. For example, the binary Cu chalcogenides have been long investigated for their interesting plasmonic properties, which allow them to be used as novel probes for surface-enhanced Raman spectroscopy (SERS) or hyperthermia. The hierarchical organization of NCs serves as the wide application set for these materials, including photovoltaics, optoelectronics, thermoelectrics, photocatalysis, fluorescent biological imaging, and photothermal therapy.^{3, 8, 30-33} Several reports have been published in the literature on p-type Copper sulfide where the materials give application in catalytic, batteries, sensing and bio-related field which results in tremendous endeavors on the rapid development of micro-/nanostructured binary copper sulfide with well-controlled compositions, sizes, crystalline phase, and morphologies.^{29, 34, 35}

The simplest and the far most studied binary copper chalcogenide is Copper sulfide (Cu_{2-x}S). A number of stoichiometric compositions of Cu_{2-x}S from copper-rich Cu_2S (chalcocite) to sulfur-rich CuS (covellite) exist with different crystal structures, leading to the increasing electrical conductivity and tunable direct band gap.³⁶ It possesses band gaps of 1.1 – 1.4 eV for chalcocite ($x=0$), increasing to 1.5 eV for digenite ($x=0.2$) and further increasing to 2.0 eV for covellite ($x=1.0$).³⁷ The exciting surface plasmon resonance can be observed under near infrared region (NIR) in various Cu_{2-x}S owing to the formation of free charge carriers. Cu_{2-x}S and its selenium analogue, copper selenide (Cu_{2-x}Se), are regarded as being competitive p-type semiconductor candidates owing to the copper vacancies in their lattices. Another important class of Cu-chalcogenide NCs contains two anionic chalcogens, in which the two chalcogens are typically sulfur and selenium. This gives rise to NC compositions, which range from ternary $\text{Cu}_{2-x}\text{Se}_y\text{S}_{1-y}$, to quaternary $\text{CuIn}(\text{S}_{1-x}\text{Se}_x)_2$ and quinary $\text{Cu}_2\text{ZnSn}(\text{S}_x\text{Se}_{1-x})_4$ (CZTSSe).²⁹ Ternary alloyed copper sulfur selenide ($\text{Cu}_{2-x}\text{Se}_y\text{S}_{1-y}$) NCs provide an effective way to finely tune the optical band gap, by controlling the S/Se chalcogen ratio in the resultant NCs.^{28, 38-40}

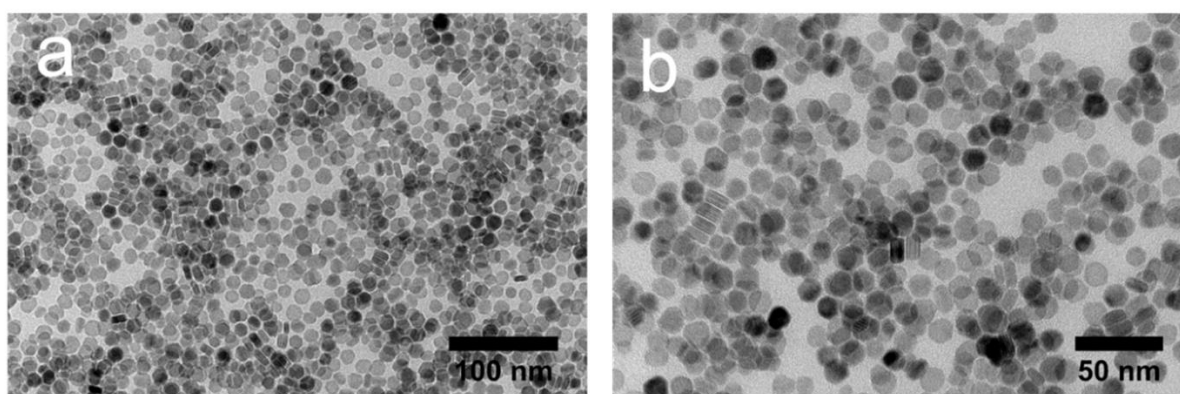


Figure 3. (a) & (b) TEM images of $\text{Cu}_{1.1}\text{S}$ NCs.

Same as Copper Sulfide, Copper selenide is a p-type semiconductor material with potential application in solar cells, superionic conductors, thermoelectric devices and microwave shield coating. It also has potential application in optical filters, nanoswitches, thermoelectric and photoelectric transformers and superconductors.^{30, 41-44} A particularly interesting feature of copper chalcogenide NCs is their essential degree of doping based on the formation of copper vacancies in the structure.^{6, 31, 32, 45, 46} Moreover, they could be used as templates to prepare multielement metal chalcogenides. Recently, ternary Cu–Se–S semiconductor NCs have been obtained significant attention for not only inheriting the perfect optoelectronic and biochemical

properties from their parent binary NCs (Cu_{2-x}Se and Cu_{2-x}S) but also possess unique properties. There have been some reports on synthesis of alloyed $\text{Cu}_{2-x}\text{S}_y\text{Se}_{1-y}$ NCs in which their NIR LSPR has been tuned by controlling the ratio of chalcogen.^{38, 47-49} However, pure Cu–Se–S NCs have not been extensively studied like their binary parents. This could be due to the difficulty in the synthesis of this type of nanomaterials with pure phases.

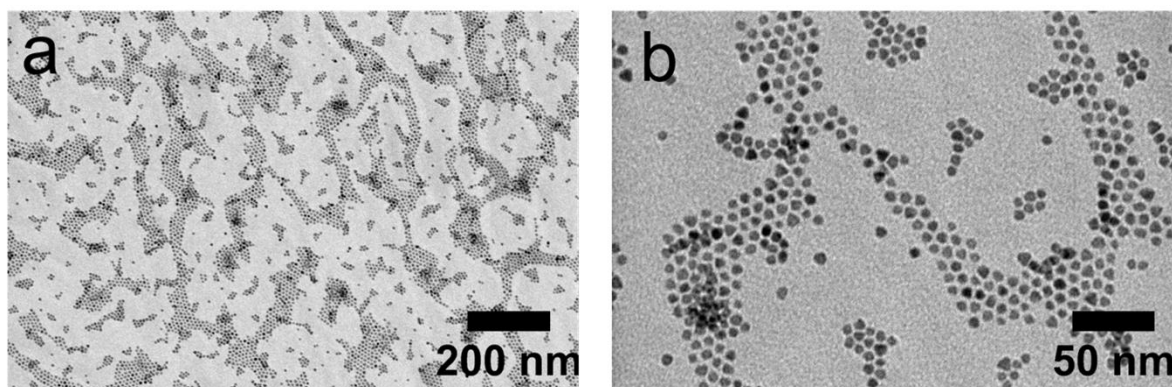


Figure 4. (a) & (b) TEM images of $\text{Cu}_{2-x}\text{Se}_y\text{S}_{1-y}$ NCs.

Various morphologies of copper chalcogenide nanocrystal have been well-demonstrated including spheres, cube, wires and sponge-like structures.^{29, 44, 48} The hierarchically anisotropic structure is more suitable in electronic device owing to oriented electronic migration and structural integrity.⁵⁰ The development of novel nanostructured copper chalcogenide with controllable building block and composition as well as the crystalline-phase feature is still an interesting and challenging topic for both fundamental study and technological application. Moreover, the functional modifications (including hybridizing and doping) of the interfacial properties and electronic structures of $\text{Cu}_{2-x}\text{S}/\text{Cu}_{2-x}\text{Se}$ -based nanostructures would effectively bring enhanced performances. Thus a systematic investigation on the formation mechanisms of different nanostructured Cu-chalcogenides can further optimize the physical properties such as morphology, optical behavior, structure, and electronic correlation, and application in Optoelectronics or Sensing would offer new insights to develop high-performance Cu-chalcogenide based materials.

1.4. Coupled organic-inorganic nanostructures (COINs)

Utilizing the unique physical properties of nanocrystals in solid-state devices is itself a challenge. There are several independently controllable factors i.e., NPs size, shape, and chemical composition, interparticle separation, material structure and so on. Since the basic building blocks (i.e., NCs are capped with organic molecules, the resultant self-assembly materials are mostly decoupled. A wide range of material properties can be realized over using a broad range of the building blocks, their surface ligands, and their arrangement procedure into bigger structures.

Most of the as-prepared copper chalcogenide NC assemblies are usually non-conductive as they have insulating surface ligands (i.e. oleic acid or oleylamine). Frequently, it is problematic to probe the continuous charge transport measurements within the NCs superlattices due to the nanoparticles isolated by their ligand shell. The ligand shell often consists of long-chained organic molecules, with one end attached to the particle's surface to stabilize them in the dispersion. These capped ligands prevent the agglomeration of the NCs into arbitrary macroscopic structures. Being made of long and insulating hydrocarbons, the ligand shell displays a strongly insulating effect, therefore limiting the charge carrier movement. Several attempts have been made to decrease inter-particle spacing of a self-assembled structure by removing ligand shells of NCs through different chemical methods.

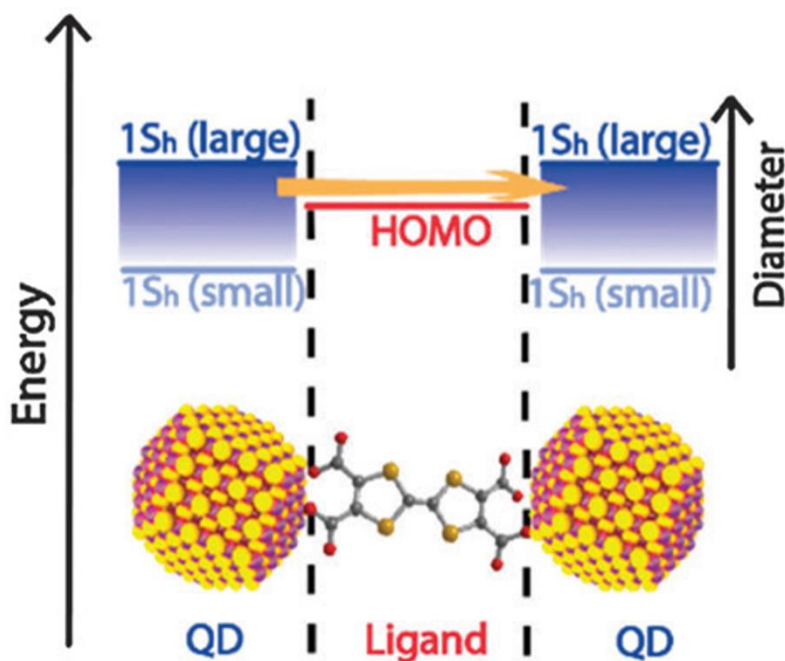


Figure 5. Energy level diagram of a COIN interface. In this example, the inorganic $1S_h$ state is tuned by the QD diameter to align with the HOMO of the OSC as for instance (adopted from Scheele et al.⁵¹)

In this thesis, we have taken a novel approach to reveal the optoelectronic properties of the nanostructures, which commonly known as coupled organic-inorganic nanostructures (COINs).⁵² Here, the insulating ligands are exchanged by new organic molecules that are already known to be semiconductors due to their conjugated π -system. Firstly, the new adligands chemically bound to the surface of the particles and spatially linking with neighboring particles. Secondly, they can act as an electronic coupler if their energy levels are located in a range near the nanoparticle's energy bands. A resonant alignment of either the $1S_e$ of the NC and the lowest occupied molecular orbital (LUMO) of the molecules, or the $1S_h$ of the NC and the highest occupied molecular orbital (HOMO), provides a conductive channel throughout the coupled structure. The electronic properties of the system can be varied by the ligand length and chemical structure by delocalization the charge carrier via new adligand. The ligand could, therefore, act as a bridge for the charge carriers, over several elements of the COIN and open the path to electrical conductivity over the structure (see in **Figure 5**). In addition, the ligands trigger the nanoparticles to arrange into a fashion that, depending on the COIN's fabrication process, ranges from glass-like to very ordered structure. COINs have been proven to be versatile coupled organic-inorganic materials with tailored properties. A typical schematic representation of hole and electron conducting states of monodisperse NCs and the LUMO – HOMO state of the OSC molecules are presented in **Figure 6**. This kind of electronically coupled structures has gained as a conceivable field of application in solar cells or diodes.

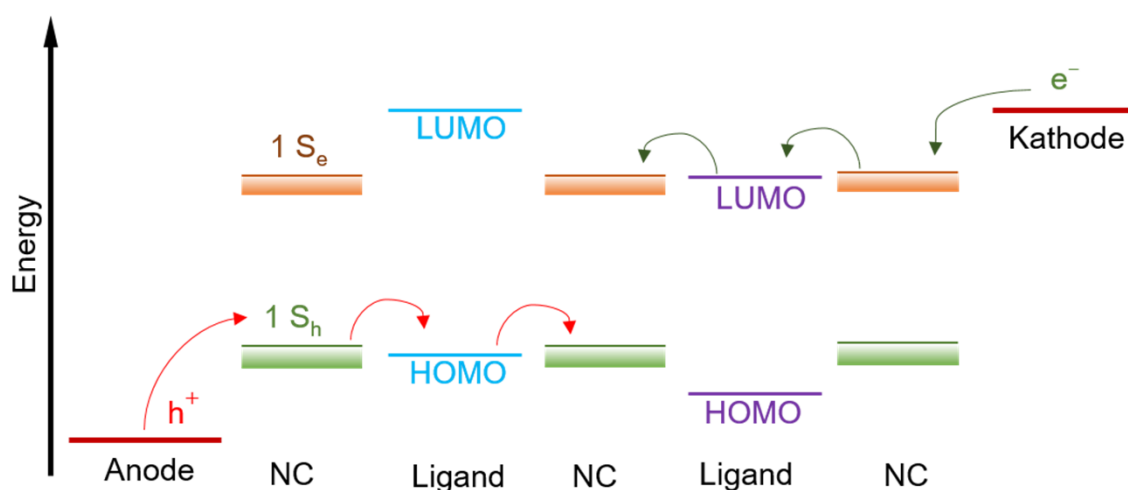


Figure 6. Schematic representation of a possible mechanism for hole and electron transport in a COIN system.

Previously, our group produced COINs of PbS NCs coupled with different organic semiconductor molecules.⁵²⁻⁵⁵ In this thesis, we produce COINs with different copper chalcogenides NCs. One study, we demonstrate disk shape $\text{Cu}_{1.1}\text{S}$ NCs (see in **Figure 3**) formed COINs using CuTAPc molecules and the resultant superlattice film has a 2D hexagonal ordering. In another work, we developed and optimized a method to investigate the structure and their electrical properties of the COIN system using binary Cu_{2-x}Se and ternary $\text{Cu}_{2-x}\text{Se}_y\text{S}_{1-y}$ (**Figure 4**) as inorganic nanocrystals and CoTAPc as organic semiconductor ligands. In a final work, we have studied the in-situ formation kinetics of the COIN formation on the liquid surface using disk-shape $\text{Cu}_{1.1}\text{S}$ NCs by X-ray scattering.

1.5. Self-Assembly of Nanocrystals

In recent decades, there has been a rapidly growing field of study exploring properties of NP assemblies. Those studies improve our understanding of the basic science governing the properties of these materials and providing hope for their applications. Out of many existed techniques reported in the literature, self-assembly methods are very promising in order to prepare long-range-ordered nanocrystals superlattices.^{4, 7, 29, 56-58} In this context, the superlattice is defined as an array of inorganic nanocrystals which are separated by organic or inorganic surface ligands.

Over the years, different strategies have been employed for the assembly of a wide variety of NCs with four types of assembly processes dominant: (i) Drying mediated assembly; (ii) Assembly at the interface; (iii) Assembly in solution; and (iv) Directed assembly.⁵⁹ These techniques become a rich tool for laboratory scale NC assembly along with their scalability to wafer level substrates suggests a possible extension to real-world applications. The first method is based on the solvent evaporation, the NCs are dispersed in an appropriate solvent (mostly organic, such as toluene, hexane, octane etc.) and are drop-cast onto a clean and polished substrate, followed by slow solvent evaporation. During the solvent drying period, the local NC concentration gradient (underneath the liquid surface) increases, which reduces the interparticle distance between NCs. The process initiates numerous attractive (dipole-dipole) and repulsion interactions (Columbic), which ultimately stabilize the NCs into a close-packed 2D/3D superstructure at the surface.⁶⁰ The entropy driven superlattice formation can be further increased by controlling the temperature of the process, the temperature of the substrate and native environment (based on Helmholtz free energy).^{60, 61}

Formation of NPs self-assembly at the liquid-liquid and liquid-air interface has been investigated for more than a century. The idea of self-assembly of NCs into superlattices comes from the Pickerin-Ramsden emulsions phenomenon.^{62, 63} In this process, the interfacial assembly is driven by the total reduction of interfacial free energy between two immiscible phases due to particle adsorption on the interface. Depending upon the particle size, the assembly can be higher (micron size) or comparable (nanometer size) to thermal energy ($k_B T$), and this will govern the adsorption of particles at the interface. In general, smaller particles adsorb more weakly than larger ones at the interface, and hence, the assemblies from larger particles are more stable. Apart from particle size, particle shape and surface chemistry also play key roles in the overall assembly process and the stability of final superstructures, as they influence the wettability (change in surface energy) and the interparticle interactions. The important role of the liquid interface is to provide a mobile surface for the particle to move freely and rearrange into their closely packed configuration. The assembly of colloiddally synthesized NCs, at interfaces with different degrees of short- and long-range ordering has been studied for isotropic (i.e. spheres, cubes) and anisotropic NCs (i.e. nanorods, nanowires, nanoplates, nanoprisms) in both metal NCs and semiconductor NCs. In the case of spherical NCs, the close-packed assembly is generally favored due to the interparticle interactions. In contrast, for anisotropic NCs, shape and spatially dependent (interface mediated) capillary forces govern the overall assembly, due to the undulation of the contact line at the interface. ratio, and the interfacial energy between liquids and the NC. Murray and co-workers reported a simple technique of drop-casting the NC dispersion on an immiscible subphase and then controlling the evaporation rate to drive the assembly for a wide range of NC morphologies (spheres, plates, rods, prisms) with complex structures (binary, ternary to quaternary).⁶⁴⁻⁶⁸ Third is Assembly in solution in which nanoparticles can coalesce in solution, due to interactions such as van der Waals, dipole-dipole, or electrostatic along with ligand-ligand, ligand-solvent present in NC solutions, which govern the assembly.⁶⁹ Choice of solvent, capping ligand plays an important role in the formation of this kind of self-assembly. In several works, people have shown that by simply adding various additives to a stable NCs colloidal solution to achieve higher order assembly. In the directed assembly process, external forces (electric and magnetic field) is applied to facilitate NC assembly. This type of assembly of NC is remarkably versatile, not only to control assembly size but also to precisely tune the location where an assembly forms. Over the years, much more research has been done to extend control of the assembly by applying external forces. It should note that in the case of arranging

anisotropic NCs, which requires additional control in both translation and orientational order, the application of external fields can provide the necessary control.

The ligands play a significant role in the self-assembly process on NCs. It separates the core of the NC from the bulk solution and direct control over the interaction between the NC and ligands environment. So, the choice of a ligand for surface passivation is a key factor for manipulating their properties, inter-particle interaction, ligand-ligand interaction, and the self-assembly process.⁷⁰ The long chain organic ligands (hydrophobic in nature) passivate the trap states on the NC surface, by binding to the low-coordinating surface atoms, which helps to solubilize the NCs in nonpolar solvents and form stable colloids. When the NCs are in solution, the ligands keep on adsorbing and desorbing on NC surface. The ligand nature and their interaction with other ligands or solvent molecules determine the extent of colloid stability. When two NCs approach at a distance smaller than twice the ligand length, the chains compress and yield a repulsive force between the NC to make the dispersion stable. The chain length and chemical composition of the capping ligands can influence the dipole moments of the NCs, their reactivity, and their stability in solution and direct the self-assembly via electrostatic interactions or bonding. It has become ever more important to understand this synergism between the NC surface and the capping ligands, which has significant consequences for the properties of assembled materials, as compared to individual NC building blocks. In the case of monodisperse spherical NCs with an organic ligand covered surface, it is expected that the assembled structure would arrange into a face-centered cubic (fcc) lattice to achieve the maximum packing efficiency.^{63, 70} Researchers shows in several literatures how the capping ligand mediates the interaction between the NC and solvent for the purpose of assembly. Li and co-workers showed for the first time that the columnar self-assembly of Cu₂S hexagonal nanoplates can be induced by in situ formation of a Sn-X complex (inorganic ligand) during the synthesis.⁷¹ Most nanoplates tend to stack face-to-face to form a columnar superstructure. This ligand-induced columnar assembly approach has also been used for the Cu_{2-x}Se NCs.⁷²

In this thesis, we mostly study 2-D self-assembled materials, inspired by materials such as graphene. In order to create materials with reduced dimensionality, we have to confine the self-assembly process of the NCs to two dimensions. The method pioneered by Dong et al.^{4, 73}, uses a liquid substrate (as shown in **Figure 7a**). In this method, the colloids do not dissolve but adsorb at the liquid-air/N₂ interface due to surface energy considerations after solvent evaporation. Nanoparticle monolayers can be obtained in which the NCs are epitaxially

connected resulting in excellent long-range nanocrystalline order. Also, the assembly can be controlled by tuning the NC concentration and the solvent evaporation rate. We modified this method to prepare COIN superlattice film by injecting ligand solution in the subphase in order to ligand-exchange the assembled NC film. By carefully choosing Cu-based chalcogenides NCs and π -conjugated organic semiconductor ligand solution we are able to get the resulting superlattices of thickness down to an NC monolayer with a typical grain size of hundreds of micrometers. And it can be scooped off the interface by simple fishing or Langmuir-Schaeffer like stamping of the NC film. The relative easiness to handle and versatility makes this process to create 2-D semiconductors attractive for industrial applications.

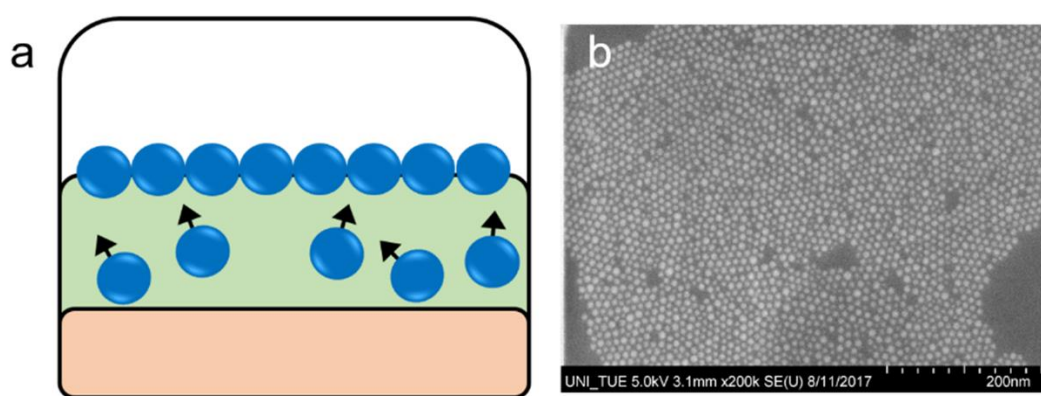


Figure 7. (a) Two-dimensional confinement of the self-assembly process, as is studied mostly throughout this thesis. The NCs are confined at a liquid-air/ N_2 interface, which can result in superlattices which have a thickness of an NC monolayer. (b) STEM image of $Cu_{1.1}S$ NCs superlattice prepared at liquid-air interface.

1.6. Characterization of NCs and their superlattices

In general, the nanocrystals are too small to be studied through conventional optical microscopy. Therefore, we have performed different types of electron microscopy to determine the size and shape of the Copper chalcogenides NCs, used in this thesis. An electron microscope uses a high voltage electron beam to illuminate the specimen and create an image. The electron beam is generated by an electron gun. The beam is accelerated by an anode with respect to the cathode, focused by different lenses, and transmitted through the specimen. When it emerges from the specimen, the electron beam carries information about the structure of the specimen that is magnified by the objective lens of the microscope. Electron microscope provides a spatially resolved of the specimen and is used throughout this thesis in various forms. In particular, Scanning-transmission electron microscopy (STEM), is used to check the

size and shape of the basic NCs and to determine the film morphology of the self-assembled NCs and their ligand-induced assembled structures. The optical properties of the NC superlattices films are characterized with absorption spectroscopy (how much photons are absorbed by the NCs at each photon energy), Raman and FTIR spectroscopy (molecular vibrations or other excitations in the system interact with laser light and produce a shift up or down of laser phonons). To determine the large scale structure in the ex-situ samples, we used X-ray scattering techniques in our laboratory source. For the in-situ measurements (self-assembly of NCs and their ligand exchange) we performed specialized liquid surface X-ray scattering using synchrotron source. These techniques allow us to study the kinetics of the self-assembly and ligand exchange processes in more detail under reaction conditions on both nanocrystal and atomic length-scales. The next section will discuss the applied techniques in more detail.

1.7. Grazing incidence small angle X-ray scattering (GISAXS)

In the last two decades, the Grazing Incidence Small Angle X-Ray Scattering (GISAXS) has emerged as a powerful technique that allows us to investigate the morphological properties in a non-destructive way. It measures the structural order of nanoparticle assemblies, deposited either on a surface, interface or embedded in a matrix, with sizes ranging from 1 nm to several microns.

X-ray scattering probes nanostructures on the surface in the reciprocal space, or the Fourier space. The principle of X-ray scattering from nanostructures is identical to traditional X-ray diffraction, except that, (i) high intense synchrotron X-ray beam is usually needed because the investigated volume of matter is small; and (ii) the incident beam angle is kept at a grazing incidence with respect to the sample surface to minimize the unwanted background scattering emanating from the bulk structure, and to enhance the near-surface scattering from the thin film. In GISAXS, all the angles (incidence, out-going azimuthal and reflected) considered are small, i.e. less than a few degrees. In general, the incoming X-ray beam impinges on the surface of interest at an angle lower than the materials' critical angle, α_c (mili-radians), the X-ray photons will be reflected from the interface and only have an evanescent component inside the materials, this leads to a total external reflection and much more scattering. However, by changing the grazing angle and hence the penetration depth of the X-ray photons, we can obtain information from both the bulk and the surface of a material of interest. If there are nanometer-size in-homogeneities of the electron density such as islands, roughness or electronic contrast

variation are present on the surface or interface, X-ray scatters the incident beam, depending on their morphology and topography.

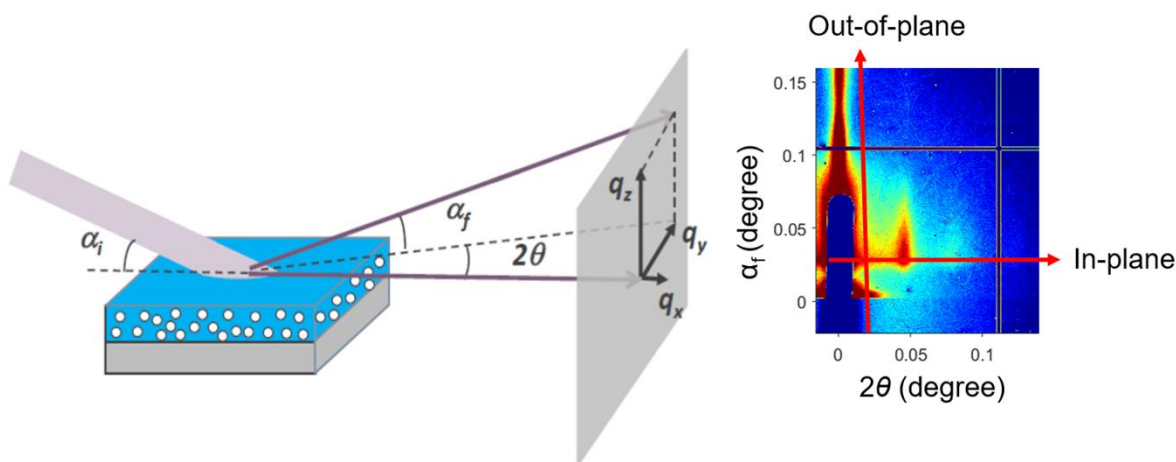


Figure 8. Typical experimental geometry of grazing-incidence X-ray scattering experiments.

Throughout this thesis, we performed X-ray scattering experiment in grazing-incidence geometry, as shown in **Figure 8**. The X-ray photons are scattered in the forward direction to a detector collecting the scattering signal, where inter-nanoparticle distances and nanocrystalline structures can be followed in ex-situ or in-situ measurements over time. The GISAXS detector is usually at a relatively large distance, depending on the X-ray photon energy, since Bragg reflections need to sufficiently diverge in order to be separated from the direct beam. Publication 1 and 2 of the results and discussion part of this thesis contain the study the ex-situ GISAXS measurements of the self-assembled NCs and their ligand-exchanged assemblies have performed by using a laboratory instrument (Xeuss 2.0, Xenocs, France) using Cu K α radiation ($\lambda = 1.5418 \text{ \AA}$). The samples are probed with a focused X-ray beam of size $0.5 \times 0.5 \text{ mm}^2$ at an incidence angle of 0.22° . The GISAXS images are collected with a 2D Pilatus 300 K, having 487×619 pixels. The detector is placed at a distance of 2496 mm, determined using Ag-behenate as reference sample. We further study the in-situ self-assembly of nanocrystals and ligand exchange at the liquid/air-interface under this so-called grazing incidence geometry in the synchrotron source at P08 beamline, PETRA III, DESY, Hamburg, Germany. In this geometry, the collimated X-ray beam has to bend down towards the liquid surface. This is either achieved using X-ray mirrors or by using a crystal deflection scheme. Here one or two crystals are placed in a Bragg condition of one of their reflections, and they are rotated such that the photons follow the 2θ cone. The diffractometer arm, carrying the detectors, has to be rotated accordingly to follow the path of the X-ray beam.

It is possible to analytically calculate the full scattering signal of any material through the distorted wave Born approximation (DWBA). This takes multiple scattering effects into account, such as interference between scattering from the direct and reflected beam, into account by calculating the Fresnel coefficients of each scattering term. So, using this approach the total scattering pattern in an X-ray scattering experiment in grazing incidence geometry can be approximated as the product of the structure factor of the lattice and the form factor of the constituent particles, i.e. $S(q) \cdot P(q)$. Example of the GISAXS pattern obtained from solid and liquid surface is displayed in **Figure 9**. We used DWBA to simulate the GISAXS pattern obtained at the liquid/air interface to avoid multiple scattering as seen in **figure 9b**. Both patterns represent two-dimensional hexagonal lattice of NCs, where the consecutive order of 1: $\sqrt{3}$: 2 of peak positions in the horizontal scattering direction shows the signature of this lattice. Since the lattice is 2-D in the horizontal plane in real space, the structure factor appears as elongated rods in reciprocal space.

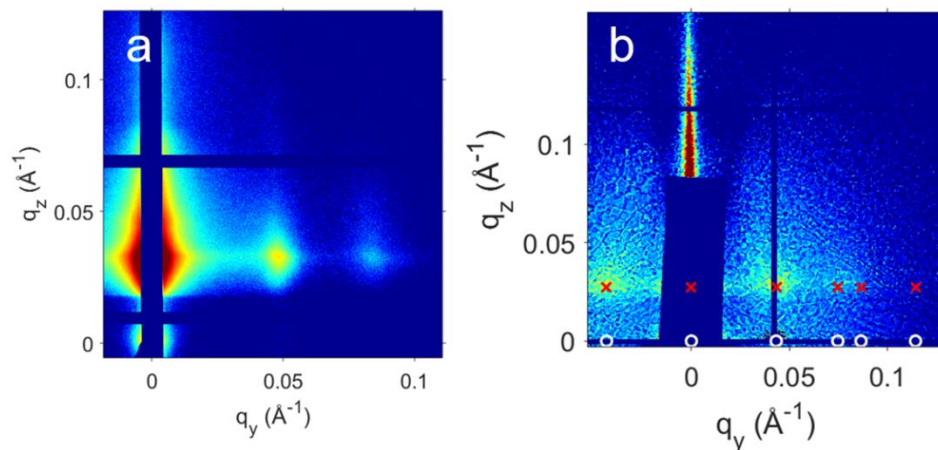


Figure 9. (a) Typical GISAXS pattern obtained from ex-situ Cu_{2-x}Se NCs superlattice film. Here, the incoming X-ray photons have an energy of 8 keV and hit the surface at a glancing angle of 0.2° (b) GISAXS patterns of $\text{Cu}_{1.1}\text{S}$ NDs superlattices film at the liquid/air interface. The red circles and pink boxes are the simulated diffraction patterns considering a hexagonal superlattice along the in-plane direction. Note that the direct beam, i.e. the reflection at $q_y=0$ and $q_z=0$, is usually blocked with a beamstop to prevent damage to the detector since it is very intense.



Figure 10. Schematic of interparticle contraction observed by GISAXS.

1.8. Charge transport in NCs superlattices

Assembly of nanocrystals into a single component, binary, and even ternary form provide a controlled platform to systematically explore charge transport in semiconductor thin films by permitting studies of structure-property relationships.⁷⁴⁻⁷⁶ There is a large effort in device-oriented research involving copper chalcogenides NCs, especially those made of binary Copper chalcogenide nanocrystals. It is clear that for any real application electron transport through films of NCs has to be understood. In addition to the technological interest in NC solids, they are of fundamental interest for physics, since they form a new class of electron conducting materials in which the occupation of the NCs energy levels and their electronic interaction can be engineered. Specifically, in complex materials such as COINs, the coupling between the individual components is a crucial point. The temperature dependence of electronic conductivity forms a key characteristic in the study of transport in any system (superconductor, metal, an inorganic semiconductor, molecular conductor).

At high temperatures (>200 K), close-packed layers of monodisperse metal NC can exhibit an increase in resistance with increasing temperature, the behavior typical for metals.⁷⁷ It is often suggested the metal-like behavior of NCs assemblies may result from the large density of states at the Fermi level and from the predominant electron-phonon interactions. According to the Drude theory, the conductivity of a metal is given by

$$\sigma = ne^2\tau/m \quad (4)$$

where n is the density of conducting electrons and τ is mean free time. τ is determined by electron scattering, which can be categorized as elastic (impurity or defect scattering) and inelastic (electron-electron or electron-phonon scattering).

According to the Matthiesen rule,

$$\frac{1}{\tau} = \frac{1}{\tau_{elastic}} + \frac{1}{\tau_{inelastic}} \quad (5)$$

and the resistivity of metals can be written as

$$\rho(T) = \rho_0 + \rho_{ph}.$$

At very low temperatures, $\tau_{elastic}$ dominates since it is independent of temperature. At higher temperatures, $\tau_{inelastic}$ becomes significant and gives rise to a temperature-dependent conductivity. Assuming that the rate of inelastic scattering due to electron-phonon interactions increases as $\sim k_B T$, metallic conductivity decreases as $\sim 1/k_B T$ and resistivity increases linearly with T . Below the metal-insulator transition temperature, electrical resistivity exhibits metallic behavior. In order to understand the conduction mechanism in the metallic region, the experimental data should be fitted with the well-known empirical equation (Bloch-Grüneisen)⁷⁸

$$\rho(T) = \rho_0 + \rho_2 T^2 + \rho_5 T^5 \quad (6)$$

Where ρ_0 is the residual resistivity arising from grain boundary scattering, ρ_2 and ρ_5 due to the electron-electron scattering and mixed effects of electron-electron, electron-magnon and electron-phonon scattering processes, respectively. For metallic conduction process, both the grain boundaries and electron-electron scattering processes play important roles in the conduction process as $\rho_0 \gg \rho_2 \gg \rho_5$.

Electronic properties of granular materials have been extensively studied both theoretically and experimentally for several decades. The important pieces of the theoretical framework were put together by Mott, Efros and Shklovskii, Altshuler, and others.^{79, 80} Although our understanding of charge transport through NP assemblies is still evolving, several phenomena are known to be particularly important given the structure of the assemblies. These include tunneling, single-electron charging, hopping, varying wave function overlap, spatial and charge disorder, percolation effects, scattering, etc.⁸¹ Disorder plays an important role in the electronic properties of NC solids. For the disordered nanocrystal arrays, the temperature dependence of conductivity is inherently related to the disorder in the electronic structure.⁸² Small differences in size, shape, and position of the nanocrystals lead to variations in the energies of electrons (or holes) occupying the quantum-confined orbitals.⁸²

At lower temperatures, the carriers are localized on individual NCs and transport occurs by sequential tunneling; the electron hops from a particle to its nearest neighbor along the current path. Arrhenius type temperature dependence of conductivity $\log(G) \sim 1/T$ is characteristic of this transport regime. At even lower temperatures, below ~ 60 K the conductivity of Au and Ag NC layers scales as $\log(G) \sim 1/T^{1/2}$.^{77, 83} Tran et al. explained such behavior by inelastic cotunneling transport mechanism dominated by cooperative, multielectron hops that each go

to the nearest neighbor but are synchronized to move charge over distances of several particles.⁸³ The conduction mechanism in semiconductor NC solids strongly depends on the strength of interparticle coupling. Bulky capping ligands typically result in the activated nearest-neighbor hopping observed for several materials at near-room temperatures. Other mechanisms, including variable range hopping (VRH) with the Coulomb energy gap (so-called Efros-Shklovskii variable range hopping, ESVRH), have been recently proposed to explain nonArrhenius behavior observed in doped semiconductor NC solids.

VRH was originally developed for lightly doped semiconductors where the conductance is proportional to the probability of tunneling between sites separated by a distance r :

$$G \propto \exp\left(\frac{-2r}{\xi} - \frac{\Delta E}{k_B T}\right) \quad (7)$$

Where ξ is the localization length, which characterizes the tunneling probability between nearest sites; r is the hopping distance; ΔE is the energy difference between the initial and final sites. Mott pointed out that the energy difference ΔE is related to r as $\Delta E \sim 1/g_0 r^D$ if there is a constant DOS g_0 near the Fermi surface, where D (1, 2, or 3) is the dimension of the materials. Maximizing the probability leads to Mott's Law:

$$G \propto \exp\left(\left(\frac{-T_M}{T}\right)^{1/(D+1)}\right) \quad (8)$$

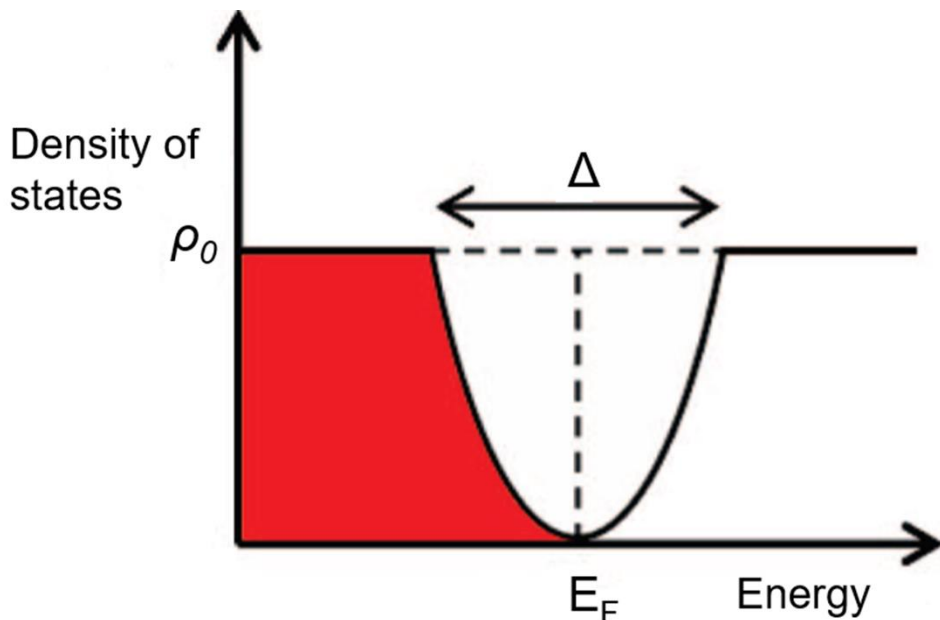


Figure 11. The density of states vs energy for a doped semiconductor exhibiting a soft Coulomb gap. The gap width is Δ .⁸⁴

In 3D, $\ln G$ is linearly proportional to $T^{-1/4}$ and $T_M = \frac{21.2}{k_B g_0 \xi^3}$

This $T^{-1/4}$ Mott's Law has been observed in various classes of lightly doped semiconductors. Nevertheless, a large body of literature reported $T^{-1/2}$ instead of Mott's Law regardless of the dimension of the materials. Efros and Shklovskii argued that the Coulomb interaction would open a soft gap in the DOS g_0 which leads to

$$G \propto \exp\left(-\sqrt{\frac{T_{ES}}{T}}\right) \quad (9)$$

In 1, 2, or 3 dimensions, T_{ES} is given by $T_{ES} = \frac{\beta e^2}{k k_B \zeta}$

k is a macroscopic dielectric constant and β is a numerical constant of the order of unity.

The Variable Range Hopping charge carrier transport mechanism in disordered NCs solids has been studied extensively.⁸⁰ Yu et al. and Wehrenberg et al. studied the temperature dependence of electrochemically charged CdSe and PbSe nanocrystal assemblies, respectively, in a temperature range of ~ 10 to ~ 150 K.^{85, 86} They concluded that the conductivity follows ES-VRH mechanism. Talapin and Murray studied the same PbSe NC system using a field-effect transistor (FET) setup and found $\ln \sigma \propto T^{-1/4}$.⁸⁷ Recently, Mentzel et al. presented more elaborate FET measurements on PbSe quantum-dot solids and concluded that the charge transport shows simple Arrhenius behavior, i.e. $\ln \sigma \propto T^{-1}$.⁸⁸ For copper sulfide (Cu_{2-x}S) film, Otelaja et al. found carrier transport mechanism from the temperature-dependent conductivities of the films reveals a Mott type Variable Range Hopping conduction mechanism for the temperature range 25 to 270K.⁸⁹

The unique physical and electrical transport properties of cu-based chalcogenides nanoparticles can be harnessed for game-changing innovations that impact a vast range of technological applications in electronic devices (for a comprehensive review see Coughlan et al.).²⁹ These include sensors, thermoelectrics, electrodes for lithium-ion batteries, supercapacitors, as well as photovoltaics, optoelectronics, photocatalysis, fluorescent biological imaging, and photothermal therapy.

1.9. Photodetection

Application of NCs in optoelectronic is receiving steadily growing attention. Under optical excitation above the band gap, the nanocrystals behave dramatically different compared to bulk

crystals as noted by Shabaev et al.⁹⁰ For applications requiring light absorption-emission in the near-IR region, inorganic NCs, especially those made of narrow-gap semiconductors, are in strong position to compete with other technologies, because their band gap can be precisely tuned from the visible spectral region to the wavelengths of 3500 nm. In such nanocrystals due to the absence of periodic boundary conditions, the conservation of momentum does not hold anymore and the efficiency of non-radiative Auger processes is increased such that it surpasses the efficiency of radiative recombination. Therefore, the energy released during the recombination of an electron-hole pair in the vicinity of another (photo-excited) electron in the conduction band is transferred to this electron with almost 100%.⁵² The photocurrent in a semiconductor can be generally described as:

$$i_{ph} = \eta e N_{\lambda} G_i \quad (10)$$

where η is the quantum efficiency (i.e., the number of excess carriers produced per absorbed photon), e is the elemental charge, N_{λ} is the number of photons of wavelength λ absorbed in the sample per unit time, and G_i is the internal (photoconductive) gain.

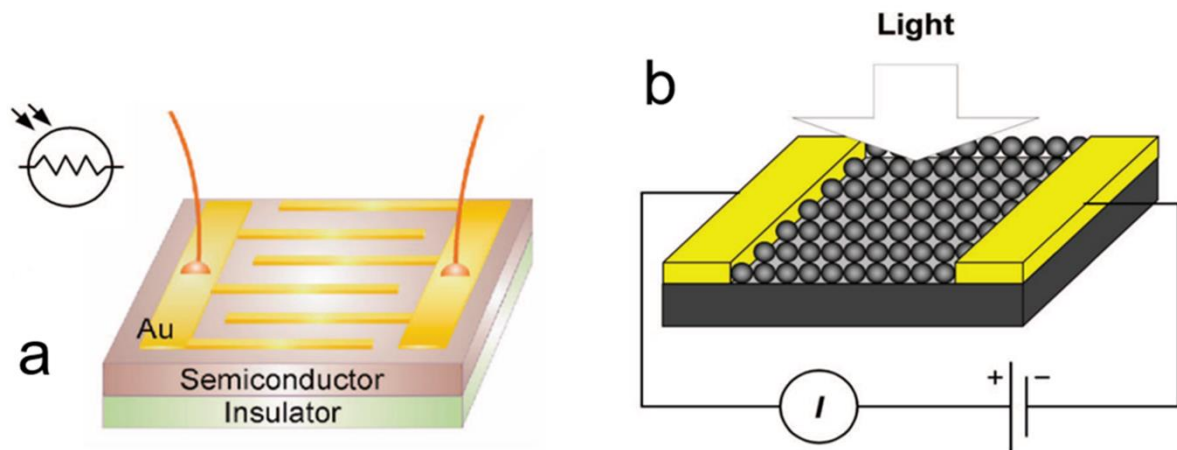


Figure 12. **a)** A sketch of typical thin film photoconductive photodetector. Interdigitate electrode structure is deposited onto the surface of active semiconductor. **(b)** A photodetector geometry that is typically used for NC-based devices: thin NC layer is deposited on top of the pre-patterned electrode structure. Au is shown as an example of metal contact material. (adapted from Talapin et al.)⁷⁰

Photoconductive gain is determined by the ratio between the free carrier lifetime (τ) and transit time (T_i): $G_i = \frac{\tau}{T_i}$. G_i is determined by the number of electrons flowing through the external circuit per each absorbed photon or, in other words, the number of cycles the majority carriers can make before recombining.

There are several figures of merits used to characterize photoconductive photodetectors. These are responsivity, spectral response, noise-equivalent power (NEP), detectivity, response time, and frequency response. Responsivity (R_i) is also often called sensitivity which provides a quantitative measure for the output signal such as photocurrent i_{ph} per watt of the input optical power P_{in} . R_i is the function of both modulation frequency (f) and photon wavelength (λ):

$$R_i(f, \lambda) = \frac{i_{ph}}{P_{in}} \quad (11)$$

Spectral response describes the spectral dependence of R_i , that is, the dependence of R_i versus λ . In NCs based photodetectors, the spectral response generally follows the shape of the NC absorption spectrum.

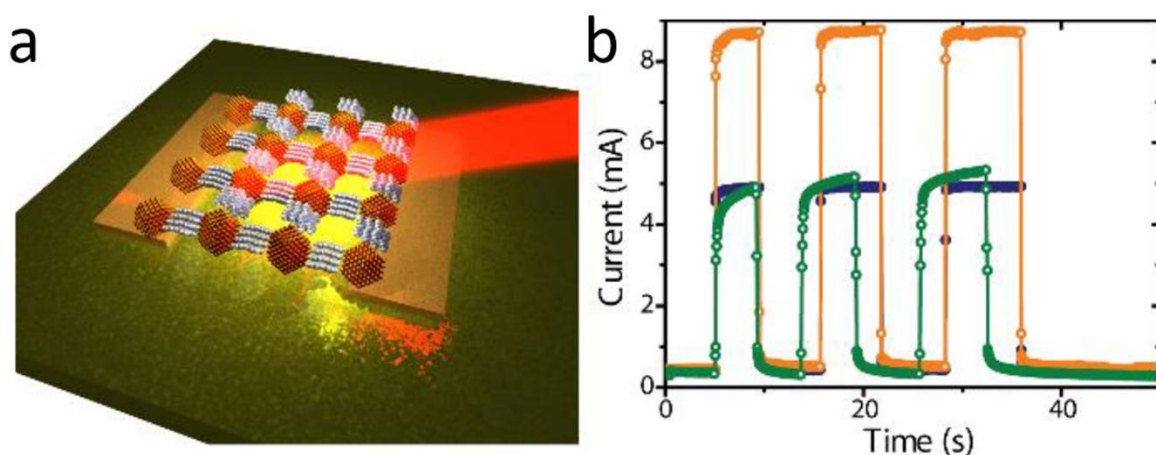


Figure 13. (a) Schematic representation of Cu-chalcogenide based CONIs assembly exciting with the suitable light source. (b) Photocurrent response upon exposure of different laser source with different optical power at a bias voltage of +200mV.

1.10. Application in Vapor Sensing

The NC surface functionalization with different capping ligands proving to be very important for the design and performance of sensitive nanosensors. Monolayer films of the organic molecular capped nanoparticle have recently attracted considerable attention due to their numerous novel emerging applications in chemical and biological sensing.^{52, 91} Since the first report on spraying alkanethiolate-protected nanoparticles as a metal-insulator-metal ensemble on chemiresistors for vapor sensing, a number of NC thin films have been demonstrated to be viable for chemical sensing.⁹² The architecture of these devices includes inorganic NCs

connected to each other through organic bridges. The NCs provide electric conductivity and, thus, enable simple electrical signal transduction. The organic film component provides sites for the selective sorption of vapor analyte molecules. A very interesting feature of these sensor materials is the possibility to control their properties through molecular level design. These nanostructures have demonstrated variable sensitivity and selectivity utilizing different linker molecules which make them promising for developing artificial noses and multivariable sensors.⁹³⁻⁹⁶

The attractiveness of functionalized NCs in sensing applications arises from the applicability of these nanostructures for different classes of gas and vapor analytes as well as the ability to produce NCs with different functional groups. Currently, the biggest limitation of NCs based sensors is the stability problem. The operational temperature ranges and the range of detectable compounds by such nanostructures also needs to be further improved. Array of metallic nanoparticles are the most common system which is explored for sensing purposes among which the Au, Ag, Pt, Pd, and Ni nanoparticles are the well-studied cases.^{92, 97-100} The choice of different metal compounds allows us to engineer the surface of nanoparticles and functionalize them with various and desired functional groups. The mechanism of vapor sensing in arrays of nanoparticles involves a variation of interparticle distance and dimension of the capping layer upon analyte absorption as well as the change in dielectric constant of the nanoparticles' environment.^{81, 101, 102} In the arrays where soft ligands separate nanoparticles from each other, the adsorption of the analyte can considerably affect the interparticle distance by changing the dimension length and geometry of capping organic molecules. In contrast, for the arrays of nanoparticles functionalized with rigid ligands, the interparticle spacing is not so sensitive to analyte adsorption; however, the charge transport can be still highly affected by the change in dielectric constant of the environment.¹⁰³

Part II

Results and discussion

2. Publication 1

Electronically Coupled, Two-Dimensional Assembly of $\text{Cu}_{1.1}\text{S}$ Nanodiscs for Selective Vapor Sensing Applications

Sonam Maiti^{1,2}, Santanu Maiti², Yvonne Joseph³, Andreas Wolf⁴, Wolfgang Brütting⁵, Dirk Dorfs⁴, Frank Schreiber^{2,6}, and Marcus Scheele^{1,6,}*

¹ Institute of Physical and Theoretical Chemistry, University of Tübingen, Auf der Morgenstelle 18, 72076 Tübingen, Germany.

² Institute of Applied Physics, University of Tübingen, Auf der Morgenstelle 10, 72076 Tübingen, Germany

³ Institute of Electronic and Sensor Materials, TU Bergakademie Freiberg, Gustav-Zeuner-Straße 3, 09599 Freiberg, Germany.

⁴ Institute of Physical Chemistry and Electrochemistry, Leibniz Universität Hannover, Callinstr. 3A, 30167 Hannover, Germany

⁵ Institute of Physics, University of Augsburg, Universitätsstrasse 1, 86159 Augsburg, Germany

⁶ Center for Light-Matter Interaction, Sensors & Analytics LISA+, University of Tübingen, Auf der Morgenstelle 15, 72076 Tübingen, Germany.

Abstract

We study temperature-dependent charge transport in two-dimensional assemblies of copper sulfide nanodiscs in the covellite crystal phase ($\text{Cu}_{1.1}\text{S}$). To enhance interparticle coupling, we cross-link the nanocrystals with the organic pi-system Cu-4,4',4'',4'''-tetraaminophthalocyanine and observe an increase in the conductivity by six orders of magnitude. The electrical properties of monolayers of this hybrid ensemble are consistent with a two-dimensional semiconductor and exhibit two abrupt changes at discrete temperatures (120 K and 210 K), which may be interpreted as phase changes. X-ray scattering experiments serve to study the importance of electronic conjugation in the organic pi-system *vs.* interparticle spacing for efficient charge transport. Applying the hybrid ensemble as a chemiresistor in organic vapor sensing experiments reveals a strong selectivity between polar and non-polar analytes, which we discuss in light of the role of the organic pi-system and its metal center.

Introduction

Two dimensional (2D) semiconductor materials (such as WS₂) have great potential for application in photodiodes, solar cells, photocatalysis, batteries, thermoelectric and light-emitting diodes.¹⁰⁴⁻¹⁰⁸ While the charge carrier mobility in single-crystalline grains may exceed that of crystalline silicon, it is challenging to synthesize these materials with macroscopic lateral domain sizes.¹⁰⁷ In contrast, granular ensembles of 2D conductors can be obtained in large quantities and assembled into macroscopic thin films, however with significantly lower mobilities.¹⁰⁹ Charge carrier transport in such granular 2D materials occurs typically via hopping, which was first described by Mott with the concept of variable-range hopping (VRH), assuming that carriers hop between localized states over a characteristic, temperature-dependent hopping distance.^{79, 110} While the density of states (DOS) is considered to be constant in this model, the electrical conductivity varies with temperature as $\sigma(T) = \sigma_0 \exp[-(T_{Mott}/T)^x]$. Here, T is the absolute temperature, σ_0 the attempt frequency for a hopping event, T_{Mott} the characteristic Mott temperature, and $x = 1/(D + 1)$, where D is the dimensionality of the conductor. Thus for a 2D material, $\ln \sigma$ is proportional to $T^{-1/3}$. Efros and Shklovskii later pointed out that for sufficiently low temperatures, the DOS near the Fermi level (E_F) is not constant and Coulomb interactions give rise to a soft gap in the density of states. In this regard, it has been demonstrated that the DOS near E_F vanishes linearly with energy for a 2D system.^{80, 111, 112} This has been explained with the electron-hole Coulomb interaction to be overcome when an electron hops from one site to another.¹¹³ For this ES VRH mechanism, the conductivity varies with temperature as $\sigma(T) = \sigma_0 \exp[-(T_{ES}/T)^{1/2}]$. Here, $\ln \sigma$ is always proportional to $T^{-1/2}$ regardless of the dimensionality of the system, which merely affects the characteristic temperature T_{ES} .¹¹⁴ Therefore for a granular 2D semiconductor, one can expect $\ln \sigma \sim T^{-1/2}$ for sufficiently low temperatures and $\ln \sigma \sim T^{-1/3}$ for higher temperatures.

In this work, we use this characteristic behavior to examine under which conditions ensembles of covellite nanocrystals (Cu_{1.1}S NCs) behave collectively like a 2D semiconductor. We chose Cu_{1.1}S due to its low toxicity and rich redox chemistry, which renders it attractive for environmentally benign applications in optoelectronics and sensing.^{37, 115, 116} Previous attempts to tune the transport properties of copper sulfide NC ensembles employed thermal doping, electrophoretic deposition and/or ligand exchange with small molecules, such as 1, 2-ethanedithiol (EDT), hydrazine, mercaptopropionic acid or ethylenediamine.^{2, 89, 117-119}

Depending on the surface modification, Copper sulfide NC ensembles have displayed 3D VRH transport, Arrhenius-type, nearest neighbour hopping or non-monotonic temperature dependencies.^{2, 89} Typical conductivities ranged between 10^{-4} S cm⁻¹, 10^{-2} S cm⁻¹ and 75 S cm⁻¹ for EDT-functionalization, treatment with hydrazine and electrophoretic deposition, respectively. Here, we take a different approach towards increasing electronic coupling in Cu_{1.1}S NC films by functionalizing their surface with the relatively large (1.2 nm), but fully conjugated molecule Cu-4,4',4'',4''',4''''-tetraaminophthalocyanine (Cu4APc) similar to other types of coupled organic-inorganic nanostructures.⁵² We discuss the transport behavior of this hybrid material in the context of potential 2D Mott VRH and demonstrate its perspectives for solvent vapor sensing.

2. Methods

2.1. Synthesis of Cu_{1.1}S Nanocrystals: Cu_{1.1}S NCs were prepared by adapting the heat-up synthesis procedure from Xie et al.³⁶

2.2. Synthesis of Ligands: Cu-4,4',4'',4''',4''''-tetraaminophthalocyanine (Cu4APc) was synthesized following a previously reported procedure.¹²⁰ For the structural formula, see **Figure S2.1**.

2.3. Thin-Film Preparation and Ligand Exchange: In this work, electronically coupled, ordered NC superlattice films were assembled at the liquid/air interface.^{4, 121} Initially, the native oleylamine passivated, disc-shaped Cu_{1.1}S NCs (diameter of 12.7 ± 1.7 nm, and a thickness of 5.8 ± 0.7 nm) film was prepared by controlling the evaporation of toluene solvent in DMSO solution in a home-built teflon chamber. A reference sample was prepared by transferring this film on to a Si-substrate. For Cu4APc cross-linked NCs, a solution of Cu4APc in DMSO was slowly injected into the subphase by a syringe in order to ligand-exchange the assembled NC film floating above the DMSO phase. Finally, the free-floating ligand-exchanged NC superlattice was transferred to substrates by retracting the solution from the bottom of the chamber (**Figure S2.2**).

2.4. Instrumentation: Scanning transmission electron microscopy (STEM, Hitachi SU 8030 microscope operating at 30 kV) was employed to determine the particle size and shape. Optical measurements were performed on solid state films on glass substrates using an UV-vis-NIR

spectrometer (Agilent Technologies, Cary 5000). Grazing-incidence small-angle X-ray scattering (GISAXS)⁵³ was carried out with a laboratory instrument (Xeuss 2.0, Xenocs, France) using Cu K α radiation ($\lambda = 1.5418 \text{ \AA}$). The samples were probed with a focused X-ray beam of size $0.5 \times 0.5 \text{ mm}^2$ at incidence angle of 0.22° . The GISAXS images were collected with a 2D Pilatus 300K, having 487×619 pixels. The detector was placed at a distance of 2496 mm, determined using Ag-behenate as reference sample. X-ray reflectivity (XRR) data from the sample was collected in specular geometry with a laboratory source (Cu K α ; GE Inspection Technologies, Germany). The surface morphology was measured by AFM using a JPK Nanowizard II instrument in tapping mode under ambient conditions. Image analysis was performed with Gwyddion. Raman spectra were acquired using a Horiba Jobin Yvon Labram HR 800 spectrometer with a CCD- 1024×256 -OPEN-3S9 detector. Excitation for Raman was performed using a He:Ne laser (wavelength 633 nm). Electrical measurements were performed in a glovebox at room temperature with a homemade probe station using a Keithley 2634B dual source-meter unit, controlled by the included test script builder program. The NC films after ligand exchange were deposited on commercially available bottom-gate, bottom-contact transistor substrates (Fraunhofer Institute for Photonic Microsystems, Dresden, Germany) with interdigitated Au electrodes of 10 mm width and $2.5 \text{ }\mu\text{m}$ channel length followed by annealing at $250 \text{ }^\circ\text{C}$ for 2 h under nitrogen atmosphere. The temperature-dependent charge transport properties of the NC thin-films were measured by a Lake-Shore CRX-6.5K probe station, equipped with a Keithley 2636B dual source-meter unit and a Lake Shore temperature controller (model 336). For investigating the vapor sensing properties, the NC films were deposited on commercially available glass substrates with interdigitated gold electrode structure (90 finger pairs, $10 \text{ }\mu\text{m}$ microelectrode gap and a circular area with a diameter of 3.5 mm ; “ED-IDE1-Au” by micrux Technologies). The sensitivity of the films was characterized by dosing them with vapors of 4-methyl-2-pentanone (4M2P), toluene, isopropanol, and water while monitoring their resistances at 0.1 V. All vapor sensing experiments were carried out at room temperature (ca. $25 \text{ }^\circ\text{C}$) at a flow rate of 400 mL min^{-1} . As all vapors have comparable vapor pressures (21, 29, 20, and 23 mbar at $20 \text{ }^\circ\text{C}$, respectively)¹²², differences in the response of the samples are expected to arise mainly from their chemical nature (polarity and structural features) and not from the differences in vapor pressure.

3. Results

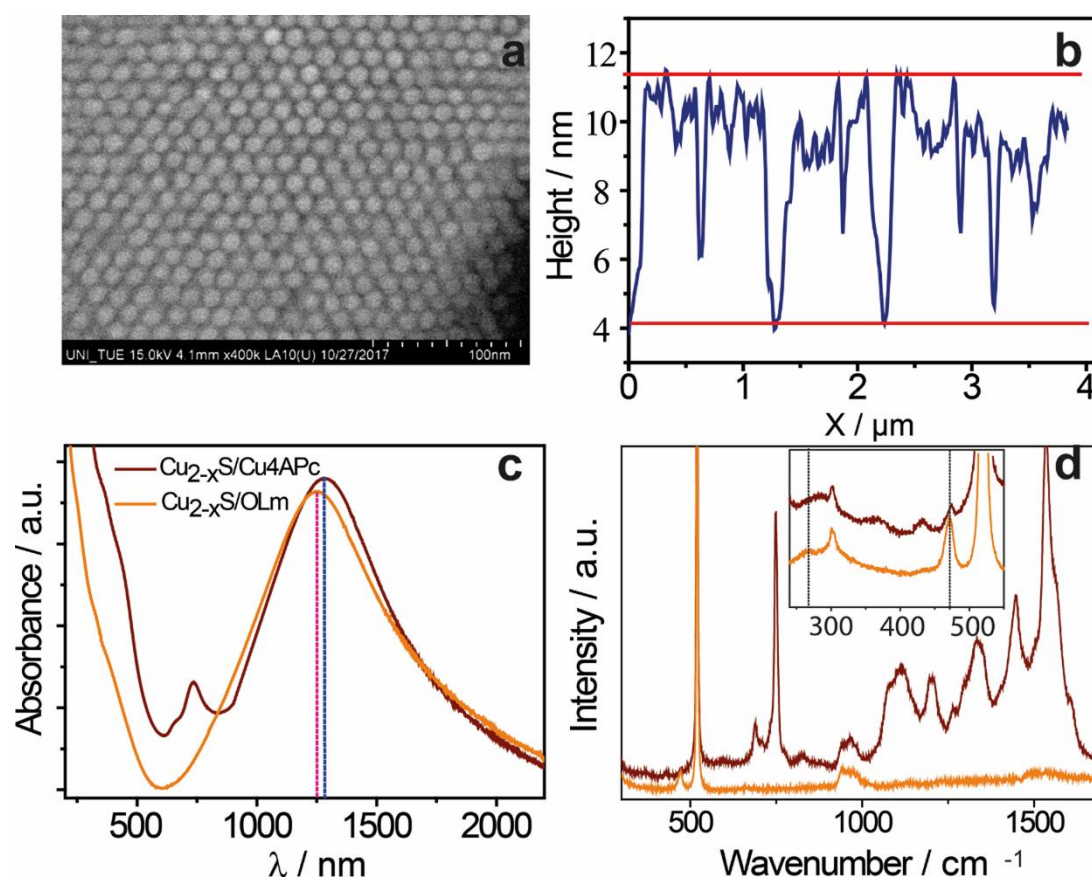


Figure 2.1. (a) SEM image and (b) height profile of a typical Cu_{1.1}S /Cu4APc film determined by atomic force microscopy (see **Figure S2.3b** for the original image). (c) UV-Vis-NIR absorption spectra of as-prepared Cu_{1.1}S superlattice before and after ligand exchange (orange and dark red curves, respectively). (d) Raman spectra of as-prepared Cu_{1.1}S nanocrystal thin films before and after ligand exchange (same color code as in (c)). The inset highlights the spectral regime around the S-S stretching bands.

Figure 2.1a depicts a typical SEM image of Cu4APc cross-linked Cu_{1.1}S NCs assembled into a hexagonal superlattice. The disk-shaped NCs have an average diameter of 12.7 ± 1.7 nm and a thickness of 5.8 ± 0.7 nm as determined from high resolution scanning electron micrographs (**Figure S2.3a**). Height profiles obtained by atomic force microscopy (AFM, **Figure 2.1b** and **Figure S2.3b**) show that the average superlattice thickness is one monolayer (6 nm). **Figure 2.1c** displays the UV-Vis-NIR spectra of the as-prepared Cu_{1.1}S NCs before (orange) and after ligand exchange with Cu4APc (dark red) on quartz substrates. The strong NIR absorption with a maximum around 1250 nm is characteristic for a localized surface plasmon resonance (LSPR)

due to copper vacancies.^{45, 46, 123} In addition, the ligand exchanged film displays a new peak at 736 nm corresponding to the appearance of the singlet absorption of Cu4APc.¹¹⁴ Raman spectroscopy provides further evidence for a successful ligand exchange (**Figure 2.1d**). While the vibrational spectrum of the as-prepared Cu_{1.1}S NCs before ligand exchange (orange curve) features mainly a weak band at 265 cm⁻¹ (see inset) and a sharp band at 471 cm⁻¹ due to S–S stretching vibrations, additional bands at 747, 1115, 1345, 1447, 1535 and 1605 cm⁻¹ appear after ligand exchange with Cu4APc^{124, 125} (Note: The bands observed near 521 cm⁻¹ and 966 cm⁻¹ correspond to the optical phonon modes of the Si substrate). Furthermore, the S–S stretching bands shift to 267 and 474 cm⁻¹ (see inset), which is often attributed to a binding interaction with the surface of the particles. These Raman spectra for both films are in good agreement with the existing literature on crystalline Cu_{1.1}S NCs.^{124, 126}

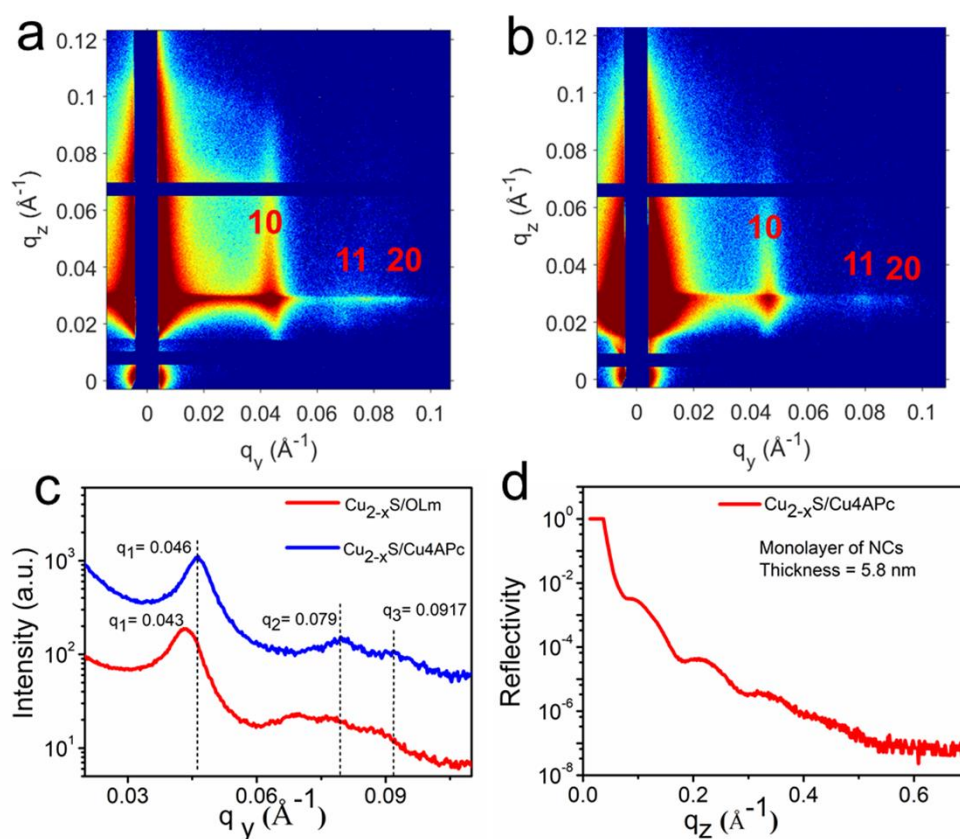


Figure 2. (a) GISAXS patterns of self-assembled Cu_{1.1}S NDs coated with OA. (b) GISAXS pattern of Cu4APc ligand induced assembly Cu_{1.1}S NDs. Both patterns show long-range highly ordered 2D hexagonal superlattices. (c) The extracted line profiles from the corresponding GISAXS images along in-plane wave vector q_y . To improve the statistics of the line profiles the signals were integrated along the q_z direction. (d) X-ray reflectivity profile of Cu_{1.1}S/Cu4APc film.

The structural changes of the $\text{Cu}_{1.1}\text{S}$ NC superlattice before and after ligand exchange are determined by GISAXS on Si-substrates in **Figure 2.2a** and **2.2b**. The appearance of several intense scattering truncation rods, extended along the q_z -direction at different q_y -positions corresponds to a long-range ordered monolayer superlattice formation for both cases. The ratio of the relative peak positions is $1: \sqrt{3}: 2$ - which is a characteristic of two-dimensional hexagonal superlattices for both cases and can be indexed with 10, 11 and 20 superlattice planes.¹²⁷ The significant changes of the correlation peak positions along the q_y -direction for both samples are additionally displayed with line profiles (**Figure 2.2c**). The lattice constants, which equal the nearest-neighbor distance in hexagonal lattices, are 16.8 ± 0.1 nm and 15.7 ± 0.1 nm before and after ligand exchange, respectively. We attribute the decrease of 1.1 nm to the effect of replacing the larger oleic acid ligand (~ 2 nm) by the more compact Cu4APc (~ 1.2 nm) molecule. The XRR profile in **Figure 2.2d** features multiple Kiessig oscillations, from which we determine the thickness of the NC film on the substrate to 5.8 nm, in good agreement with our AFM data.¹²⁸

For charge transport studies, the $\text{Cu}_{1.1}\text{S}$ NC films were deposited on Si-substrates with pre-patterned gold contacts. Since the I/V characteristics were slightly field-dependent, all conductivities were measured in the low-field regime by fitting the linear current response to a voltage sweep from -200 mV to +200 mV (See **Figure S2.4+5**). We find an enhancement by six orders of magnitude after ligand exchange with Cu4APc in the electrical conductivity of the NC superlattice, providing clear evidence for the improved coupling. To determine the transport mechanism in the 2D superlattices of NCs before and after ligand exchange, we perform temperature-dependent conductivity measurement from 30 to 300 K in **Figure 2.3a**. In both cases, σ of the film increases with increasing temperature, which is the typical behavior of a semiconductor. However, as evident for the unexchanged sample and – to a lesser degree – for the Cu4APc-functionalized NCs as well (inset in **Figure 2.3a**), $\sigma(T)$ deviated from a simple monotonic increase, implying that the charge transport cannot be described by a single hopping model. While the origin of this anomaly is not clear, it has been observed before for arrays of $\text{Cu}_{1.1}\text{S}$ and tends to be more pronounced for less coupled NCs.^{2, 129} The deviation from a single hopping model is further evidenced for the Cu4APc-capped $\text{Cu}_{1.1}\text{S}$ films in **Figure 2.3b**, where we plot the $\sigma(T)$ -data according to $\ln \sigma = \ln \sigma_0 - \left(\frac{T_0}{T}\right)^{1/x}$ with $x = 1, 2, 3$ or 4. Evidently, none of the common temperature coefficients results in a satisfactory fit over the entire temperature range. To exemplify this, we display linear fits to the data as dashed lines. For $x = 2, 3$ and 4, this satisfactorily describes the data at low temperatures (30 – 120 K), but

increasingly deviates from a simple linear relationship (in this mode of plotting the data) above this range. For $x = 1$, no linear relationship over a reasonably large temperature window could be established.

Another way of testing a certain transport mechanism is to plot the derivative $d(\log \sigma)/d(\log T)$ against $\log T$ as illustrated in **Figure 2.3c**¹³⁰ and determining x from the slope, m , of a linear fit to the data as $x = -1/m$. The unusual, non-monotonic $\sigma(T)$ behavior is readily visible in this plot with three distinct temperature regimes, namely 30-120 K, 120-210 K and 210-300 K, which are separated by abrupt changes in the derivative $d(\log \sigma)/d(\log T)$.

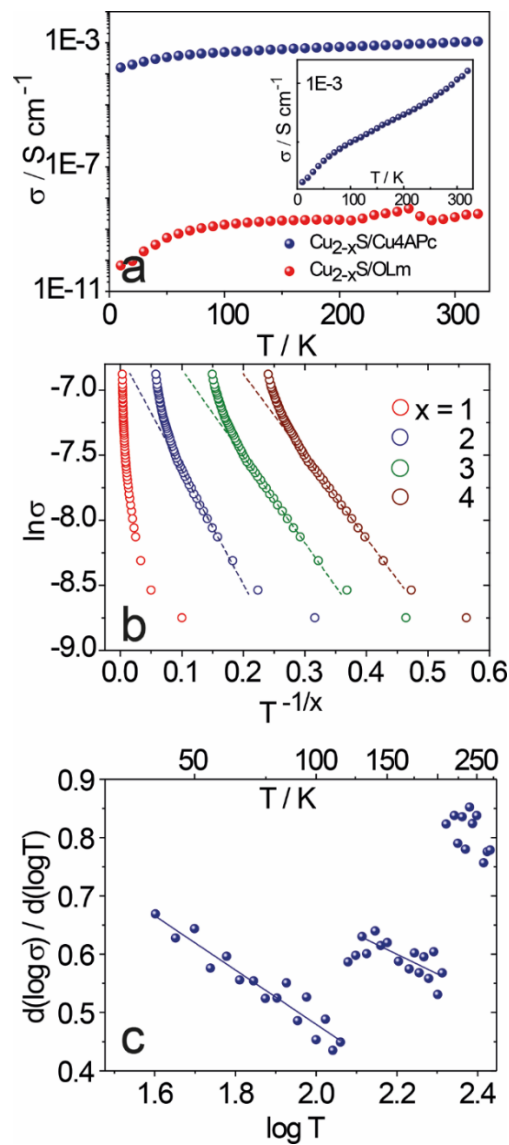


Figure 2. 3(a) Temperature-dependent electrical conductivity measurement of $\text{Cu}_{1.1}\text{S}$ nanocrystal films from 30 to 320 K. Red circles: OLm-capped $\text{Cu}_{1.1}\text{S}$ NC films and blue circles: $\text{Cu}_{1.1}\text{S}$ NC films

crosslinked with Cu4APc. Inset: linear plot of the Cu4APc-capped Cu_{1.1}S film for better visualization. **(b)** $\ln \sigma$ vs. $T^{-1/x}$ for $x = 1-4$ as assigned by the color legend for Cu_{1.1}S NC films crosslinked with Cu4APc. Dashed lines are linear fits for a fixed temperature window of 30 – 120 K. **(c)** Derivative $d(\log \sigma)/d(\log T)$ vs. $\log T$ for the same dataset as in **(b)**. Solid lines are linear fits for fixed temperature windows of 30 – 120 K and 120 – 210 K, respectively.

We note several previous reports about presumed phase transitions in copper sulfide at low temperatures, which we tentatively hold responsible for our observation.^{2, 129, 131} Between 30-120 K, we find $x = 2.1$ and a reasonable R-squared confidence of 90 %, suggesting a VRH ES transport mechanism in this temperature window. For 120-210 K, the slope notably flattens and we derive $x = 3.0$ in excellent agreement with Mott 2D VRH. However, an R-squared confidence of only 53 % cannot entirely rule out the possibility of Mott 3D VRH due to the small differences between the two mechanisms in the expected slope. Above 210 K, the R-squared confidence decreases to 18 % and a meaningful fit becomes impossible. We suspect that this may be due to the already mentioned anomaly in this temperature range (see **Figure 2.3a**).

In addition to studying the transport characteristics of Cu_{1.1}S/Cu4APc monolayers, we seek to take advantage of the high active surface area of the material for vapor sensing. The basic idea is that adsorption of vaporized molecules on and into the Cu_{1.1}S/Cu4APc monolayer may induce a change in resistance, which serves as feedback for sensing. **Figure 2.4a** presents the typical resistance change ($\Delta R/R_0$) at room temperature upon exposure to 4M2P vapor with concentrations in the range of 100 - 5000 ppm (three exposure cycles of 120 seconds each). We observe a fast (few seconds) and fully reversible, approximately rectangular response, which increases with increasing analyte concentration at the same operating temperature and 0% relative humidity. Four types of vapor analytes are used in this study, i.e. 4M2P, Toluene, 1-Propanol and water to check the chemical selectivity. **Figure 2.4b** compares the response of the NC film to these four analytes after exposure to 5000 ppm. While toluene vapor exhibits a significant but slightly weaker response compared to 4M2P vapor, the two polar analytes 1-propanol and water invoke almost no response.

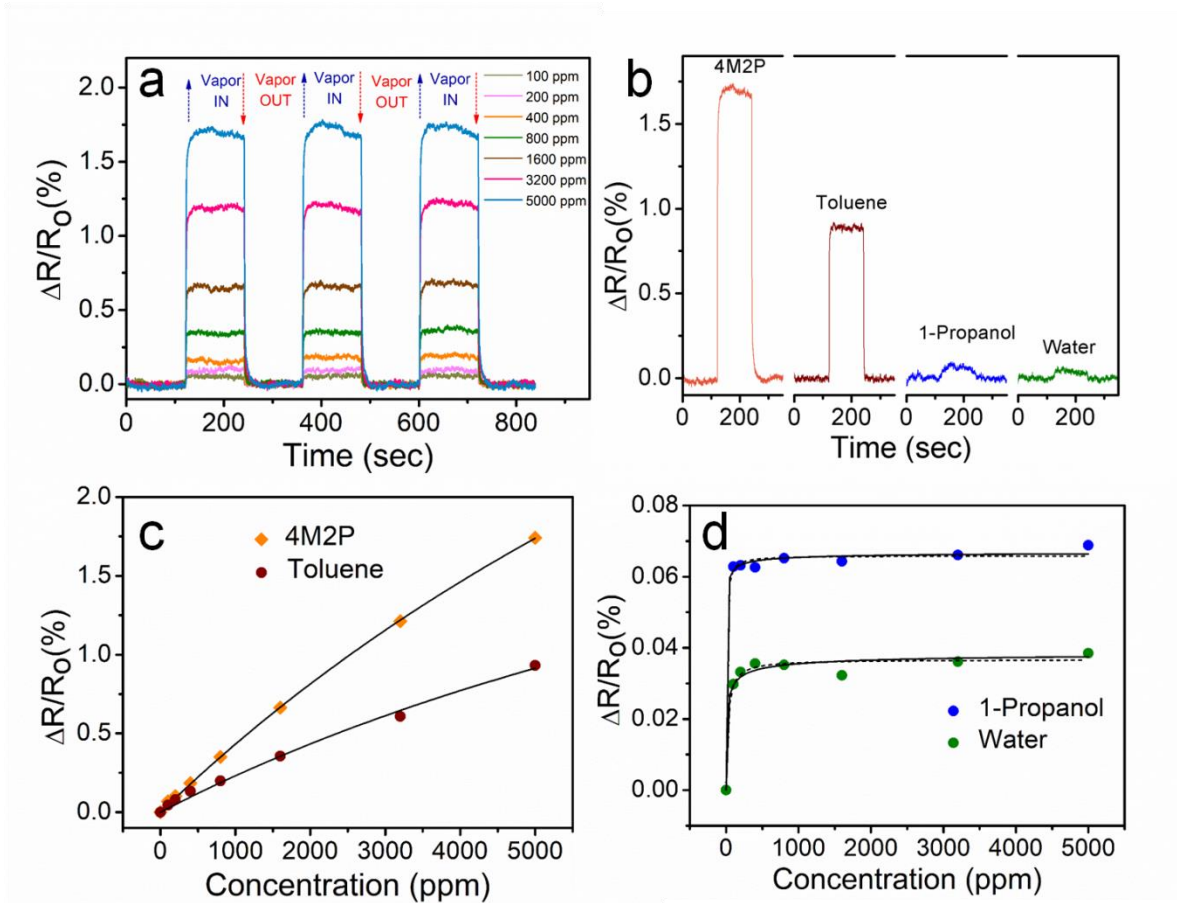


Figure 2.4. (a) Transient vapor response traces of $\text{Cu}_{1.1}\text{S}/\text{Cu4APc}$ film toward 100 to 5000 ppm of 4M2P at 0% relative humidity. (b) Responses of the $\text{Cu}_{1.1}\text{S}/\text{Cu4APc}$ films to exposure with 5000 ppm 4M2P vapor, toluene vapor, water vapor, and 1-propanol vapor. (c) Response amplitudes plotted versus the gas-phase concentration of 4M2P and toluene. (d) Response amplitudes plotted versus the gas-phase concentration of 1-propanol and water. The solid lines are the Langmuir fits according to a 1st order adsorption model (i.e. equation 2.1) and the dashed lines are the Langmuir fits according to a 2nd order adsorption model (i.e. equation 2.2).

We gain further insight into the sensor response and analyte/film interactions by fitting the concentration-dependent change in resistance for all four analytes with a Langmuir adsorption using the equation

$$\frac{\Delta R}{R_0} = \left[\frac{\Delta R}{R_0} \right]_s \frac{K_b C_{\text{vapor}}}{1 + K_b C_{\text{vapor}}} \quad (2.1)$$

where $[\Delta R/R_0]_s$ and K_b are the relative change of resistance at saturation and the binding constant, respectively, and C_{vapor} is the concentration of the analyte in the gas phase.¹²²

We find that the 1st order Langmuir adsorption model in equation (2.1) reflects well the behavior for 4M2P and toluene as displayed in **Figure 2.4c**. In contrast, no satisfactory fits

could be obtained in this way for the analytes 1-propanol and water, which is why we applied a 2nd order Langmuir adsorption model according to equation (2.2), which described the experimental data more adequately (**Figure 2.4d**).

$$\frac{\Delta R}{R_0} = \left[\frac{\Delta R}{R_0} \right]_s \frac{K_b \sqrt{C_{vapor}}}{1 + K_b \sqrt{C_{vapor}}} \quad (2.2)$$

The fitting parameters, such as the relative differential resistance responses at saturation $[\Delta R/R_0]_s$ and the binding constants K_b obtained from the 1st and 2nd order Langmuir adsorption model for all four analytes at room temperature are given in Table 1.

Table 1. The experimental sensor responses i.e. relative changes of resistance at saturation $[R/R_0]_s$ and binding constants K_b obtained from the Langmuir fits for $\text{Cu}_{1.1}\text{S}/\text{Cu}_4\text{APc}$ thin films at room temperature.

NC Film	Analyte	$[\Delta R/R_0]_s$ (%)	K_b
$\text{Cu}_{1.1}\text{S}/\text{Cu}_4\text{APc}$	4M2P	7.13	$6.43602\text{E-}5$ (M^{-1})
	Toluene	3.51	$7.03732\text{E-}5$ (M^{-1})
	1-propanol	0.067	1.11619 ($\text{M}^{-0.5}$)
	Water	0.039	0.29583 ($\text{M}^{-0.5}$)

4. Discussion

In addition to providing evidence for the chemical modifications, the spectroscopic data in **Figure 2.1** also highlights the structural changes occurring in the NC ensemble during surface functionalization with Cu_4APc . We attribute the 34 nm red-shift of the LSPR transition to a reduced interparticle distance due to the shorter length of Cu_4APc (12 Å) compared to oleylamine (20 Å). As the interparticle spacing narrows, dipole–dipole interactions between the NCs strengthen, which is known to cause a red-shift in the LSPR band.¹³² In addition, alterations in the dielectric environment of the NCs by the new surface chemistry can also affect the position of the LSPR. The anticipated contraction of the interparticle spacing is quantified by the GISAXS data in **Figure 2.2** to a net decrease of 11 Å. It is noteworthy that

even after this contraction, the average interparticle spacing is $30 \pm 17 \text{ \AA}$ and, thus, the NCs remain spatially well separated. In this light, the room-temperature conductivity of 1 mS cm^{-1} is quite remarkable (**Figure 2.3a**) and even higher than that of EDT treated $\text{Cu}_{1.1}\text{S}$ NCs, despite the much shorter length of the molecular linker (4 \AA).²⁰ In addition, the conductivity increase by six orders of magnitude following the interparticle contraction during ligand exchange highlights the sensitivity of the material towards further structural changes, such as those induced by swelling upon exposure to a solvent vapor. To test this idea, we chose the four vapor analytes investigated in **Figure 2.4**, which differ significantly in their chemical affinity and permittivity (toluene: 2.4 (hydrophobic), 4M2P: 13.11 (hydrophilic), 1-propanol: 20.8 (H-bonding) and water: 80.1 (polar H-bonding)).¹³³ As detailed in Table 1, the Cu4APc-capped $\text{Cu}_{1.1}\text{S}$ NC monolayers are significantly more sensitive towards analytes of low permittivity (4M2P and toluene), while the two polar analytes 1-propanol and water bind more strongly to the film as indicated by the larger binding constants K_b (Table 1) as well as the strong curvature of the response (**Figure 2.4d**).¹³⁴

We consider several possible reasons for the different behavior of 4M2P/toluene vs. 1-propanol/water: (1) Water and 1-propanol are quite small and compact molecules, such that swelling effects exerted by these species are expected to be relatively small. (2) As shown in previous findings by Olichwer et al. on hydrophobic superlattices of dodecanethiol (DDT)-stabilized Au NCs, 1-propanol adsorbs predominantly on the surface of the film with little contribution to film swelling.¹³⁵ However, Cu4APc is significantly less hydrophobic than DDT, such that this reasoning may not fully apply here. (3) The metal center of tetraaminophthalocyanines possess a high affinity towards 1-propanol and water.¹³⁶ With just one metal per molecule, we expect this particular binding site to saturate quickly, even at low dosing concentrations. As a very crude estimate, one may expect 3 molecules per nm^2 on the surface of each nanocrystal,¹³⁷ corresponding to 300 metal center binding sites as an upper limit. Considering the active area of the interdigitated electrodes of the transducer (38.5 mm^2) and assuming a monolayer coverage with $\text{Cu}_{1.1}\text{S}$ particles (diameter: 12.7 nm) with hexagonal packing (74 % fill fraction) yields $5.6 \cdot 10^{10}$ particles, corresponding to $1.7 \cdot 10^{13}$ metal center binding sites in the entire active area. At room temperature, there are roughly $2.5 \cdot 10^{22}$ gas molecules/L and, thus, $2.5 \cdot 10^{18}$ 1-propanol/water molecules per Liter at a dosing concentration of 100 ppm. At a flux of 400 mL/min, saturation is expected instantaneously for this scenario after roughly 1 ms of exposure time in agreement with our observations (see

Figure 2.4b+d). Such small density of binding sites could possibly enable very low limits of detection as indicated by **Figure 2.4d**, provided a sufficient signal-to-noise ratio.

In contrast, for the nonpolar analytes toluene and 4M2P, a strong affinity to the phthalocyanine metal center does not exist such that they are weakly adsorbed within the nonpolar ligand matrix and invoke swelling of the NC film. This induced expansion of the interparticle spacing is expected to significantly increase the resistance (as demonstrated in **Figure 2.3a**), which appears to be the major sensing mechanism for this material, explaining the selectivity for the two analytes toluene and 4M2P.^{110, 122} The magnitude of the relative response should be viewed in the context of the very thin layer thickness of ≤ 10 nm, a fast recovery of the sensors within a second time regime and a nearly rectangular sensor response. Thicker films may exhibit a stronger, but slower sensing response. In comparison with other previously reported chemiresistors based on NC ensembles for room temperature vapor sensing, these preliminary sensing measurements are encouraging. For instance, networks of Au NCs cross-linked with a variety of alkanethiols have shown $\Delta R/R_0$ -values between 0.1-10 % but suffer from gradual degradation in air due to oxidation of the thiol cross-linkers.^{122, 134, 138-140} Utilizing more durable tin-doped indium oxide NCs yielded $\Delta R/R_0$ -values of 2-3 %.^{141, 142} Higher values of 80 – 500 % are typically only obtained for very large analyte concentrations or at elevated temperatures (300 °C).^{143, 144} For example, ZnO nanoflowers decorated with Au NCs have been reported to exhibit a $\Delta R/R_0$ of 7500 % towards 100 ppm acetone, however only at a working temperature of 270 °C.¹⁴⁵ The material investigated in the present paper is operative under ambient conditions, unoptimized and holds the potential for selective vapor sensing at low detection limits due to its heterostructure as outlined above.

The temperature-dependent transport data of Cu4APc-capped Cu_{1.1}S NC monolayers in **Figure 2.3** are consistent with the picture of a two-dimensional conductor. At low temperatures ($30 < T < 120$ K), the transport mechanism is satisfactorily described with ES VRH, supposedly because of the dominant effect of Coulomb interactions and the opening of a soft gap in the density of states. At higher temperatures, this Coulomb gap closes and the transport data is more adequately described with Mott VRH as indicated by the slope of 3.0 for $d(\log \sigma)/d(\log T)$ vs. $\log T$ (**Figure 2.3c**). As detailed in the introduction, this is the expected behavior for a granular 2D conductor.

We note that the transport properties of Cu4APc-capped Cu_{1.1}S NC films are different from those detailed by Bekenstein et al. for the same type of NCs but different surface ligands, such

as thiols of different chain lengths or mercaptopropionic acid, who exclusively found Arrhenius-type NNH over the whole temperature range.² In view of the quasi-two dimensional structure of the films and the relatively large conductivity provided by the conjugated Cu4APc cross-linkers, we suspect that this altered transport behavior may be due to a combination of the unique geometry of the material as well as enhanced coupling between the NCs. This and the large interparticle spacing (30 ± 17 Å) are ideal for resistance-mediated sensing applications of vapors, operating with adsorption and swelling effects, which we have demonstrated with the vapor sensing measurements in **Figure 2.4**. Comparative electric transport measurements using thicker films (5-10 monolayers) yield 2-3 orders of magnitude smaller electric conductivities, which we attribute predominantly to large structural inhomogeneities as well as a potentially incomplete ligand exchange (**Figure S2.6**).

CONCLUSION

We assemble Cu_{1.1}S NCs capped with the organic pi-system Cu4APc at the air-liquid interface into a quasi-2D thin film with significant long-range order and electronic coupling. The coupling is evidenced by a six orders of magnitude enhancement in the conductivity as a result of the ligand exchange. Temperature-dependent electrical transport measurements are discussed in the context of two-dimensional variable range hopping, the effect of the quasi-2D structure, and the presence of the conjugated linker. Resistivity-based vapor sensing measurements reveal a selective sensitivity for non-polar analytes, which is facilitated by a large interparticle spacing of 30 ± 17 Å. The results of this study show how combining organic pi-systems and copper-deficient covellite NCs rewards electrically conductive, quasi-2D films, which are solution-processible and attractive for vapor sensing applications.

ACKNOWLEDGMENTS

The authors acknowledge the DFG for support under Grants SCHE1905/3, SCHE1905/4, BR1728/18 and SCHR700/25. We also thank Mrs. Elke Nadler, Institute of Physical and Theoretical Chemistry, University of Tübingen, for performing SEM/STEM measurements using a Hitachi SU 8030 SEM which was funded by the DFG under contract INST 37/829-1 FUGG, partially.

Corresponding Author:

*email: marcus.scheele@uni-tuebingen.de

Author Contributions:

The manuscript was written through contributions of all authors. All authors have given approval to the final version of the manuscript.

Supplementary Material:

This material is available free of charge *via* the Internet at <http://pubs.acs.org>.

Structural formula of Cu₄APc; schematics of the ligand exchange procedure at the liquid/air interface; high magnification STEM and AFM image of the Cu_{1.1}S NC film; current-voltage (I-V) curves before and after ligand exchange and the evaluation of contact resistance applying transmission line method (TLM); field-dependence of the I/V characteristics; Transport characteristics of thicker films

3. Publication 2

Dye-Sensitized Ternary Copper Chalcogenide Nanocrystals: Optoelectronic Properties, Air Stability and Photosensitivity

*Sonam Maiti^{1,2}, Santanu Maiti², Ali Hossain Khan^{3,4}, Andreas Wolf⁵, Dirk Dorfs⁵, Iwan Moreels^{3,4}, Frank Schreiber^{2,6} and Marcus Scheele^{1,6} **

¹ Institute of Physical and Theoretical Chemistry, University of Tübingen, Auf der Morgenstelle 18, 72076 Tübingen, Germany.

² Institute of Applied Physics, University of Tübingen, Auf der Morgenstelle 10, 72076 Tübingen, Germany

³ Istituto Italiano di Tecnologia, Via Morego 30, 16163 Genova, Italy

⁴ Department of Chemistry, Ghent University, Krijgslaan 281-S3, 9000 Gent, Belgium

⁵ Institute of Physical Chemistry and Electrochemistry, Leibniz Universität Hannover, Callinstr. 3A, 30167 Hannover, Germany

⁶ Center for Light-Matter Interaction, Sensors & Analytics LISA+, University of Tübingen, Auf der Morgenstelle 15, 72076 Tübingen, Germany.

Abstract

We report on the effect of ligand exchange of $\text{Cu}_2\text{Se}_y\text{S}_{1-y}$ as well as Cu_2Se nanocrystals (NCs) with the organic π -system Cobalt β -tetraaminophthalocyanine (CoTAPc) and analyse changes in the structural, optical as well as electric properties of thin films of these hybrid materials. A strong ligand interaction with the surface of the NCs is revealed by UV/vis absorption and Raman spectroscopy. Grazing-incidence small-angle X-ray scattering studies show a significant contraction in the interparticle distance upon ligand exchange. For copper-deficient Cu_{2-x}Se , this contraction has a negligible effect on electric transport, while for copper-deficient $\text{Cu}_{2-x}\text{Se}_y\text{S}_{1-y}$, the conductivity increases by eight orders of magnitude and results in metal-like temperature-dependent transport. We discuss these differences in the light of varying contributions of electronic vs. ionic transport in the two materials and highlight their effect on the stability of the transport properties under ambient conditions. With photocurrent measurements, we demonstrate high optical responsivities of 200-400 A/W for CoTAPc-

capped $\text{Cu}_2\text{Se}_y\text{S}_{1-y}$ and emphasize the beneficial role of the organic π -system in this respect, which acts as an electronic linker and an optical sensitizer at the same time.

Introduction

Copper chalcogenide nanocrystals (NCs) have become a subject of intense research as possible alternatives to the more toxic Cd or Pb-based counterparts for optoelectronic applications such as solar cells or photocatalysts, but also as thermoelectric converters, gas sensors, optical filters, superionic conductors and electro-optical devices.^{29, 34, 47, 108, 146-154} A majority of these investigations focused on the binary compounds copper selenide (Cu_2Se) and copper sulphide (Cu_2S) with variable Cu(I) deficiency (as example Cu_{2-x}Se , $0.00 \leq x \leq 0.6$) and tailored charge carrier concentration as well as charge carrier concentration dependent localized plasmon resonance frequency (LSPR).^{28, 31, 45, 46, 152, 155-159} Introducing Cu(I) vacancies is readily afforded by oxidizing parts of the chalcogenide sublattice into the (-I)-state, which leads to a loss of Cu(I)-ions and the release of free holes in the NC core.³⁶ More recently, the ternary alloy, $\text{Cu}_2\text{Se}_y\text{S}_{1-y}$, has been studied to some extent, for instance as a precursor in the synthesis of $\text{Cu}_2\text{ZnSn}(\text{Se}_y\text{S}_{1-y})_4$ NCs with relevance for photovoltaic applications.^{39, 40, 47-49, 149, 160, 161} Particular, with respect to the oxidation-sensitive Cu_2Se system, it has been argued that $\text{Cu}_2\text{Se}_y\text{S}_{1-y}$ may have similar optoelectronic properties, however with improved stability in air.^{38, 162} For the binary, copper-deficient copper chalcogenide NCs, Cu_{2-x}Se and Cu_{2-x}S , several studies have been conducted to increase electronic coupling in thin films of these materials, for instance by removing the native ligand with smaller molecules or anions, by thermal decomposition of the insulating ligand sphere or by thermal doping.^{2, 34, 42, 43, 147, 157, 158, 163-167} Specifically for Cu_{2-x}Se NCs, several groups have reported that high electric conductivities (up to 25 S cm^{-1}) may also be obtained without such post-synthetic ligand exchange, indicating that charge carrier transport in these NCs potentially follows a different mechanism than that in copper sulphide where ligand exchange is usually necessary.^{3, 8, 168} From the perspective of tailoring the optoelectronic properties of copper chalcogenide NCs by their surface chemistry, such ligand-independent transport characteristics are undesirable. However, the electric conductivities in Cu_2Se NCs are often found to be larger than in comparable Cu_2S NCs.^{42, 118}

The present study is motivated by the hypothesis that alloying Cu_2S into Cu_2Se may combine the ligand-tunable optoelectronic of pure Cu_2S with the high electric conductivity of pure Cu_2Se . To this end, we compare the optical and electrical properties of Cu_2Se and Cu_{2-x}Se with

$\text{Cu}_2\text{Se}_y\text{S}_{1-y}$ and $\text{Cu}_{2-x}\text{Se}_y\text{S}_{1-y}$, assess the different sensitivity to oxidation in air and the effect of ligand exchange with the organic π -system Cobalt β -tetraaminophthalocyanine (CoTAPc). We show that only the ternary alloy exhibits stable electric transport properties in air. Electrical conductivities $> 1 \text{ Scm}^{-1}$ and an increasing resistivity with increasing temperature indicate highly efficient charge carrier transport in CoTAPc-functionalized $\text{Cu}_{2-x}\text{Se}_y\text{S}_{1-y}$ NC thin films. We demonstrate an optical responsivity of 400 A/W under 637 nm photoexcitation which is an exceptionally large photosensitivity for this material. We argue that this is enabled by the hybrid nature of the presented material, in which the organic π -system acts as the photosensitizer and the network of NCs provides the channel for fast transport of the photoexcited charges.

2. Methods

2.1. Synthesis of Cu_2Se nanocrystals:

A synthesis method adapted from Deka et al. has been used to produce quasi-spherical Cu_2Se NCs.³ Standard Schlenk line techniques were applied during synthesis and purification. A mixture of 15 mL 1-Octadecene (ODE) and 15 mL Oleylamine (OLm) is degassed under vacuum -at 115 °C for 3 h. The mixture is cooled to room temperature, and under argon flow 297 mg Copper (I) chloride (CuCl , 3 mmol) is added. For an additional 15 min, the mixture is heated to reflux under vacuum. Subsequently, the flask is filled with argon and the temperature is raised to 300 °C in 5-6 min. The selenium (Se) precursor solution is prepared by dissolving Se (117 mg, 1.5 mmol) in degassed OLm (9 mL) and refluxing under vacuum for 30 min (115 °C). The flask is again filled with argon and the mixture is left stirring at 190-200 °C until all Se is dissolved. Upon dissolution, the temperature is raised to 230 °C for 20 min. To transfer the precursor solution with a glass syringe, the solution is cooled to 150 °C. The Se solution is rapidly injected into the copper precursor solution. The temperature of the reaction mixture is allowed to recover to 290 °C within approximately 2-3 min. The reaction is quenched 15 min after the injection. At 150 °C, toluene (20 mL) is injected to prevent agglomeration. The particles are precipitated from the growth solution with ethanol (20 mL) and methanol (10 mL) and centrifugation (3700g, 20 min). The precipitate is resuspended in toluene (20 mL) by ultrasonication (5 min). After 12 h the solution is centrifuged again (3700g, 20 min) to remove aggregates. The supernatant is collected and used for all further experiments.

2.2. Synthesis of $\text{Cu}_2\text{Se}_y\text{S}_{1-y}$ nanocrystals:

The Se-precursor solution is prepared according to the reported method of Lesnyak et al.¹⁴⁶ 158 mg of Se powder (2 mmol) is mixed with 1 mL of 1-dodecanethiol (DDT) and 1 mL of OLM and is heated for 1 h at 100 °C under nitrogen atmosphere. The resultant, brown alkyl ammonium selenide solution is cooled to room temperature and stored in a nitrogen filled glass vial.

In a three-neck round-bottom flask, 262 mg of Copper(II) acetylacetonate [Cu(acac)₂] (1 mmol) is mixed with 3.5 mL of DDT and 10 mL of OLM and the mixture is degassed under vacuum with vigorous stirring at 70 °C for 1 h. Next, the flask is filled with nitrogen and quickly heated to 220 °C. After complete dissolution, Cu(acac)₂ forms a clear yellow solution. At this temperature, a mixture of 0.5 mL of the Se-precursor with 1.5 mL of DDT is swiftly injected into the flask leading to immediate color change from yellow to brown. The reaction mixture is kept at 220 °C for 30 min. The nanocrystals are precipitated under inert gas atmosphere by centrifugation of the crude reaction mixture with subsequent dissolving of the precipitate in chloroform.

2.3. Thin-Film Preparation and Ligand Exchange:

NC thin films were prepared by assembly at the dimethylsulfoxide/N₂ interface under inert conditions in a glovebox. The fabrication process and ligand exchange were carried out in a home-built Teflon chamber according to our previously reported method.³⁴

2.4. Instrumentation:

Scanning transmission electron microscopy (STEM, Hitachi SU 8030 microscope operating at 30 kV) is employed to determine the particle size and shape. Optical measurements are performed on solid state films on glass substrates using an UV–vis–NIR spectrometer (Agilent Technologies, Cary 5000). Grazing-incidence small-angle X-ray scattering (GISAXS)^{53, 108, 127, 128, 169} is carried out with a laboratory instrument (Xeuss 2.0, Xenocs, France) using Cu K_α radiation ($\lambda = 1.5418 \text{ \AA}$). The samples are probed with a focused X-ray beam of size 0.5 x 0.5 mm² at an incidence angle of 0.22⁰. The GISAXS images are collected with a 2D Pilatus 300K, having 487 x 619 pixels. The detector is placed at a distance of 2496 mm, determined using Ag-behenate as reference sample. X-ray diffraction (XRD) data from the sample is collected in a laboratory source (Cu K_α; GE Inspection Technologies, Germany). Raman spectra are acquired using a Horiba Jobin Yvon Labram HR 800 spectrometer with a CCD-1024 x 256-OPEN-3S9 detector. Excitation for Raman is performed using a He:Ne laser (wavelength 633

nm). Electrical measurements are performed in a glovebox at room temperature with a homemade probe station using a Keithley 2634B dual source-meter unit, controlled by the included test script builder program. The NC films after ligand exchange are deposited on commercially available bottom-gate, bottom-contact transistor substrates (Fraunhofer Institute for Photonic Microsystems, Dresden, Germany) with interdigitated Au electrodes of 10 nm width and 2.5 μm channel length followed by annealing at 250 $^{\circ}\text{C}$ for 2 h under nitrogen atmosphere. The temperature-dependent charge transport properties as well as the photoresponse of the NC thin-films are measured in a Lake-Shore CRX-6.5K probe station at a pressure of 5×10^{-6} mbar, equipped with a Keithley 2636B dual source-meter unit and a Lake Shore temperature controller (model 336). As an excitation source, single mode fiber-pigtailed laser diodes operated by a compact laser diode controller CLD1010 by Thorlabs were used: A 638 nm laser diode with a maximal output power of 70 mW and a 408 nm diode with a maximal output power of 30 mW. Losses to this theoretical optical power output due to scattering, inefficient coupling into the optical fiber, decollimation of the beam etc. were determined by a calibration sample and an optical power meter to obtain the total absorbed optical power at the sample surface.

Results and Discussion

The TEM images in **Figure 3.1a** and **3.1b** depict the morphologies of the as-synthesized alloyed $\text{Cu}_2\text{Se}_y\text{S}_{1-y}$ and Cu_{2-x}Se NCs with relatively uniform size of 7.0 ± 0.8 nm and 12.2 ± 1.9 nm, respectively. All NCs appear well separated by the native OLM capping ligand. Powder X-ray diffraction reveals that the $\text{Cu}_2\text{Se}_y\text{S}_{1-y}$ are in the hexagonal phase (**Figure S3.1**).⁴⁷ We determine the composition of the alloyed NCs by energy-dispersive X-ray spectroscopy (EDX) as $\text{Cu}_{2.2}\text{Se}_{0.68}\text{S}_{0.32}$ (**Figure 3.1c**). We note that colloidal NCs often exhibit an excess of cations on the surface, such that the actual stoichiometry of the inner core may contain less copper than suggested by our EDX result. **Figure 3.1d** shows Raman spectra for solid state films of both NC materials coated with the native OLM ligand. In good agreement with previous reports, the most intense resonance peak is observed at around 260 cm^{-1} for both samples, corresponding to the Se–Se stretch vibration.^{159, 170} For the films composed of the ternary $\text{Cu}_2\text{Se}_y\text{S}_{1-y}$ NCs, two additional peaks are observed, one at 450 cm^{-1} corresponding to the S-S stretching mode, and another peak at 368 cm^{-1} due to the S-Se stretching mode.¹⁷¹ Consistent with the EDX data, the intensity of the Se-Se band is much stronger than that of the S-S and S-Se stretching vibration, suggesting that the alloy is rich in selenium.

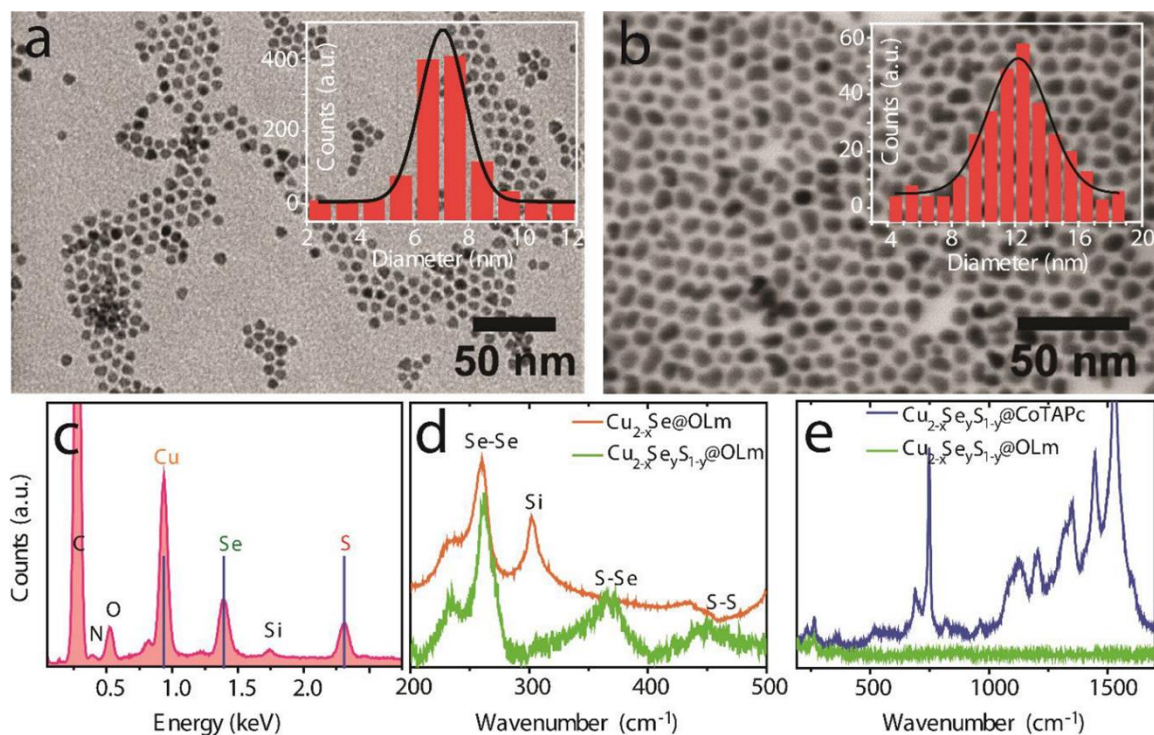


Figure 3.1 TEM images of (a) 7.0 ± 0.8 nm $\text{Cu}_2\text{S}_y\text{Se}_{1-y}$ NCs and (b) 12.2 ± 1.9 nm Cu_2Se NCs. (c) EDX spectrum of the $\text{Cu}_2\text{S}_y\text{Se}_{1-y}$ NCs. (d) Raman spectra of as-prepared Cu_2Se and $\text{Cu}_2\text{Se}_y\text{S}_{1-y}$ nanocrystal thin films (orange curve and green curve, respectively). (e) Raman spectra of Cu_2SeS nanocrystal thin films before and after ligand exchange (green curve and blue curve, respectively).

To enhance chemical and electronic coupling in solid-state films of both NC materials, we exchange the native OLm ligand with the multidendate cross-linker CoTAPc. We choose this linker because earlier reports have shown that tetraaminophthalocyanines are suitable to replace oleylamine from the surface of $\text{Cu}_{1.1}\text{S}$ NCs and drastically improve charge carrier transport.³⁴ The ligand-exchanged NC films exhibit a smooth surface with an average height difference of 3-4 NCs and 1 NC monolayer for $\text{Cu}_2\text{Se}_y\text{S}_{1-y}$ and Cu_2Se , respectively (**Figure S3.2**). We monitor the effect of this ligand exchange by Raman spectroscopy in **3.1e**. (This Figure exemplifies the exchange for $\text{Cu}_2\text{Se}_y\text{S}_{1-y}$ NCs, but the same spectral features between $700 - 1700 \text{ cm}^{-1}$ are also obtained with Cu_2Se after ligand exchange.) In accordance with previous studies, we interpret the strong bands appearing at 747, 1124, 1202, 1337, 1447, 1530 and 1605 cm^{-1} with vibrational modes of CoTAPc, which is supporting evidence for the

presence of the new linker in the NC film.¹⁷² The peaks at 300 and 513 cm^{-1} belong to the Si substrate. Fourier-transform infrared spectroscopy furthermore reveals significant changes after exposure to CoTAPc, most notably the disappearance of characteristic OLM vibrations at 1660 and 3350 cm^{-1} . (For details, see **Figure S3.3** in the Supporting Information.)

We determine the structural details of the ensemble of the two NC samples as well as the effect of ligand exchange with CoTAPc by GISAXS in **Figure 3.2**. The intense in-plane scattering truncation rods, extended along the q_z -direction indicate the formation of superlattices with long-range in-plane order. For OLM-capped Cu_{2-x}Se NCs (**Figure 3.2a+c**), we find the first order in-plane correlation peak at $q_y = 0.043 \text{ \AA}^{-1}$, a second order peak at $q_y = 0.078 \text{ \AA}^{-1}$ and a barely visible third signal at $q_y \approx 0.9 \text{ \AA}^{-1}$. These relative positions in q_y can be interpreted as the formation of a hexagonal lattice ($q_1:q_2:q_3 = 1:\sqrt{3}:2$) with in-plane lattice constant $a = 16.8 \pm 0.1 \text{ nm}$. After ligand exchange with CoTAPc (**Figure 3.2b+c**), the in-plane correlation peaks shift to higher values, that is, smaller lattice constants, and we find $q_y = 0.048 \text{ \AA}^{-1}$, 0.084 \AA^{-1} and a shoulder at 0.096 \AA^{-1} . These values are again in agreement with a hexagonal lattice, but with a contracted in-plane lattice constant $a = 15.1 \pm 0.1 \text{ nm}$. We attribute the contraction of 1.7 nm to the replacement of OLM by the smaller CoTAPc ligand. The improved signal-to-background ratio after ligand exchange indicates a higher degree of long-range order as a result of cross-linking with the rigid organic π -system. With respect to the average particle diameter of $12.2 \pm 1.9 \text{ nm}$ (**Figure 3.1b**), the interparticle spacing before ligand exchange is $4.6 \pm 1.9 \text{ nm}$, which can be interpreted with two adjacent, non-intercalated ligand spheres of OLM. After cross-linking with CoTAPc, the interparticle spacing is reduced to $2.9 \pm 1.9 \text{ nm}$, which is equivalent to 1-2 times the molecular length of CoTAPc. Since the exact binding mode of CoTAPc to the surface of the NCs is not known, the latter finding could either be explained with a side-on binding of stacks of CoTAPc or with head-to-tail cross-linking of a CoTAPc monolayer.

Similar GISAXS patterns are also obtained for $\text{Cu}_{2-x}\text{Se}_y\text{S}_{1-y}$ before and after ligand exchange with CoTAPc (**Figure 3.2d+e**). The first-order correlation peak shifts from 0.074 \AA^{-1} with OLM functionalization to 0.082 \AA^{-1} after ligand exchange (**Figure 3.2f**). Under the assumption of a hexagonal lattice, this corresponds to a center-to-center distance between the NCs of $9.8 \pm 0.1 \text{ nm}$ for OLM functionalization and $8.8 \pm 0.1 \text{ nm}$ for CoTAPc as the ligand. With a particle diameter of $7.0 \pm 0.8 \text{ nm}$, the interparticle distances are $2.8 \pm 0.8 \text{ nm}$ for OLM and $1.8 \pm 0.8 \text{ nm}$ for CoTAPc. The latter result may be viewed as indirect supporting evidence that CoTAPc binds preferentially in a head-to-tail cross-linking manner between the surfaces of

two adjacent NCs as the width of the ligand sphere is precisely one molecular length of CoTAPc.

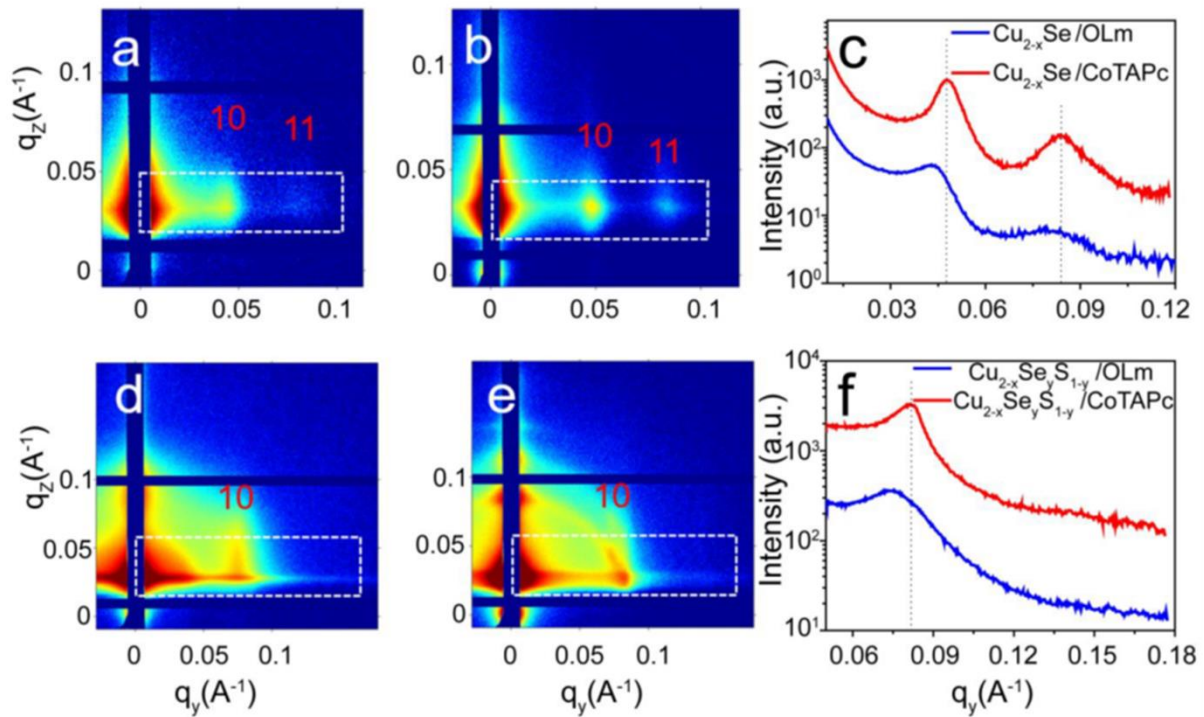


Figure 3.2 GISAXS patterns of self-assembled (a) $\text{Cu}_{2-x}\text{Se}/\text{OLm}$, (b) $\text{Cu}_{2-x}\text{Se}/\text{CoTAPc}$, (d) $\text{Cu}_{2-x}\text{Se}_y\text{S}_{1-y}/\text{OLm}$ and (e) $\text{Cu}_{2-x}\text{Se}_y\text{S}_{1-y}/\text{CoTAPc}$ films. (c) and (f) extracted line profiles from the corresponding GISAXS images on the left in (a)/(b) and (d)/(e), respectively, as a function of the in-plane scattering vector q_y . To improve the statistics of the line profiles, the ROI (white dotted box) was integrated along the q_z direction.

For charge transport studies, we deposit both copper chalcogenide NC films on silicon oxide substrates with pre-patterned Au contacts and record the two-point probe current–voltage (I – V) characteristics at room temperature. In **Figure 3.3a+b**, we focus on a comparison of the I/V characteristics of both materials before and after ligand exchange with CoTAPc and before/after oxidation by exposure to air. The left panels in **Figure 3.3** represent the characteristics of the ternary copper chalcogenide NCs, while the right panel characterizes the binary NCs. The color code is the same for both materials: green = OLM capping, reduced; yellow = OLM capping, oxidized; blue = CoTAPc capping, reduced; red = CoTAPc capping, oxidized. Oxidation leads to copper vacancies and a non-stoichiometric composition in copper selenide NCs and drastically increases the density of free holes, which manifests in degenerate p-type doping as well as the occurrence of an LSPR in the near-infrared (NIR).^{45, 46, 151}

Therefore, we monitor the degree of vacancy doping for both samples with vis/NIR absorption spectroscopy in **Figure 3.3c+d**. We note a broad band centred at 1250 nm for oxidized $\text{Cu}_{2-x}\text{Se}_y\text{S}_{1-y}$ (for both OLM and CoTAPc ligands), 1300 nm for oxidized OLM-capped Cu_{2-x}Se and 1600 nm for oxidized Cu_{2-x}Se capped with CoTAPc, which we interpret as LSP resonances. In the reduced state, both materials show a negligible LSPR signal below 2000 nm, indicative of a low carrier density and a near stoichiometric copper content. In both ligand exchanged samples, the HOMO-LUMO transition of CoTAPc invokes a strong absorption band between 600-800 nm. (See Supporting Information for the absorption spectrum of pure CoTAPc. **Figure S3.2**) Before ligand exchange, charge transport is poor in both materials (green curve) with conductivities on the order of $10^{-8} \text{ S cm}^{-1}$ for $\text{Cu}_2\text{Se}_y\text{S}_{1-y}$ and $10^{-4} \text{ S cm}^{-1}$ for Cu_2Se . After surface functionalization with CoTAPc, both materials behave similar and the conductivities increase dramatically to 1 S cm^{-1} and 5 S cm^{-1} , respectively (blue curve). In contrast, when studying the effect of oxidation in air for several hours (Cu_{2-x}Se) or days ($\text{Cu}_{2-x}\text{Se}_y\text{S}_{1-y}$), we observe a different behavior for $\text{Cu}_{2-x}\text{Se}_y\text{S}_{1-y}$ vs. Cu_{2-x}Se . While the increase of copper vacancies has a negligible effect on the transport properties of OLM-capped $\text{Cu}_{2-x}\text{Se}_y\text{S}_{1-y}$, it increases the conductivity of the OLM-capped Cu_{2-x}Se to 6 S cm^{-1} . Oxidizing the CoTAPc-capped NC films has no significant effect on the conductivity of either of the two samples (**Figure S3.3**).

The structural characterization in **Figure 3.2** demonstrates that the highly conductive OLM-capped Cu_{2-x}Se NCs are well-separated from each other ($4.6 \pm 1.9 \text{ nm}$), such that necking and the formation of percolative pathways are an unlikely explanation for such efficient charge carrier transport. Similar widths of the OLM ligand sphere are also observed for $\text{Cu}_{2-x}\text{Se}_y\text{S}_{1-y}$ ($2.8 \pm 0.8 \text{ nm}$, this work) and $\text{Cu}_{1.1}\text{S}$ NCs ($4.1 \pm 1.7 \text{ nm}$), which exhibit negligible conductivities ($10^{-8} \text{ S cm}^{-1}$ and $10^{-9} \text{ S cm}^{-1}$, respectively).³⁴ We note that previous reports on drop-casted, oxidized OLM-capped Cu_{2-x}Se NCs revealed similar or even larger conductivities, corroborating our finding here that Cu_{2-x}Se NCs show uniquely different transport properties compared to $\text{Cu}_{2-x}\text{Se}_y\text{S}_{1-y}$ or $\text{Cu}_{1.1}\text{S}$ NCs.^{3, 8, 168} It is furthermore surprising that the significant contraction of the Cu_{2-x}Se NC ensemble by 1.7 nm upon ligand exchange has no effect on the conductivity (**Figure 3.3b** yellow vs. red curve). This speaks against electronic (hopping) conduction as the dominant transport mechanism in OLM-capped Cu_{2-x}Se NC thin films, which is strongly affected by a change of the hopping distance.¹⁷³ We hypothesize that ionic conduction of mobile copper ions may play a key role here. Very large ionic mobilities with diffusion constants $> 10^{-5} \text{ cm}^2\text{s}^{-1}$ and superionicity have been reported for Cu_{2-x}Se , which can result in electric conductivities $> 1 \text{ S cm}^{-1}$.^{151, 174} Although it is not immediately obvious how

such ionic conductivity would be affected by the OLM ligand sphere, superionicity is an important feature of Cu_{2-x}Se NCs and likely to be responsible for the unusually large electric conductivities. This would explain why only a reduction in copper vacancies can significantly reduce the conductivity in OLM-capped Cu_2Se NCs. After surface-functionalization with CoTAPc, electronic conduction appears greatly improved, such that the conductivity is now only weakly affected by the density of copper vacancies (**Figure 3.3b** blue vs. red curve).

An alternative explanation which we briefly consider here involves the formation of conductive, percolative pathways consisting of copper oxide nanostructures. Oxidation in air of Cu_2Se NCs results in the release of Cu(I)-ions, which react with oxygen to copper oxide NCs.⁴⁵ The conductivity of some copper oxide phases (which are mostly semiconducting) is rather high, and it is possible that successive release of Cu(I) ions from the Cu_2Se NCs leads to a continuous network of this conductor. Once formed, charge transport across this network is expected to be unaffected by the addition of $[\text{Cu}(\text{CH}_3\text{CN})_4]\text{PF}_6$, which is a powerful reducing agent for Cu_{2-x}Se NCs (via filling of Cu(I) vacancies), but not for copper oxide. However, we find that films of $\text{Cu}_{2-x}\text{Se}/\text{OLM}$ NCs show a drastically reduced electric conductivity upon treatment with $[\text{Cu}(\text{CH}_3\text{CN})_4]\text{PF}_6$, which speaks against this alternative explanation (see **Figure S3.4**).

The transport characteristics of the ternary $\text{Cu}_2\text{Se}_y\text{S}_{1-y}$ NC ensemble appears to be dominated by electronic conduction with a strong dependence on the hopping distance (**Figure 3.3a** yellow vs. red curve and green vs. blue curve) and weak dependence on the density of copper vacancies (**Figure 3.3a** green vs. yellow curve and blue vs. red curve). In view of a recent report on electric transport in similar $\text{Cu}_{1.1}\text{S}$ NC ensembles, the $\text{Cu}_2\text{Se}_y\text{S}_{1-y}$ NCs investigated here resemble much more that of the binary sulphides than the selenides.³⁴

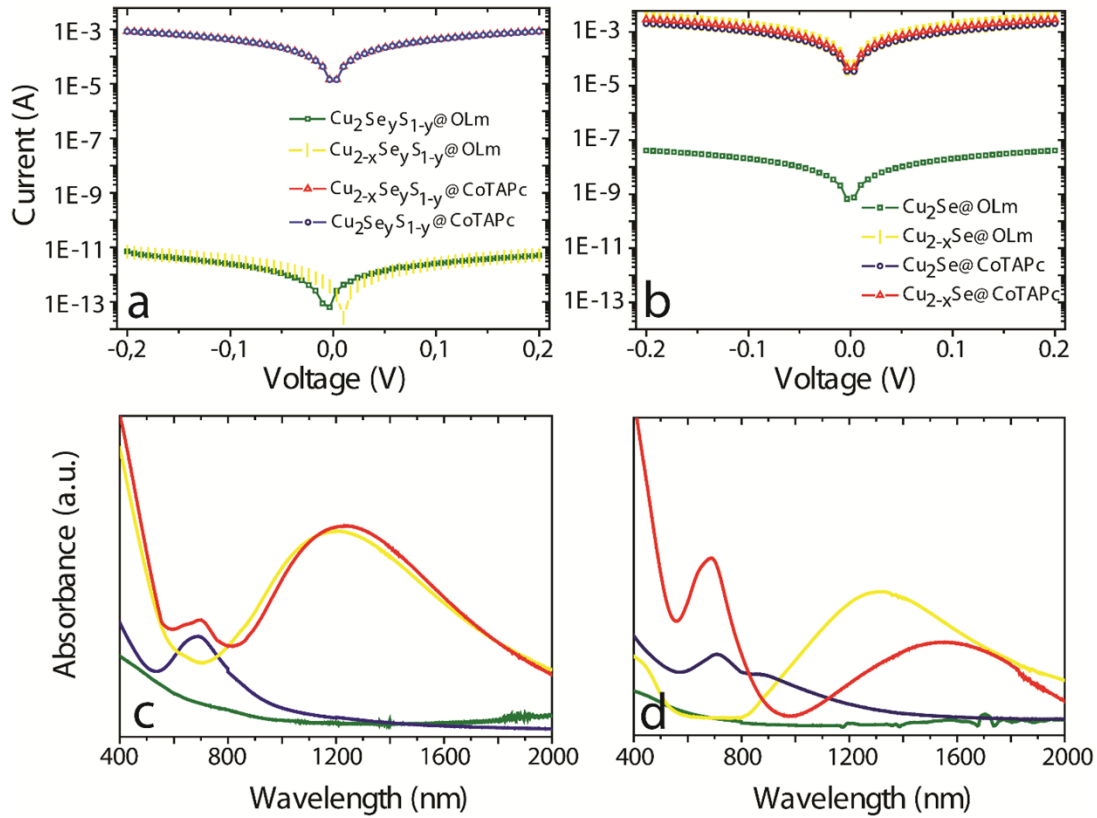


Figure 3.3(a) Current-voltage (*I-V*) curves of $\text{Cu}_2\text{Se}_y\text{S}_{1-y}$ as well as $\text{Cu}_{2-x}\text{Se}_y\text{S}_{1-y}$ and (b) of Cu_2Se and Cu_{2-x}Se . (c) Corresponding optical absorption spectra of the ternary and (d) binary copper chalcogenides. The color code is the same in all four panels: green = OLM capping, reduced; yellow = OLM capping, oxidized; blue = CoTAPc capping, reduced; red = CoTAPc capping, oxidized.

To further understand the electronic properties of CoTAPc-capped $\text{Cu}_2\text{Se}_y\text{S}_{1-y}$ NCs, we perform temperature-dependent resistivity measurements under high vacuum (**Figure 3.4a**). Throughout the entire temperature regime of 20-300 K, we observe monotonically increasing resistance with temperature, reminiscent of metallic behavior. Such characteristic is rarely observed in copper chalcogenide NC ensembles, and only in cases where electronic coupling is large enough to overcome the temperature-activated hopping regime.^{43, 175}

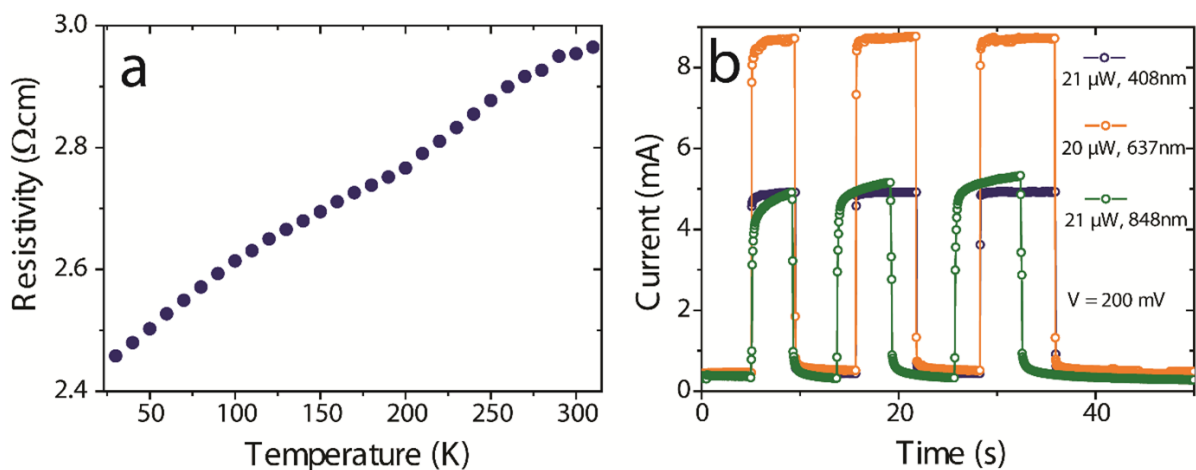


Figure 3.4(a) Temperature-dependent resistivity of $\text{Cu}_2\text{Se}_y\text{S}_{1-y}$ functionalized with CoTAPc. **(b)** Time-dependent current at 200 mV of a $\text{Cu}_2\text{Se}_y\text{S}_{1-y}$ /CoTAPc film during three excitation periods to 21 μW of 408 nm light (blue), 20 μW of 637 nm light (orange) and 21 μW of 848 nm (green).

In light of the tunable optical absorption properties, copper chalcogenide NCs are often considered for applications where light-to-electric current conversion is important, such as photovoltaics or photocatalysis. However, the photocurrent behaviour of these materials showed only moderate photosensitivities so far.^{30, 41, 78, 176} In **Figure 3.4b**, we display the ON/OFF photocurrent characteristics of $\text{Cu}_2\text{Se}_y\text{S}_{1-y}$ /CoTAPc NCs during three excitation periods with 408 nm, 637 nm and 848 nm laser diodes at roughly the same direct optical power of $\sim 20 \mu\text{W}$. At a bias of 200 mV, we find a photocurrent of ~ 4 mA and ~ 8 mA, respectively, corresponding to a responsivity of 200 A/W at 408 nm and 400 A/W at 637 nm. The reversibility of the transport characteristics after each excitation period indicates that the increased current is indeed a photocurrent and not, as recently observed for copper sulphide NCs, an irreversible photo-doping effect.¹⁶⁵ We explain such unprecedented optical responsivity with the presence of CoTAPc, which shows strong absorbance at all three excitation wavelengths (See Supporting Information). We suggest that CoTAPc sensitizes $\text{Cu}_2\text{Se}_y\text{S}_{1-y}$ NCs for the absorption of photons at these wavelengths to form singlet excitons in the organic pi-system, which are split at the organic-inorganic interface and quickly swept to the source-drain electrodes under a small bias. For comparison, we have also measured the 408 nm photocurrent response for OLM-capped $\text{Cu}_2\text{Se}_y\text{S}_{1-y}$ NCs, that is, without any CoTAPc sensitizers (see Supporting Information **Figure S3.5**). Here, the responsivity is only on the order of 3 $\mu\text{A/W}$. We conclude that the dramatic increase in responsivity by almost 8 orders of

magnitude observed after functionalizing $\text{Cu}_2\text{Se}_y\text{S}_{1-y}$ NCs with CoTAPc is due to the combined effect of better electronic coupling and the additional absorption of the organic pi-system. Thus, CoTAPc acts as an electronic cross-linker and optical sensitizer for the NCs.

Conclusion

We have measured the structural, optical and electric properties of ternary $\text{Cu}_2\text{Se}_y\text{S}_{1-y}$ NC solids capped with oleylamine and the organic pi-system Cobalt β -Tetraaminophthalocyanine (CoTAPc), respectively, and compared it to the binary compound Cu_2Se . While the structural and optical response to ligand exchange and oxidation in air is rather similar for both materials, we have observed substantial differences in the charge carrier transport properties. Charge transport in $\text{Cu}_2\text{Se}_y\text{S}_{1-y}$ NC solids is dominated by electronic conduction, very sensitive to structural changes and largely unaffected by oxidation in air. Exchanging the surface ligand oleylamine with the organic π -system not only drastically increases electronic coupling in the $\text{Cu}_2\text{Se}_y\text{S}_{1-y}$ NC ensembles but also invokes an increase in the optical responsivity by eight orders of magnitude. Thus, ligand exchange with CoTAPc enables high conductivity and large responsivity in $\text{Cu}_2\text{Se}_y\text{S}_{1-y}$ NC films, which are much more robust against oxidation than their binary Cu_2Se analogues.

Acknowledgements

The authors acknowledge the DFG for support under Grants SCHE1905/3, SCHE1905/4, DO1580/5 and SCHR700/25. We also thank Mrs. Elke Nadler, Institute of Physical and Theoretical Chemistry, University of Tübingen, for performing SEM/STEM measurements using a Hitachi SU 8030 SEM which was funded by the DFG under contract INST 37/829-1 FUGG, partially.

Corresponding Author:

*email: marcus.scheele@uni-tuebingen.de

Author Contributions:

The manuscript was written through contributions of all authors. All authors have given approval to the final version of the manuscript.

Supplementary Material:

(S1) XRD pattern of as-synthesized $\text{Cu}_2\text{S}_y\text{Se}_{1-y}$ NCs, (S2) AFM images and height profiles of NC films, (S3) FT-IR spectra of Cu_2Se and $\text{Cu}_2\text{Se}_y\text{S}_{1-y}$ NC films before and after ligand

exchange with CoTAPc, (S4) UV/VIS absorption spectrum of pure CoTAPc, (S5) I/V curves of CoTAPc-functionalized $\text{Cu}_{2-x}\text{S}_y\text{Se}_{1-y}$ NCs after varying exposure times to air, and (S6) Current–voltage characteristics of a Cu₂Se/OLm film after different oxidation/reduction treatments, and (S7) I/V curves of OLm functionalized $\text{Cu}_{2-x}\text{Se}_y\text{S}_{1-y}$ NCs under photoexcitation by a 408 nm laser diode of varying optical power.

4. Publication 3

***In Situ* Formation of Electronically Coupled Superlattices of Cu_{1.1}S Nanodiscs at the Liquid/Air Interface**

*Sonam Maiti^{1,2}, Santanu Maiti*¹, Andre Maier², Rupak Banerjee³, Shen Chen⁴, Bridget M. Murphy^{5,6}, Marcus Scheele^{2,7}, Frank Schreiber*^{1,7}*

¹Institute of Applied Physics, University of Tübingen, Auf der Morgenstelle 10, 72076 Tübingen, Germany.

²Institute of Physical and Theoretical Chemistry, University of Tübingen, Auf der Morgenstelle 18, 72076 Tübingen, Germany.

³Department of Physics, Indian Institute of Technology Gandhinagar, Palaj, Gandhinagar 382355, India.

⁴Deutsches Elektronen-Synchrotron DESY, Notkestraße 85, D-22607 Hamburg, Germany

⁵Institute for Experimental and Applied Physics, Kiel University, D-24098 Kiel, Germany

⁶Ruprect Heansel Laboratory, Kiel University, D-24098 Kiel, Germany

⁷Center for Light-Matter Interaction, Sensors & Analytics LISA+, University of Tübingen, Auf der Morgenstelle 15, 72076 Tübingen, Germany

Abstract

We report on the in-situ monitoring of the formation of conductive superlattices of Cu_{1.1}S nanodiscs via cross-linking with semiconducting cobalt 4,4',4'',4''',4''''-tetraaminophthalocyanine (CoTAPc) molecules at the liquid/air interface by real-time grazing incidence small angle X-ray scattering (GISAXS). We determine the structure, symmetry and lattice parameters of the superlattices, formed during solvent evaporation and ligand exchange on the self-assembled nanodiscs. Cu_{1.1}S nanodiscs self-assemble into two-dimensional hexagonal superlattice with a minor in-plane contraction (~ 0.2 nm) in the lattice parameter. A continuous contraction of the superlattice has been observed during ligand exchange, preserving the initial hexagonal symmetry. We estimate a resultant decrement of about 5% in

the in-plane lattice parameters. The contraction is attributed to the continuous replacement of the native oleylamine surface ligands with rigid CoTAPc. The successful cross-linking of the nanodiscs is manifested in terms of the high electrical conductivity observed in the superlattices. This finding provides a convenient platform to understand the correlation between the structure and transport of the coupled superstructures of organic and inorganic nanocrystals of anisotropic shape.

KEYWORDS: nanocrystals, self-assembly, GISAXS, superlattice, liquid/air interface

Self-assembly of nanocrystals (NCs) into ordered structures has garnered increased attention due to their astonishing properties which are valuable for fundamental studies and technological devices.^{53, 54, 108, 109, 177-184} Most of the as-prepared NCs are usually spherical in shape and produce essentially non-conductive superlattice as they feature insulating surface ligands. Relatively little research has been carried out to improve the physical properties of the superlattices by tuning the shape of the NCs, passivating the surface of the NCs and cross-linking with organic semiconductor molecules (OSC).^{52, 185-187} Superstructure of copper sulfide nanomaterials have demonstrated generous use for their rich transport and plasmonic properties.^{2, 36, 43, 106, 115} The controlled preparation of two dimensional ordered and conductive assemblies of NCs with anisotropic shape is one of the challenges in nano-fabrication as the overall properties of the assemblies depend on their shape and orientation.¹⁸⁸⁻¹⁹⁰ Recently, the physical properties of nanoparticle superstructures coupled electronically with OSC molecules has been investigated by *ex-situ* measurements.^{34, 55} In such a typical superlattice, the OSC molecules bind at certain facets of the NCs with their reactive groups as they have a strong preference to couple between NCs. This might promote high charge carrier transport across the superstructure through resonant energy levels. In spite of the growing importance in the field of fabrication of conductive superstructures by tuning the shape of the NCs, the exact formation mechanism revealing the process is still poorly understood. Here, we use this approach to fabricate the superlattice with interesting transport properties by a) tuning the shape of the NCs, b) passivating the NCs surface, and c) cross-linking with organic semiconducting (OSC) molecules and followed the structure formation in real time.

We choose *in-situ* grazing incidence small angle x-ray scattering (GISAXS)^{108, 128, 169}, which is particularly relevant in elucidating the structure formation in real-time during the involved chemical processes, starting from the self-assembly to ligand exchange. In this context,

GISAXS is crucial to determine the *in-situ* structural changes in the thin film at the liquid/air interface. We report the *in-situ* formation of conductive hexagonal superlattices of Cu_{1.1}S nanodiscs (NDs) by exchanging the native oleylamine (Olm) surface ligand with CoTAPc at the dimethyl sulfoxide (DMSO)/air interface. Initially, the nanodiscs (core diameter 12.7 ± 0.5 nm and thickness 5.8 ± 0.2 nm) self-assemble into a two dimensional (2D) hexagonal superlattice after spreading them on the liquid surface with almost unaltered lattice parameter. A continuous contraction of the in-plane lattice parameters occurs during ligand exchange preserving the 2D hexagonal structure on liquid surface. The replacement of Olm with CoTAPc ligands in these superlattice films is confirmed by ex-situ Raman spectroscopy. A dramatic increase in the conductivity by more than 6 orders of magnitude of the ligand exchanged films suggests that the phthalocyanine derivative acts as an electronic linker between the NDs.

Self-assembly of oleylamine-capped nanodiscs at the DMSO/air interface:

Self-assembly of Olm-capped Cu_{1.1}S NDs (**Figure S4.1a**) has been monitored by dispersing 5 μ M, 200 μ L NC solution in toluene at the DMSO/air interface in a custom-built Teflon cell of surface area 3x4 cm². *In-situ* GISAXS patterns are collected as a function of waiting time at an interval of 4-6 minutes during the self-assembly process. **Figure 4.1a** and **4.1b** show the GISAXS patterns for 5 minutes and 240 minutes of waiting period whereas others at intermediate times are shown in the Supporting Information (**Figure S4.2**). The appearance of several scattering peaks along the in-plane direction (q_y) corresponds to the formation of order superlattices. The in-plane peak positions has a ratio of 1: $\sqrt{3}$:2 - which is the characteristic for a 2D hexagonal superlattice and are indexed to the (10), (11) and (20) lattice planes. During the self-assembly process, all the GISAXS patterns show resemblance among themselves which illustrates that the superlattices remain in a hexagonal geometry for the whole period of assembling time. The scattering peaks in the GISAXS patterns are fitted by the distorted wave Born Approximation (DWBA)^{127, 169, 191, 192} method considering a model of 2D hexagonal superlattice with suitable lattice parameters ($a, b, c = \text{Inf.}, \alpha=\beta=90^\circ, \gamma=120^\circ, \theta_c=0.1^\circ$) and *P6mm* space group (S.G.) symmetry oriented with [001]_{SL}-axis perpendicular to the liquid substrate. We found a small contraction in lattice parameter (~ 0.2 nm) during the first 10 minutes first of self-assembly and an almost unaltered of $a=b= 16.8 \pm 0.1$ nm for rest of the self-assembly period (60 minutes) as shown in **Figure 4.1c**. The obtained lattice parameters also imply that the nanodiscs (NDs) assemble into 2D hexagonal superlattice with an edge-to-edge configuration. **Figure 4.1d** shows that the in-plane scattering peaks have no shift in the

extracted line profiles of the GISAXS patterns, obtained at different time intervals, except first two points (5 and 30 minutes).

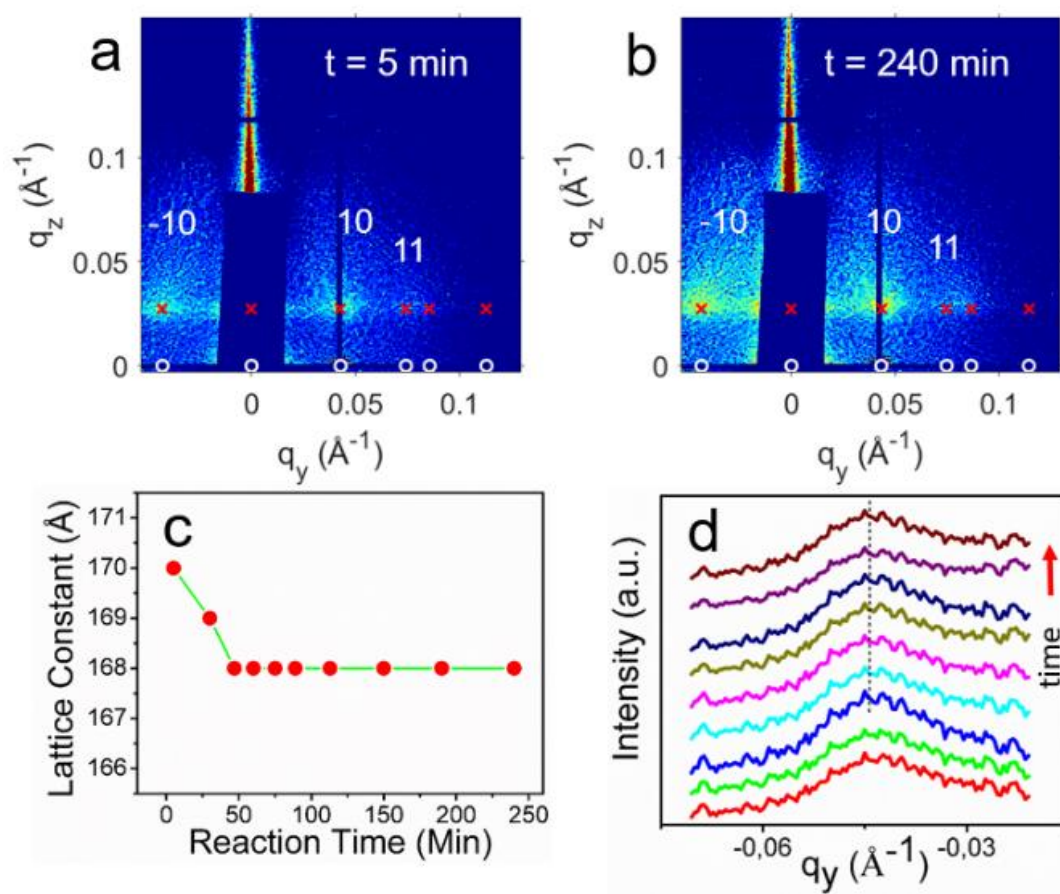


Figure 4.1a) GISAXS patterns of the NDs during self-assembly for a waiting period of **a)** 5 min. and **b)** 240 min. The white circles (transmitted) and red crosses (reflected) are the simulated diffraction patterns considering a hexagonal superlattice along the in-plane direction. **c)** Temporal evolution of the lattice constants. **d)** In-plane line profiles along $-q_y$ through the {10} peak of the GISAXS patterns.

Self-assembly of the nanodiscs during ligand exchange at the DMSO/air interface:

To gain insight into the ligand exchange process of the self-assembled $\text{Cu}_{1.1}\text{S}$ NDs (already in a 2D hexagonal superlattice) at the DMSO/air interface, we inject CoTAPc ligand solution in the bulk DMSO and investigate the structural change as a function of reaction time by *in-situ* GISAXS measurements. We recorded a series of GISAXS patterns in a regular time interval of 4-6 minutes during ligand exchange and **Figure 4.2a-d** represents four selected GISAXS patterns, collected at -42, 6, 24 and 276 minutes, respectively. It should be noted that in the present case, the reference time ($t = 0$) is the time of ligand injection in the bulk liquid subphase.

During ligand exchange, the scattering pattern of all the GISAXS images including the images in the intermediate time periods (**Figure S4.3**) reveal a high resemblance with the patterns collected during self-assembly (**Figure 4.1, 4.2a**). This clearly indicates that the CoTAPc ligands do not significantly change the symmetry of the superlattice during ligand exchange at the liquid/air interface. To determine the transformation of the lattice parameter as a function of reaction time, we again extract the in-plane lattice parameters by simulating and fitting the scattering patterns of each images taking into account DWBA. Additionally, we determine the lattice parameter at different time period, from the peak position of the corresponding GISAXS line profiles (**Figure 4.2e**) passing through the first correlation peak (-10) along q_y -direction.

The patterns correspond to 2D hexagonal superlattice with $P6mm$ SG symmetry and oriented with $[001]_{SL}$ -axis perpendicular to the liquid surface with varied lattice parameters (**Table 2**). The temporal evolution of the in-plane superlattice parameters (δ) after ligand injection is presented in **Figure 4.2f**. It illustrates that the lattice parameter shrinks almost linearly from 16.75 ± 0.1 to 16 ± 0.1 nm during the time period of 60 min. (refer **Figure 4.2f**) with a rate of $0.18 \text{ \AA}/\text{min}$. For the rest of the waiting period (276 minutes), we have not observe any further major contraction of the superlattice. It is important to note that the hexagonal symmetry of the NDs superlattice was conserved during the superlattice contraction *via* ligand exchange with CoTAPc.

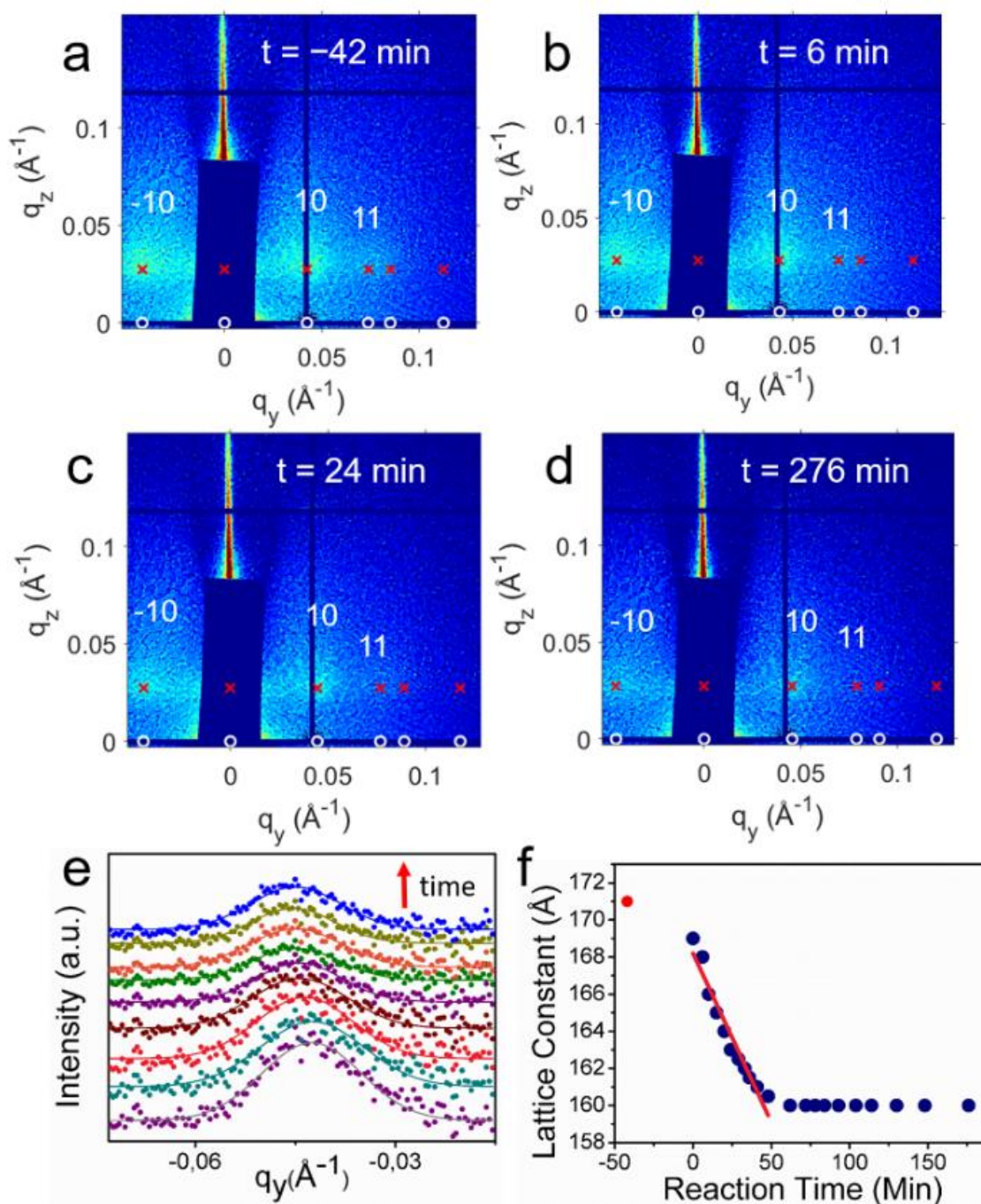


Figure 4.2 GISAXS patterns of the NDs during ligand exchange for a waiting period of **a)** -42 min, **b)** 6 min, **c)** 24 min, and **d)** 276 min. The red crosses and white circles are the simulated diffraction patterns considering a hexagonal superlattice along the in-plane direction. **e)** In-plane line profiles along $-q_y$ through the $\{10\}$ peak of the GISAXS patterns. Peak intensities have been scaled up for clarity. **f)** Temporal evolution of the lattice constants with elapsed time.

Ex-situ measurements of the ligand exchanged films:

The Raman vibrational spectrum of the native and ligand exchanged superlattices are shown in **Figure 4.3a**. The NDs capped with oleylamine ligand shows a sharp peak at 471 cm^{-1} , which can be attributed to the S-S stretching vibration in crystalline CuS nanoparticles (NPs).¹²⁵ Several new peaks appeared at $747, 1105, 1336, 1447, 1533$ and 1607 cm^{-1} are due to presence of CoTAPc in the sample through ligand exchange (red curve **Figure 4.3a**).¹⁹³ These Raman spectra of both are in good agreement with the existing literature on crystalline copper sulfide and CoTAPc.^{34, 125, 193} **Figure 4.3b** shows the obtained current-voltage (I-V) characteristics in semi-log scale from the corresponding samples. We observe an ohmic behavior of the current with increasing bias voltage. The conductivity of the cross-linked superlattice is higher by about 6 orders of magnitude with respect to the native Olm capped film.

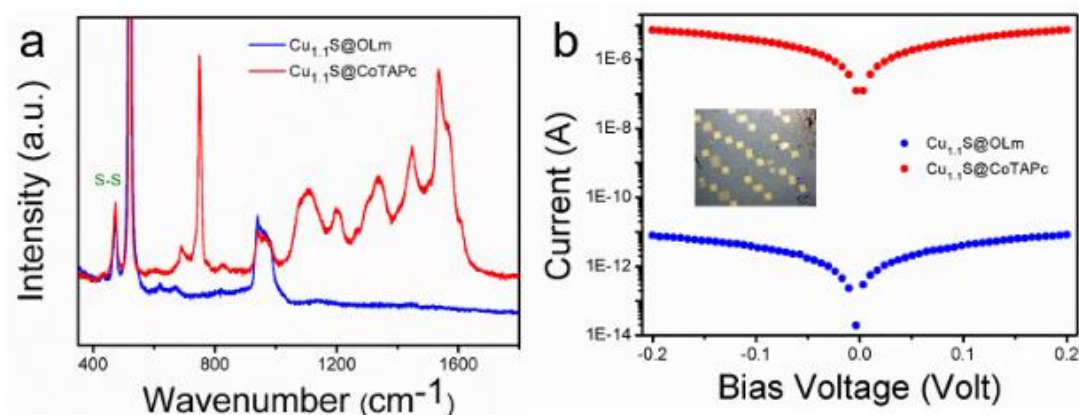


Figure 4.3a) Raman spectra of Cu_{1.1}S nanodisc thin films before (blue) and after ligand exchange (red). **b)** Current-voltage (I-V) characteristics of Cu_{1.1}S ND films. Blue circles: Olm-capped Cu_{1.1}S ND films and red circles: Cu_{1.1}S ND film after ligand exchange. The graph is plotted on a logarithmic scale for better comparison. Inset: photograph of a substrate with Au contacts for I-V measurements.

We determined the structure of the colloidal nanocrystal solution undergoing self-assembly *via* slow solvent evaporation and the superlattice experiencing ligand exchange by CoTAPc ligands as a function of reaction time (276 minutes) and compared our results with few earlier works on the self-assembly of anisotropic nanoparticles. Recently, Maiti *et al.* observed the *in-situ* formation of disc shape single crystalline CuS nano-objects and their self-assembly at the liquid-liquid interfaces.¹¹ Korgel group reported the self-assembly of disc shape CuS

nanoparticles by using time resolved SAXS and GISAXS, showing the formation of isotropic-to-columnar arrays during solvent evaporation.¹⁹⁴ Li *et al.* also observed the columnar self-assembly of Cu₂S hexagonal nanoplates in which Sn-X complexes act as the native inorganic surface ligands.⁷¹ In contrast to the previous works on the disc shape nanocrystals, we have not found any strong scattering peaks along the out-of-plane (q_z) direction which undoubtedly rule out the possibility of the formation of columnar assembly by the Cu_{1.1}S NDs. We have not seen similar events even after adding external crosslinking molecules. In our study, we find a very small (~ 0.2 nm) contraction of the nanocrystal superlattice parameter during self-assembly *via* solvent evaporation which is in contrary to the solvent evaporation induced assembly of concentrated solution of spherical PbS NPs (diameter 6.8 nm) at the acetonitrile/air interface.⁵³ The self-assembly of NCs are attributed to the capillary forces present in the liquid surfaces.⁵³ On the other hand, this small contraction is consistent with the recent results on cubic PbS NCs (edge length 11.8 nm).⁵⁴ They proposed that the effective capillary forces are not sufficient enough to displace the relatively large size particles.^{53, 195, 196} We believe that in the present case, the small contraction during solvent evaporation is also due to the ineffective capillary forces acting on the large diameter (12.7 nm) disc-shape particle at air/liquid interface. In our previous *ex-situ* study (prepared in inert atmosphere/glove box), we observed that similar NDs organise into hexagonal superlattice for self-assembled (without ligand exchange) and ligand exchanged films with Cu-4,4',4'',4''',4''''-tetraaminophthalocyanine (CuTAPc) with similar lattice parameters.³⁴ In contrary, here we monitored the in-situ self-assembly and ligand exchange of similar nanodiscs with CoTAPc as adligands directly at the air/liquid interface using synchrotron X-ray scattering to know the formation kinetics of the structural organization. For an understanding of possible electronic consequences of the structural changes in Cu_{1.1}S ND superlattices, it is elucidating to correlate the structural, optical and transport behaviour after ligand exchange. While Raman spectra (**Figure 4.3a**), in particularly the new vibrational peaks above 1000 cm⁻¹, show that the strongly-insulating Olm ligands are replaced by CoTAPc,³⁴ this removal enhances the current by six orders of magnitude (refer **Figure 4.3b**). The significant enhancement in conductivity depicts the efficient charge transport in the coupled superstructures by decreasing the inter-particle separation and increasing electronic coupling among the NDs via semiconducting ligands.

In summary, we have monitored the real time structural evolution of Cu_{1.1}S nanodisc superlattices at the DMSO/air interface during self-assembly followed by ligand exchange with CoTAPc molecules. The nanodiscs self-assemble into 2D hexagonal superlattices and their

lattice parameters does not change significantly during self-assembly. In contrast, the in-plane lattice parameters of the superlattice contracts isotropically during ligand exchange by preserving initial structural symmetry with a resultant shrinkage of about 5%. We attribute this contraction to the continuous replacement of oleylamine surface ligands by small CoTAPc molecules. Finally, we demonstrate that the OSC molecules act as electronic coupling agents between the nanodiscs to promote high charge carrier transport across the order superlattices.

This work was supported by the DFG under grants SCHR700/25. We thank the DESY, Hamburg, Germany, for enabling X-ray scattering experiments at P08, Petra-III. We acknowledge the fruitful discussion with F. Bertram, R. Giri and B. Reisz. BMM thank BMBF for grants 05KS7FK3/05KS10FK2 (LISA spectrometer) and 05K16FK1 (Lambda detector). We thank Mrs. Nadler for STEM measurements.

Conflicts of interest

There are no conflicts to declare.

Corresponding Author:

santanu.maiti@uni-tuebingen.de

Supporting Information

Experimental details. TEM image of Olm-passivated $\text{Cu}_{1.1}\text{S}$ NDs, Structural formula of CoTAPc, GISAXS patterns from the self-assembly without ligand exchange at different intermediate times, GISAXS patterns from the self-assembly during ligand exchange process at different intermediate times, STEM image of $\text{Cu}_{1.1}\text{S}$ NC superlattice, AFM image of the nanocrystal superlattice after complete ligand-exchange and drying on a silicon substrate and table of Superlattice parameters.

Conclusions

In this thesis work, we demonstrated an approach to increase the conductive properties of NCs films by crosslinking the particles with multivalent organic semiconductor molecules. Ideally, the film not only gets mechanically more stable through chemically connecting the NCs, but also shows increased electronic conductance. We have carried out spectroscopy studies to explore the direct evidence of ligand attachment with NCs surface. The structural changes before and after ligand exchange has been confirmed by the Grazing incidence x-ray scattering (GISAXS) techniques. Also GISAXS and the microscopy studies confirm the superlattice of the ligand exchanges films formed at liquid-air interfaces. We observed that the direct coupling by means of increased electrical conductivity by several order of magnitude by two-point probe electrical measurements. The charge carrier conduction mechanism is revealed by temperature-dependent electrical transport measurements of the NCs superlattices films.

We have demonstrated ligand exchange of $\text{Cu}_{1.1}\text{S}$ nanocrystals with organic semiconductor Cu4APc molecule yields a quasi-2D thin film with significant long-range order and electronically coupled network. UV-vis-NIR and Raman spectroscopy results exhibit the presence/binding of the organic semiconductor ligand between/to the $\text{Cu}_{1.1}\text{S}$ nanocrystals. The GISAXS measurements confirms the contraction of the interparticle spacing is to a net decrease of 11 Å. It is noteworthy that even after this contraction, the average interparticle spacing is 30 ± 17 Å and, thus, the NCs remain spatially well separated. 2-point probe conductivity measurements reveal a dramatic increase in conductivity by more than six orders of magnitude after ligand exchange, suggesting that the phthalocyanine derivative acts as an electronic linker. Temperature-dependent electrical transport measurements indicated that at low temperatures, transport across the NCs arrays occurs via two-dimensional variable range hopping. The effect of the quasi-2D structure and the presence of the conjugated linker in this context of charge transport mechanism are discussed in this work. Resistivity-based vapor sensing measurements reveal a selective sensitivity for non-polar analytes, which is facilitated by a large interparticle spacing of 30 ± 17 Å. The results presented in this work show how combining organic pi-systems and copper-deficient chalcocite NCs rewards electrically conductive, quasi-2D films, which are solution-processible and attractive for vapor sensing applications.

We have measured the structural, optical and electric properties of ternary $\text{Cu}_2\text{Se}_y\text{S}_{1-y}$ NC solids capped with oleylamine and the organic semiconductor molecule CoTAPc, respectively, and compared it to the binary compound Cu_2Se . While the structural and optical response to ligand

exchange and oxidation in air is rather similar for both materials, we have observed substantial differences in the charge carrier transport properties. Charge transport in $\text{Cu}_2\text{Se}_y\text{S}_{1-y}$ NC solids is dominated by electronic conduction, very sensitive to structural changes and largely unaffected by oxidation in air. Exchanging the surface ligand oleylamine with the organic π -system not only drastically increases electronic coupling in the $\text{Cu}_2\text{Se}_y\text{S}_{1-y}$ NC ensembles but also invokes an increase in the optical responsivity by eight orders of magnitude. Thus, ligand exchange with CoTAPc enables high conductivity and large responsivity in $\text{Cu}_2\text{Se}_y\text{S}_{1-y}$ NC films, which are much more robust against oxidation than their binary Cu_2Se analogues.

In-situ GISAXS is a powerful technique to probe the superlattice formation of NCs. We have obtained the direct evidence of superlattice formation of anisotropic $\text{Cu}_{1.1}\text{S}$ nanocrystals at the liquid-air interface. We have monitored the structural evolution of a $\text{Cu}_{1.1}\text{S}$ nanodiscs superlattices on the DMSO surface during self-assembly followed by ligand exchange. We used the Rectangular-shape CoTAPc cross-linker to exchange the native Olm ligands and investigated the *in-situ* structural changes of the superlattices. We determined the superlattice parameters from the scattering patterns by fitting the peaks and monitor the orientation of the atomic lattices of NDs within the superlattice. We arrive at the following conclusions: The nanodiscs order into hexagonal superlattice and the lattice parameter does not change significantly during self-assembly through solvent evaporation. A continuous in-plane contraction of the superlattice occurs during ligand exchange, which is attributed solely to the continuous removal of the Olm by the smaller CoTAPc molecules. The superlattice contracts isotropically, preserving the initial structural symmetry with a resultant contraction of lattice parameter by 5%. The NDs within the superlattice have preferential orientation with respect to the liquid surface. The coupling of adjacent NDs via OSC molecules produces electronically coupled highly conductive and order superlattices.

Part III

Collaborated Publications

5. Collaborated Publication 1

Understanding the Formation of Conductive Mesocrystalline Superlattices with Cubic PbS Nanocrystals at the Liquid/Air Interface

(Santanu Maiti, Sonam Maiti, Andre Maier, Jan Hagenlocher, Andrey Chumakov, Frank Schreiber, Marcus Scheele published in J. Phys. Chem. C 2018, DOI: 10.1021/acs.jpcc.8b11518)

We report the formation of conductive mesocrystalline superstructures of cubic PbS nanocrystals (NCs) through directional cross-linking with organic semiconductors at the liquid/air interface monitored simultaneously by in situ grazing incidence small angle X-ray scattering and grazing incidence X-ray diffraction. We determine the superlattice type, its symmetry and parameters, and the atomic orientation of NCs from the time-resolved scattering patterns. The superlattice contraction follows an exponential decay during ligand exchange, preserving always the two-dimensional square geometry. We attribute the contraction to the continuous replacement of oleic acid with smaller cobalt/copper 4,4',4'',4'''-tetraaminophthalocyanine molecules. In these superlattices, the NCs are directed with a $[100]_{AL}$ axis perpendicular to the liquid surface for the whole assembly period. The kinetics and structural results provide a direct correlation between the superstructure and their atomic orientation on the liquid surface during self-assembly followed by ligand exchange.

Methods

Synthesis of cubic PbS Nanocrystals: The details on the synthesis of PbS nanocrystals can be found in the original publication.

Synthesis of Co/CuTAPc: The details on the synthesis of Co/CuTAPc can be found in the original publication.

Formation of NC Films at the Liquid/Air Interface and Ligand Exchange: At first, the nitrogen-flushed chamber is filled up to 5 mm below the window edge with acetonitrile. 200 μ L of the 2.5 μ M NC solution in a mixture of 1:2 hexane (97%, extra dry, nitrogen flushed, Acros Organics) to octane (99+%, extra dry, nitrogen flushed, Acros Organics) is dispersed on top of the acetonitrile at a rate of 1 mL/min. A nanoparticle film forms within a few seconds.⁵³ After beam alignment onto the liquid surface, the measurements before ligand injection are

done. After the investigations of the OA-capped NC film are finished, a 1 mg/mL solution in dimethyl sulfoxide (DMSO) of Co/CuTAPc is injected into the bulk acetonitrile liquid. The start of the injection process marks the time zero of our experiment. The subphase height was adjusted about every 15 min. For better control on the experiment, all the injection or dispersion processes are performed with the help of a syringe pump.

Raman Spectroscopy and electrical measurements:

Raman spectra (Horiba Jobin Yvon Labram HR 800 spectrometer) were collected using a He:Ne laser (wavelength 633 nm) as an excitation source and a CCD-1024 × 256-OPEN-3S9 detector.

The ligand-exchanged films were transferred onto commercially available bottom-gate, bottom-contact transistor substrates (Fraunhofer Institute for Photonic Microsystems, Dresden, Germany) with interdigitated Au electrodes of 10 mm width and 2.5 μm channel length. Two-probe electrical measurements were carried out using a Keithley 2634B dualsource measurement unit.

Ex Situ Characterization of the Ligand Exchanged Films:

Raman spectroscopy (**Figure 5.1a**) on the recovered exchanged films shows the presence of intense bands at wavenumbers $>1000\text{ cm}^{-1}$, which are a strong indication for the presence of the new Co/CuTAPc ligands on the surface of the NPs. It should be noted that we extensively washed the films with acetonitrile to remove excess/free ligand molecules. We compare the transport measurements of the ligand exchanged and self-assembled films in **Figure 5.1b**. The current–voltage (I – V) characteristics indicate an improvement of the current by 4 orders of magnitude for ligand exchanged film with respect to the native OA-capped PbS film. The enhancement of the electrical conductivity by 4 orders of magnitude (refer **Figure 5.4b**) for ligand-exchanged films is attributed to the formation of conductive PbS NC SLs by cross-linking with the phthalocyanine molecules.⁵⁵

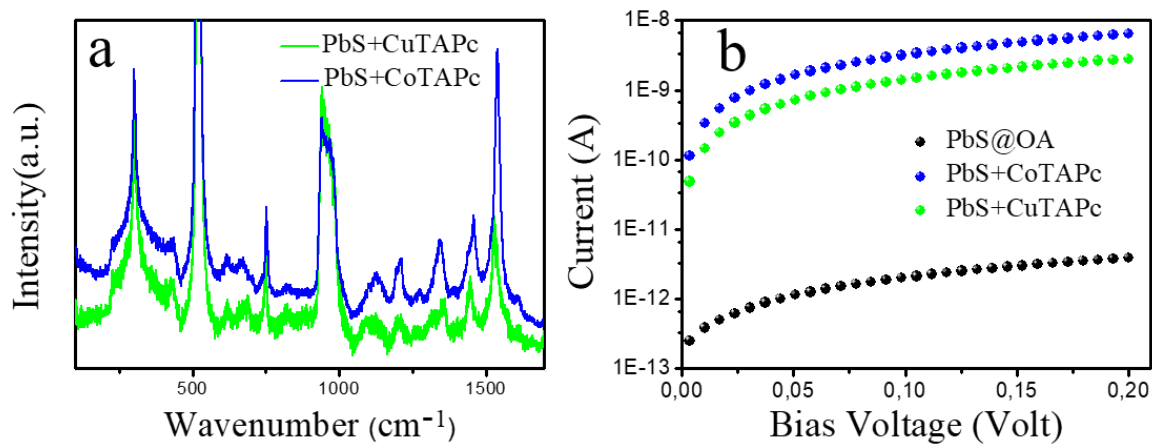


Figure 5.1(a) Raman spectroscopy data after ligand exchange films. **(b)** Current–voltage ($I-V$) characteristics of PbS NC films: OA-capped (black); exchange film with CoTAPc (blue) and CuTAPc (green); the graph is plotted on a logarithmic scale for better comparison.

6. Collaborated Publication 2

Correlated, Dual-Beam Optical Gating in Coupled Organic–Inorganic Nanostructures

(Kai M. Wurst, Dr. Markus Bender, Dr. Jannika Lauth, Sonam Maiti, Prof. Thomas Chassé, Prof. Alfred Meixner, Prof. Laurens D. A. Siebbeles, Prof. Uwe H. F. Bunz, Dr. Kai Braun, Dr. Marcus Scheele published in *Angewandte Chemie* 2018 doi.org/10.1002/anie.201803452)

In this manuscript, an optical switch with two distinct resonances is formed by combining PbS nanocrystals and the conductive polymer poly[sodium 2-(2-ethynyl-4-methoxyphenoxy)acetate] (PAE) into a hybrid thin film. Infrared excitation of the nanocrystals invokes charge transfer and consecutive polaron formation in the PAE, which activates the switch for excited-state absorption at visible frequencies. The optical modulation of the photocurrent response of the switch exhibits highly wavelength-selective ON/OFF ratios. Transient absorption spectroscopy shows that the polaron formation is correlated with the excited state of the nanocrystals, opening up new perspectives for photonic data processing. Such correlated activated absorption can be exploited to enhance the sensitivity for one optical signal by a second light source of different frequency as part of an optical amplifier or a device with AND logic.

Methods

Synthesis of PbS Nanocrystals: The details on the synthesis of PbS nanocrystals can be found in the original publication.

Synthesis of Poly[sodium 2-(2-ethynyl-4-methoxyphenoxy)acetate] (PAE-1): PAE-COOEt. The details on the synthesis of PAE-COOEt can be found in the original publication.

Ligand Exchange with TTFDA – Solid/Air Exchange: Three milligrams of [TBA]₂TTFDA was dissolved with 3 mL of methanol. Substrates for various characterization methods (FET, XPS, PDS, SEM, GIXD, etc.) were cleaned on using soap scrub, rinsed with distilled water, followed by isopropanol and acetone, blow-dried, UV/ozone cleaned for 5 min, and mounted onto a spin-coater. One drop of a filtered hexanes solution of nanoparticles (roughly 1 mg/mL)

was drop-cast onto the substrate and spun at 2000 rpm with a 1 s ramp for 15 s. At rest, the substrate was covered with the TTFDA solution (approximately 200 μL) and allowed to dry completely within roughly 10 min. While spinning at 2000 rpm, it was washed with methanol to spin-off excess TTFDA followed by hexanes to wash off the oleate. This procedure was repeated one more time to yield a continuous film.

Self-assembly and ligand exchange into hybrid PbS-PAE-1 thin films. The following described preparation procedure is schematically pictured in **Figure 6.1**. All steps were carried out under nitrogen atmosphere.

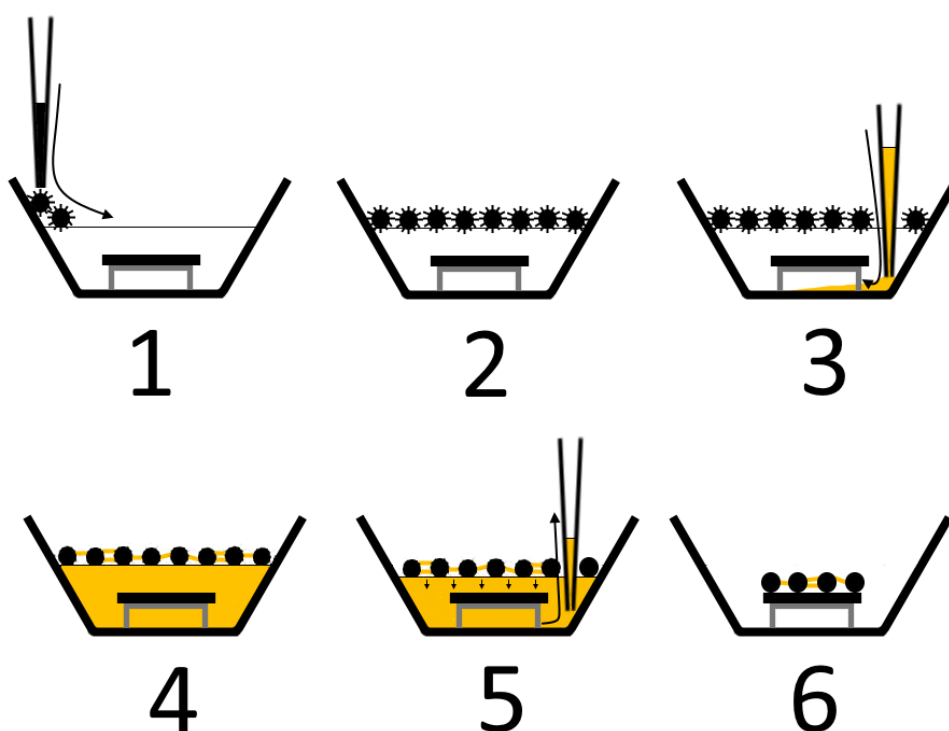


Figure 6.1 Schematically presentation of hybrid PbS-PAE-1 thin film fabrication. Individual steps are described in the continuous text.

First, the substrate (commercial FET substrate from the Fraunhofer institute for Photonic Microsystems, Dresden, Germany, with bottom-gate and bottom Au contacts of 30 nm height, 1 cm width and 2.5, 5, 10 or 20 μm channel lengths, or self-fabricated substrate with nanochannels) was placed on a stand in a Teflon crucible followed by addition of 8 mL acetoneitrile. 100 μL of a 1 μM PbS NC solution in a 1:6 mixture of octane and hexane was slowly added on the edge of the crucible. After waiting for about 3 minutes, hexane and octane have evaporated completely yielding a thin PbS NC layer on top of the acetoneitrile subphase

(Figure 6.1, step 2). In the next step (Figure 6.1, panel 3), 200 μL of PAE-1 saturated solution in methanol are added to the bottom of the crucible by punctuating the floating PbS nanoparticle layer. After waiting for 2 h, the ligand completely diffused through the subphase revealing a homogeneous yellow solution. During this period (step 4), the native oleic acid ligand of the PbS nanoparticles was replaced with the organic semiconductor. The subphase was carefully removed (step 5) and the hybrid PbS-PAE-1 film was deposited on the substrate (step 6). After waiting for 15 min, the sample dried completely. Excess organic semiconductor was removed by washing the film carefully with 200 μL methanol. Afterwards, the sample was baked out for 30 min at 80°C followed by storing in vacuum overnight.

Raman spectroscopy

Raman spectra were acquired using a Horiba Jobin Yvon Labram HR 800 spectrometer with a CCD-1024 \times 256-OPEN-3S9 detector. Excitation for Raman was performed using a frequency doubled He:Ne laser at a wavelength of 633 nm.

Hybrid thin films of PbS NCs cross-linked with PAE-1 were assembled as floating membranes at the acetonitrile/ N_2 interface and coated onto solid supports (see **Figure 6.2a** for Raman spectroscopy).

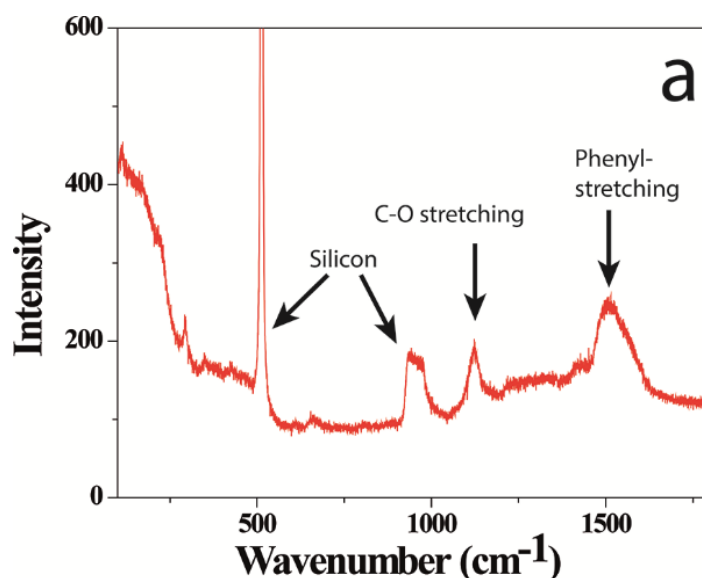


Figure 6.2(a) Raman spectrum of a PbS-PPE-1 film, using a 1.96 eV laser. While the Oleic acid-capped PbS NCs do not exhibit any distinct Raman bands, after ligand exchange with PPE-1, the C-O as well as the phenyl-stretching bands of the polymer are clearly visible.

Appendix A

Supporting information

Electronically Coupled, Two-Dimensional Assembly of $\text{Cu}_{1.1}\text{S}$ Nanodiscs for Selective Vapor Sensing Applications

Sonam Maiti^{1,2}, *Santanu Maiti*², *Yvonne Joseph*³, *Andreas Wolf*⁴, *Wolfgang Brütting*⁵, *Dirk Dorfs*⁴,
Frank Schreiber^{2,6}, and *Marcus Scheele*^{1,6,*}

¹ Institute of Physical and Theoretical Chemistry, University of Tübingen, Auf der Morgenstelle 18, 72076 Tübingen, Germany.

² Institute of Applied Physics, University of Tübingen, Auf der Morgenstelle 10, 72076 Tübingen, Germany

³ Institute of Electronic and Sensor Materials, TU Bergakademie Freiberg, Gustav-Zeuner-Straße 3, 09599 Freiberg, Germany.

⁴ Institute of Physical Chemistry and Electrochemistry, Leibniz Universität Hannover, Callinstr. 3A, 30167 Hannover, Germany

⁵ Institute of Physics, University of Augsburg, Universitätsstrasse 1, 86159 Augsburg, Germany

⁶ Center for Light-Matter Interaction, Sensors & Analytics LISA+, University of Tübingen, Auf der Morgenstelle 15, 72076 Tübingen, Germany.

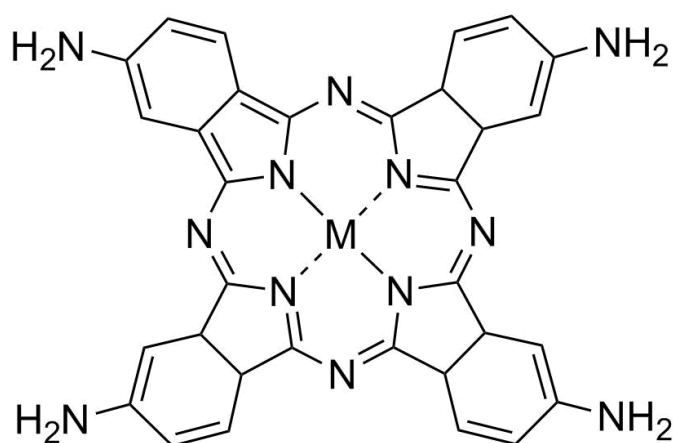


Figure S2.1 Structural formula of Cu-4,4',4'',4'''-tetraaminophthalocyanine (Cu4APc) with M = Cu.

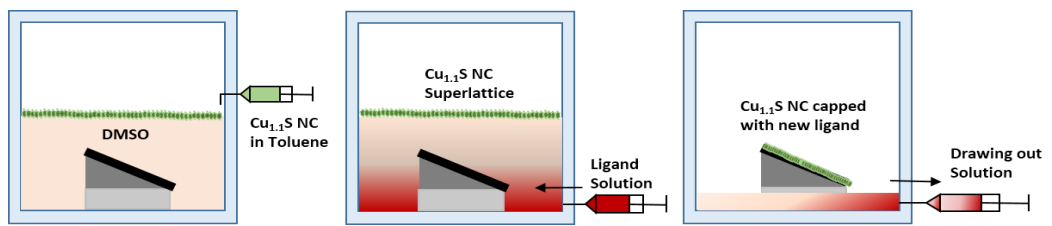


Figure S2.2 Ligand exchange at the liquid-air interface.

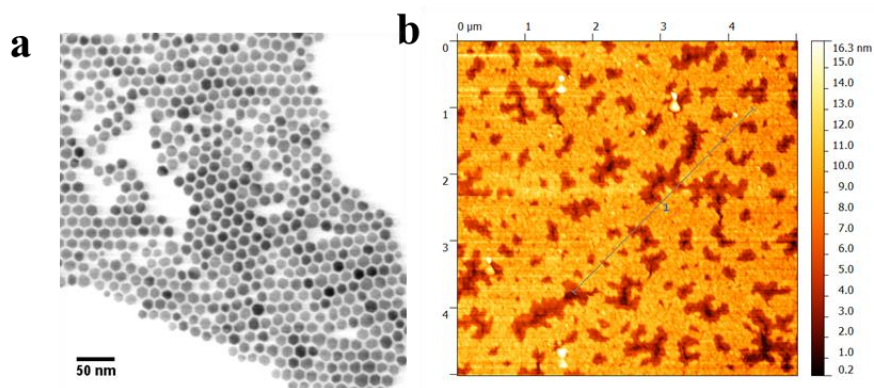


Figure S2.3 TEM image of Cu_{1.1}S nanodiscs of an average diameter of 12.7 ± 1.7 nm, and a thickness of 5.8 ± 0.7 nm. (b) AFM image of Cu_{1.1}S nanocrystal film after ligand exchange.

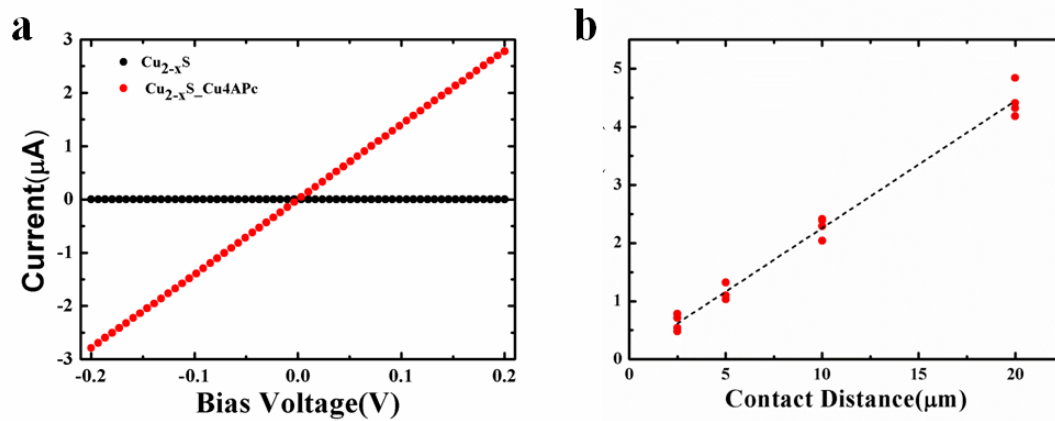


Figure S2.4(a) Current-voltage (I-V) curves of $\text{Cu}_{1.1}\text{S}$ nanocrystal films prepared by interface method before and after ligand exchange (black and red curves, respectively). The curves were recorded under ambient conditions. **(b)** Plot of the total resistance vs. channel length $\text{Cu}_{1.1}\text{S}$ nanocrystal film after ligand exchange with Cu4APc. The contact resistance is extracted by a linear fit to this data

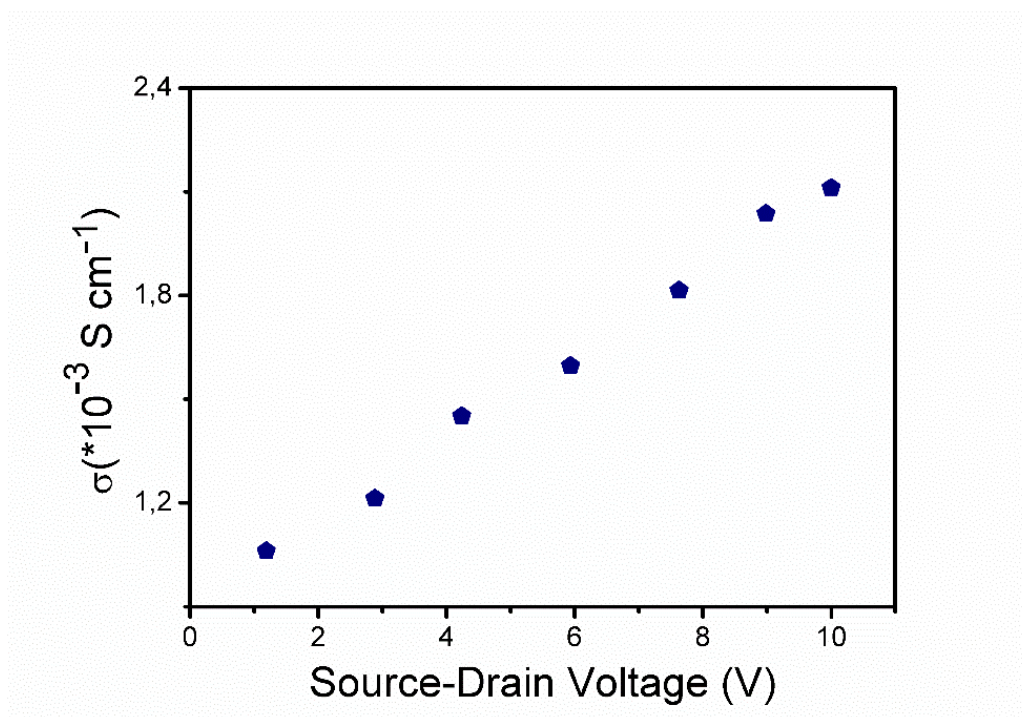


Figure S2.5 Plot of the total resistance vs. channel length Cu_{1.1}S nanocrystal film after ligand exchange with Cu4APc. The contact resistance is extracted by a linear fit to this data.

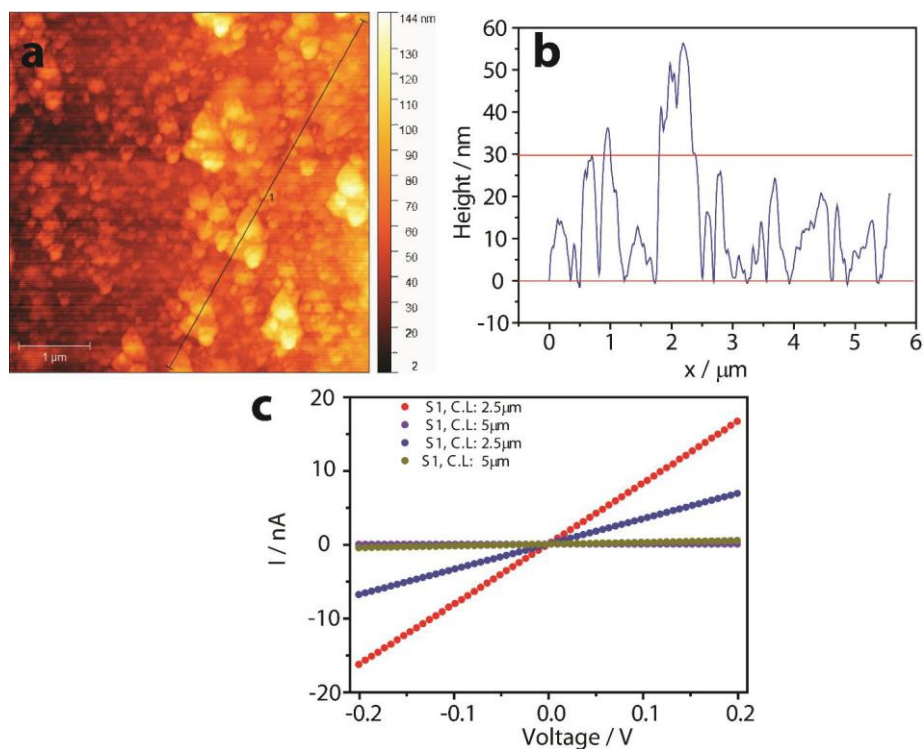


Figure S2.6 a) Atomic force micrograph and b) extracted height profile of a thicker sample with 5-10 monolayers. c) I/V characteristics of a thick film at different contacts and channel lengths. The conductivity is 2-3 orders of magnitude smaller than in the monolayered films shown in the main body of the manuscript.

Appendix B

Supporting Information

Dye-Sensitized Ternary Copper Chalcogenide Nanocrystals: Optoelectronic Properties, Air Stability and Photosensitivity

*Sonam Maiti^{1,2}, Santanu Maiti², Ali Hossain Khan^{3,4}, Andreas Wolf⁵, Dirk Dorfs⁵, Iwan Moreels^{3,4},
Frank Schreiber^{2,6} and Marcus Scheele^{1,6} **

¹ Institute of Physical and Theoretical Chemistry, University of Tübingen, Auf der Morgenstelle 18, 72076 Tübingen, Germany.

² Institute of Applied Physics, University of Tübingen, Auf der Morgenstelle 10, 72076 Tübingen, Germany

³ Istituto Italiano di Tecnologia, Via Morego 30, 16163 Genova, Italy

⁴ Department of Chemistry, Ghent University, Krijgslaan 281-S3, 9000 Gent, Belgium

⁵ Institute of Physical Chemistry and Electrochemistry, Leibniz Universität Hannover, Callinstr. 3A, 30167 Hannover, Germany

⁶ Center for Light-Matter Interaction, Sensors & Analytics LISA+, University of Tübingen, Auf der Morgenstelle 15, 72076 Tübingen, Germany.

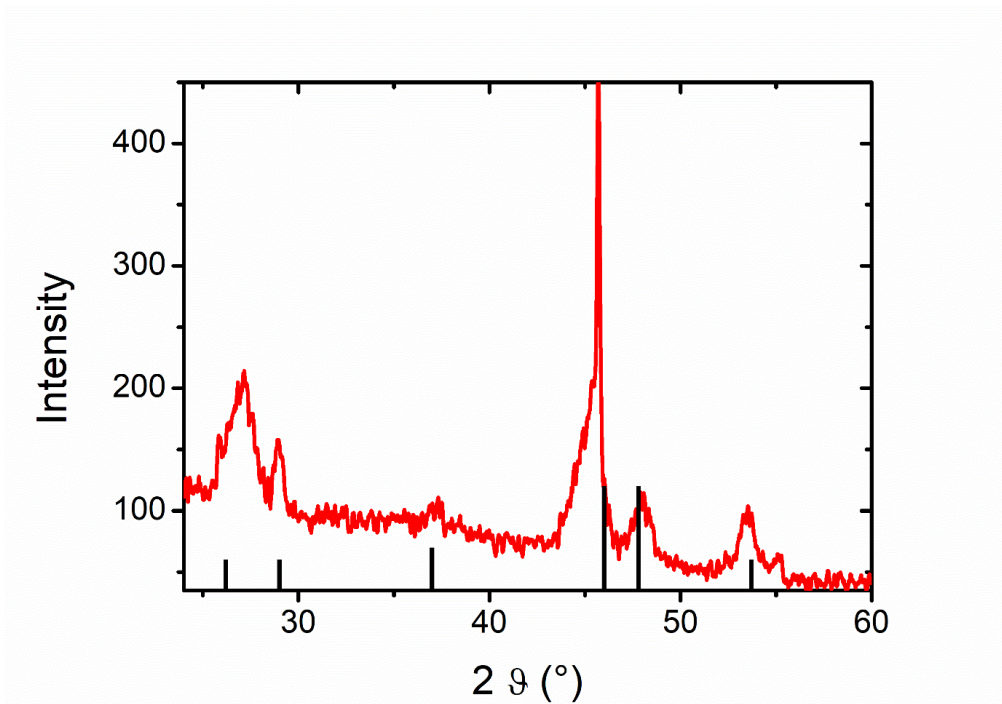


Figure S3.1 XRD pattern of as-synthesized $\text{Cu}_2\text{S}_y\text{Se}_{1-y}$ NCs. The reference structural data shows hexagonal Cu_2S (PDF card #: 84-0209). The reflections at 29° , 37° and 48° are absent in the cubic structure, and therefore characteristic for the hexagonal phase here.

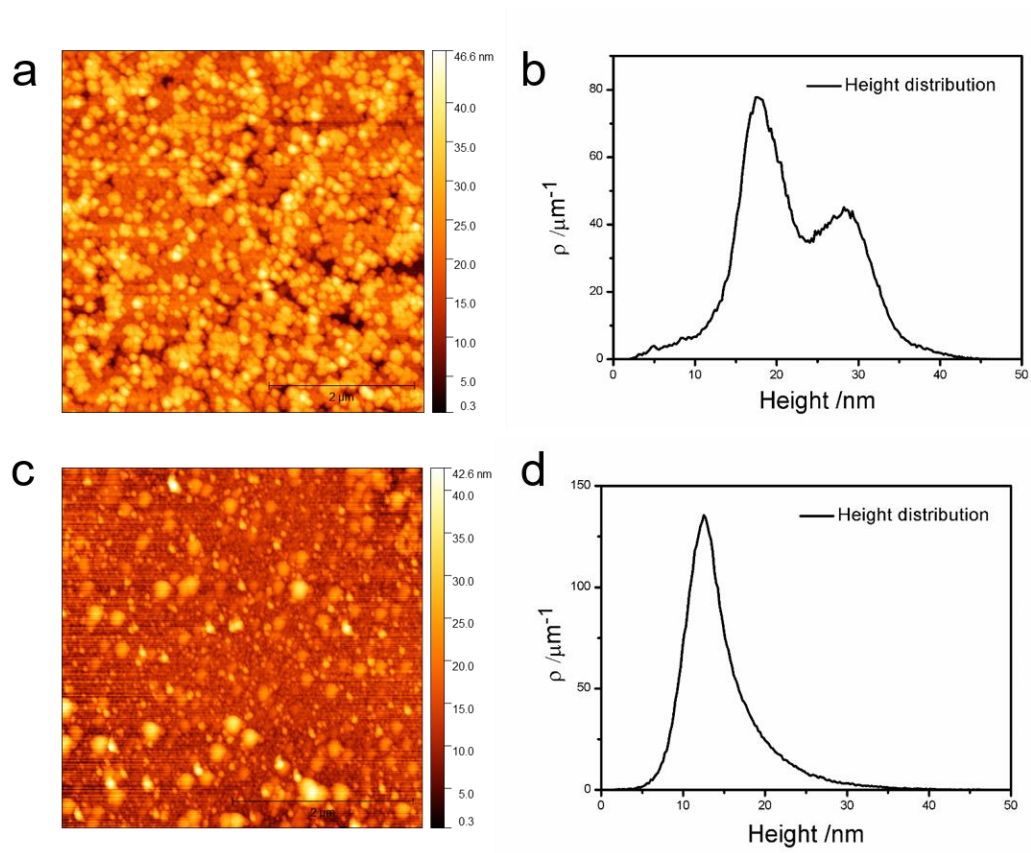


Figure S3.2 AFM images and extracted height profile of $\text{Cu}_2\text{Se}_y\text{S}_{1-y}$ (top) and Cu_{2-x}Se (bottom).

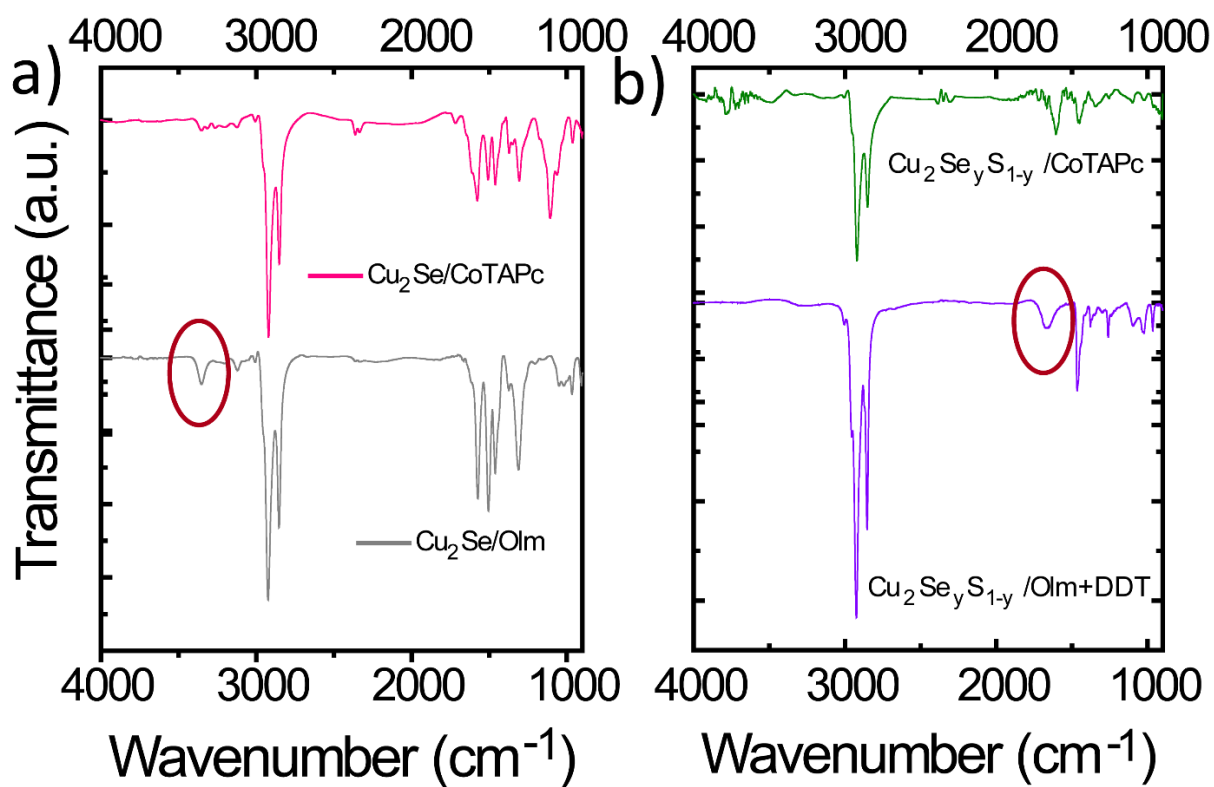


Figure S3.3 FT-IR spectra of **a)** Cu_2Se and **b)** $\text{Cu}_2\text{Se}_y\text{S}_{1-y}$ NC films, both before and after ligand exchange with CoTAPc. Characteristic bands for oleylamine, which disappear during ligand exchange have been encircled in red. Note: Since CoTAPc also contains $-\text{NH}_2$ and $-\text{CH}$ vibrations, no quantitative description of the exchange efficiency can be made from this experiment.

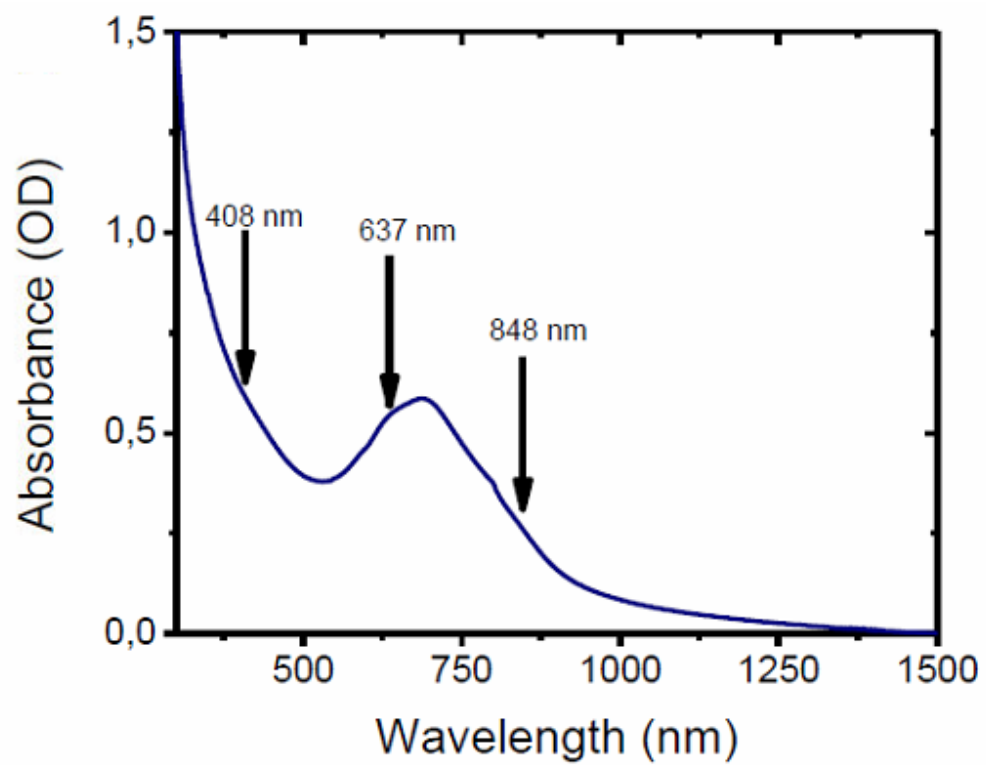


Figure S3.4 UV/VIS absorption spectrum of pure CoTAPc.

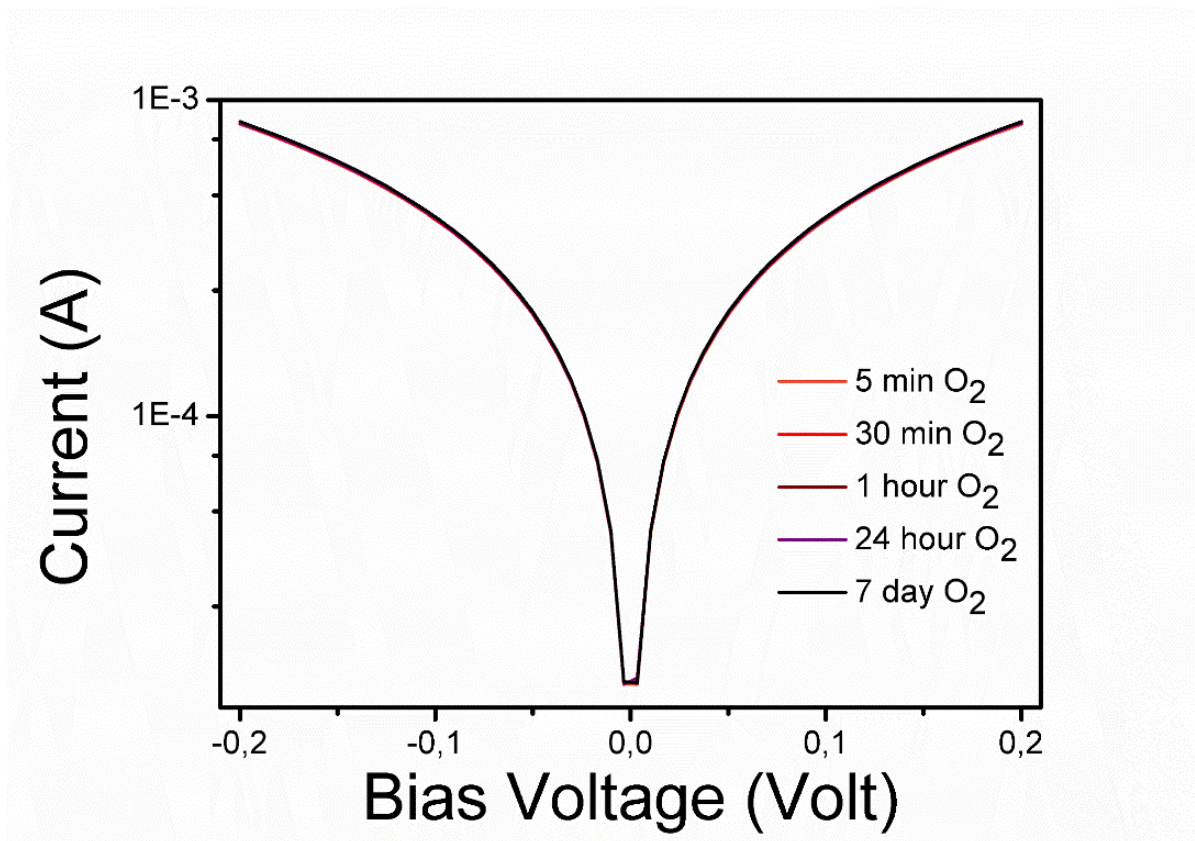


Figure S3.5 Current/Voltage characteristics of a $\text{Cu}_{2-x}\text{Se}_y\text{S}_{1-y}/\text{CoTAPc}$ thin film at varying exposure times to air. The current was measured once the device was removed from the inert atmosphere of the glovebox and subsequently recorded from 5 minutes to 7 days.

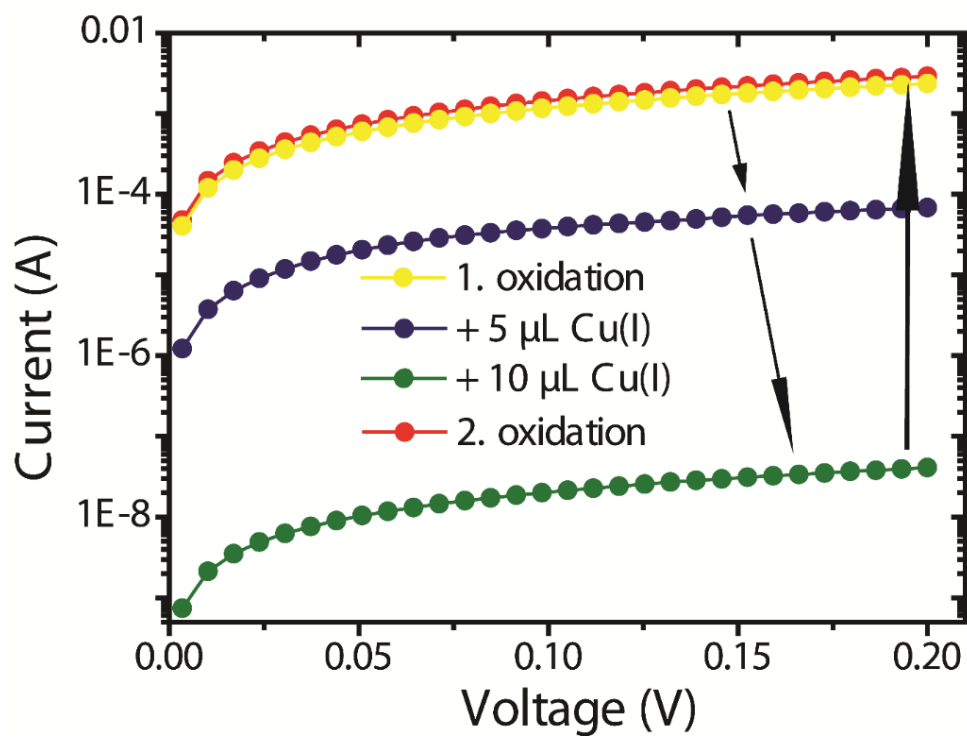


Figure S3.6 Current–voltage characteristics of a $\text{Cu}_2\text{Se}/\text{OLm}$ film after a first oxidation in air (yellow), after treatment with 5 μL of a 0.04 mmol/L solution of $[\text{Cu}(\text{CH}_3\text{CN})_4]\text{PF}_6$ (blue), after treatment with 10 μL of the same solution and after 15 min of oxidation in air.

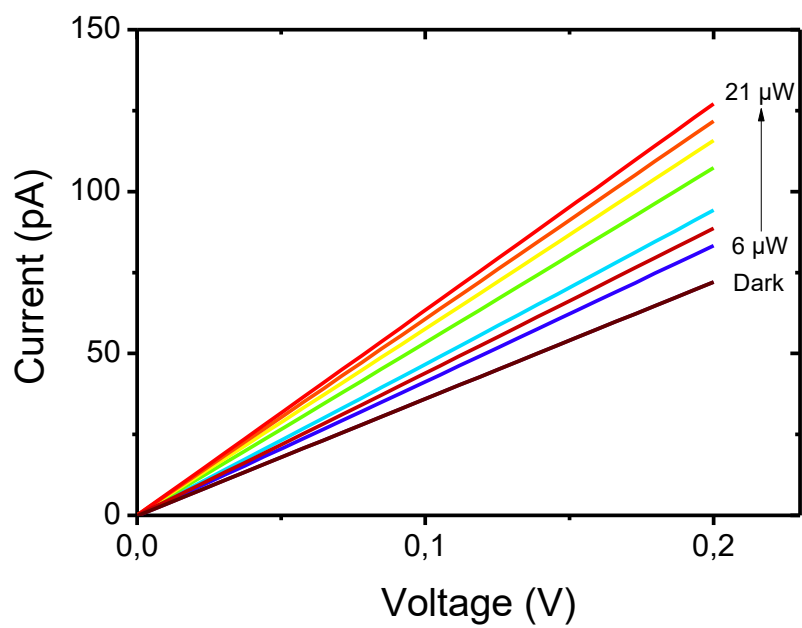


Figure S3.7 Current–voltage characteristics of a typical $\text{Cu}_{2-x}\text{Se}_y\text{S}_{1-y}/\text{OLm}$ film at different absorbed optical power values provided by a 408 nm laser diode.

Appendix C

Supporting Information

In-situ Formation of Electronically Coupled Superlattice of Cu_{1.1}S Nanodiscs at the Liquid/Air Interface

Sonam Maiti^{1,2}, *Santanu Maiti**¹, *Andre Maier*², *Rupak Banerjee*³, *Chen Shen*⁴, *Bridget M. Murphy*^{5,6},
Marcus Scheele^{2,7}, *Frank Schreiber*^{1,7}

¹Institute of Applied Physics, University of Tübingen, Auf der Morgenstelle 10, 72076 Tübingen, Germany.

²Institute of Physical and Theoretical Chemistry, University of Tübingen, Auf der Morgenstelle 18, 72076 Tübingen, Germany.

³Department of Physics, Indian Institute of Technology Gandhinagar, Palaj, Gandhinagar 382355, India.

⁴Deutsches Elektronen-Synchrotron DESY, Notkestraße 85, D-22607 Hamburg, Germany

⁵Institute for Experimental and Applied Physics, Kiel University, D-24098 Kiel, Germany

⁶Ruprect Heansel Laboratory, Kiel University, D-24098 Kiel, Germany

⁷Center for Light-Matter Interaction, Sensors & Analytics LISA+, University of Tübingen, Auf der Morgenstelle 15, 72076 Tübingen, Germany

Contents

- Experimental Details.
- Supplementary Figures
- Supplementary Table

- **Experimental Methods**

Synthesis of Cu_{1.1}S Nanocrystals: Cu_{1.1}S NDs were prepared by adapting the heat-up synthesis procedure from Xie et al.³⁶

Synthesis of Ligands: Co-4,4',4'',4''',4''''-tetraaminophthalocyanine (Co4APc) was purchased from Abcr and used without further purification.

***In-situ* formation of NC film at the liquid/air interface and ligand exchange:**

At first, the nitrogen flushed chamber is filled up to 5 mm below the window edge with dry, oxygen free DMSO (99,7+%, extra dry, Acros organics). Then 200 μ L of the 5 μ M ND solution in Toluene (97%, extra dry, nitrogen flushed, Acros Organics) is dispersed on top of the acetonitrile at a rate of 1 mL/min. The time resolved GISAXS patterns are collected afterwards from the ND film.

After the investigations on the oleylamine capped NC film are finished, the ligand solution (1mg/mL solution of CoTAPc in DMSO) is injected in the bulk DMSO. The start of the injection process marks the time zero of our experiment. The subphase height was adjusted about every 15 minutes for perfect alignment. For better control on the experiment, all the injection or dispersion processes are performed with the help of a syringe pump.

***In-situ* Grazing Incidence Small Angle X-ray Scattering (GISAXS):**

In-situ GISAXS measurements were performed at the Deutsches Elektronen-Synchrotron (DESY) in Hamburg, Germany at the Liquid Interface Scattering Apparatus (LISA), P08 beamline. The x-ray beam energy was set at 18 keV by using a Si(111) double crystal monochromator and Ge(311) Large-Offset-Monochromator, focused with CRL lens.^{197, 198} A beam of size 100 μ m x 400 μ m (V x H) was illuminated on the liquid surface at a grazing angle of 0.065 degree, set by the double crystal deflector of LISA.¹⁹⁹ The GISAXS signals were collected with a Lambda detector, having a pixel size of 55 x 55 μ m². The detector was placed at a distance of 1103 mm and each GISAXS images were collected over 5 seconds of exposure time.

Instrumentation

Scanning transmission electron microscopy (STEM, Hitachi SU 8030 microscope operating at 30 kV) was employed to determine the particle size and shape. The surface

morphology was measured by AFM using a JPK Nanowizard II instrument in tapping mode under ambient conditions. Image analysis was performed with Gwyddion. We perform Raman spectroscopy to ratify the ligand exchange in the nanodisc superlattices over depositing them onto Si-substrates. Raman spectra were acquired using a Horiba Jobin Yvon Labram HR 800 spectrometer with a CCD-1024 × 256-OPEN-3S9 detector. Excitation for Raman was performed using a He:Ne laser (wavelength 633 nm). The superlattice films were illuminated at room temperature with the excitation in the range of 350-1800 cm^{-1} . Electrical measurements were performed in a glovebox at room temperature with a homemade probe station using a Keithley 2634B dual source-meter unit, controlled by the included test script builder program. The NC films after ligand exchange were deposited on a commercially available bottom-gate, bottom-contact transistor substrates (Fraunhofer Institute for Photonic Microsystems, Dresden, Germany) with interdigitated Au electrodes of 10 μm width and 2.5 μm channel length followed by annealing at 250°C for 2 h under nitrogen atmosphere.

- **Supplementary Figures**

a) TEM image of Olm-passivated $\text{Cu}_{1.1}\text{S}$ NDs. b) Structural formula of CoTAPc.

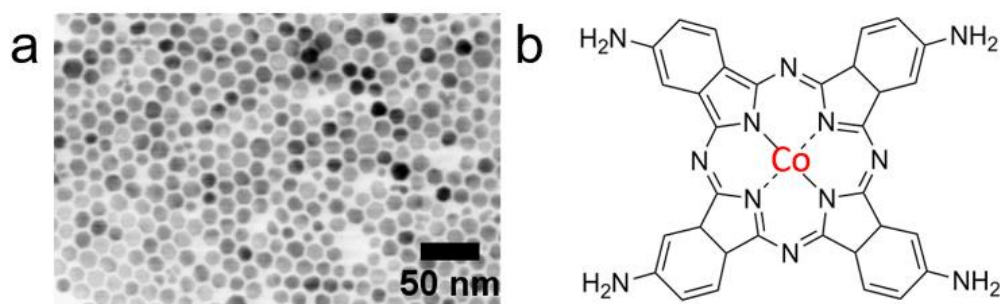


Figure S4.1 a) TEM image of Olm-passivated $\text{Cu}_{1.1}\text{S}$ NDs. b) Structural formula of CoTAPc.

Figure S4.1a shows a typical transmission electron microscopy (TEM) image of as-synthesized $\text{Cu}_{1.1}\text{S}$ NCs. The NCs are disc in shape (i.e. NDs) and have two hexagonal and six rectangular side facets. The NCs have an average in-plane diameter (d) and thickness of 12.7 ± 0.5 nm and 5.6 ± 0.5 nm, respectively. The NC surfaces are encapsulated with native oleylamine (Olm) and dispersed in toluene. Here, we use rectangular-shaped CoTAPc OSC molecules (size: 1.3 ± 0.6 nm) for the ligand exchange reaction. The CoTAPc molecule has four amines ($-\text{NH}_2$) groups on their backbone as shown the structural formula in **Figure S4.1b**.

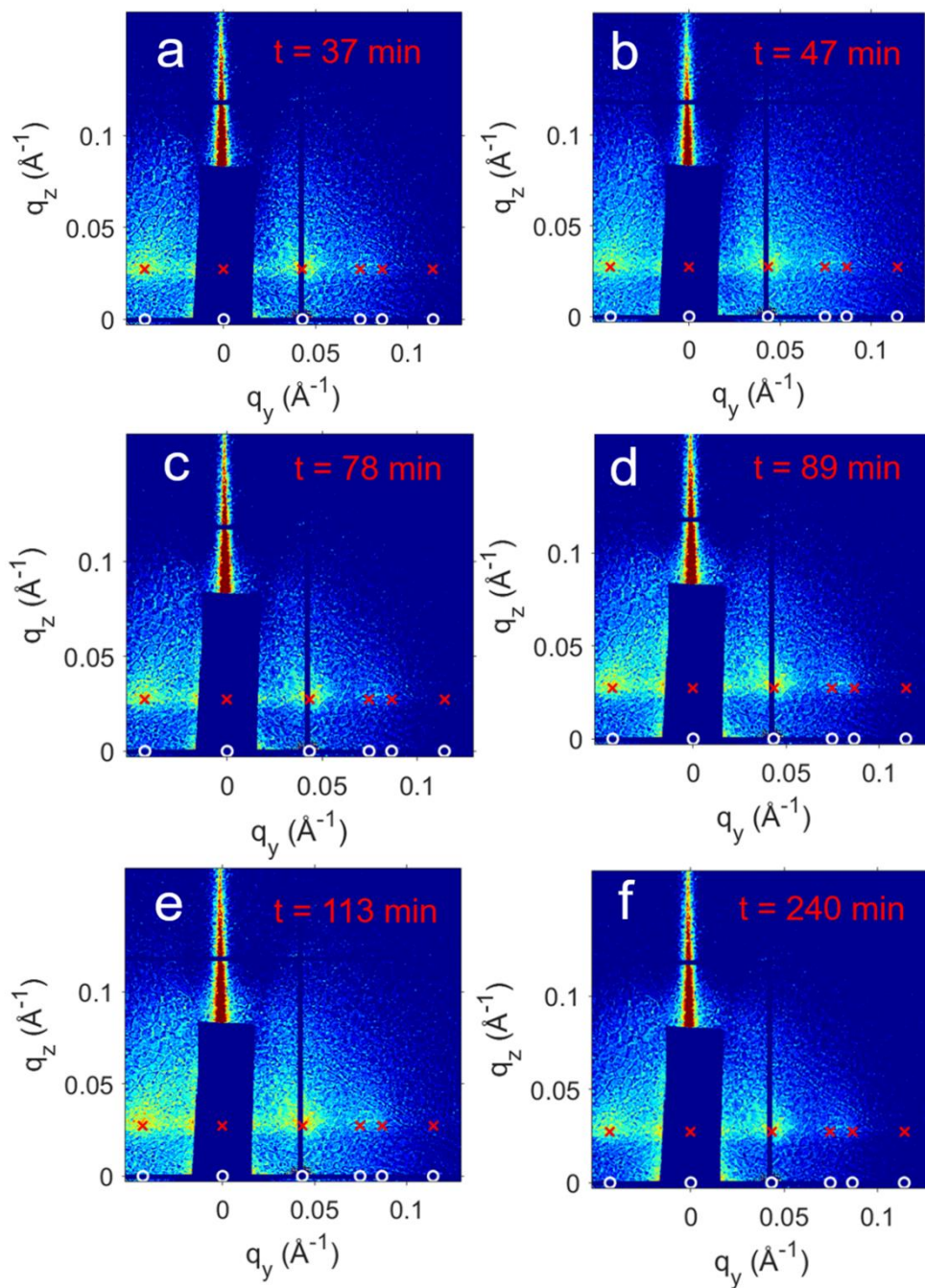


Figure S4.2 a-f) GISAXS patterns from the self-assembly without ligand exchange at different intermediate times marked at the right corner of each images. The pink and red spots are the simulated diffraction peak position of bcc superlattice considering DWBA method.

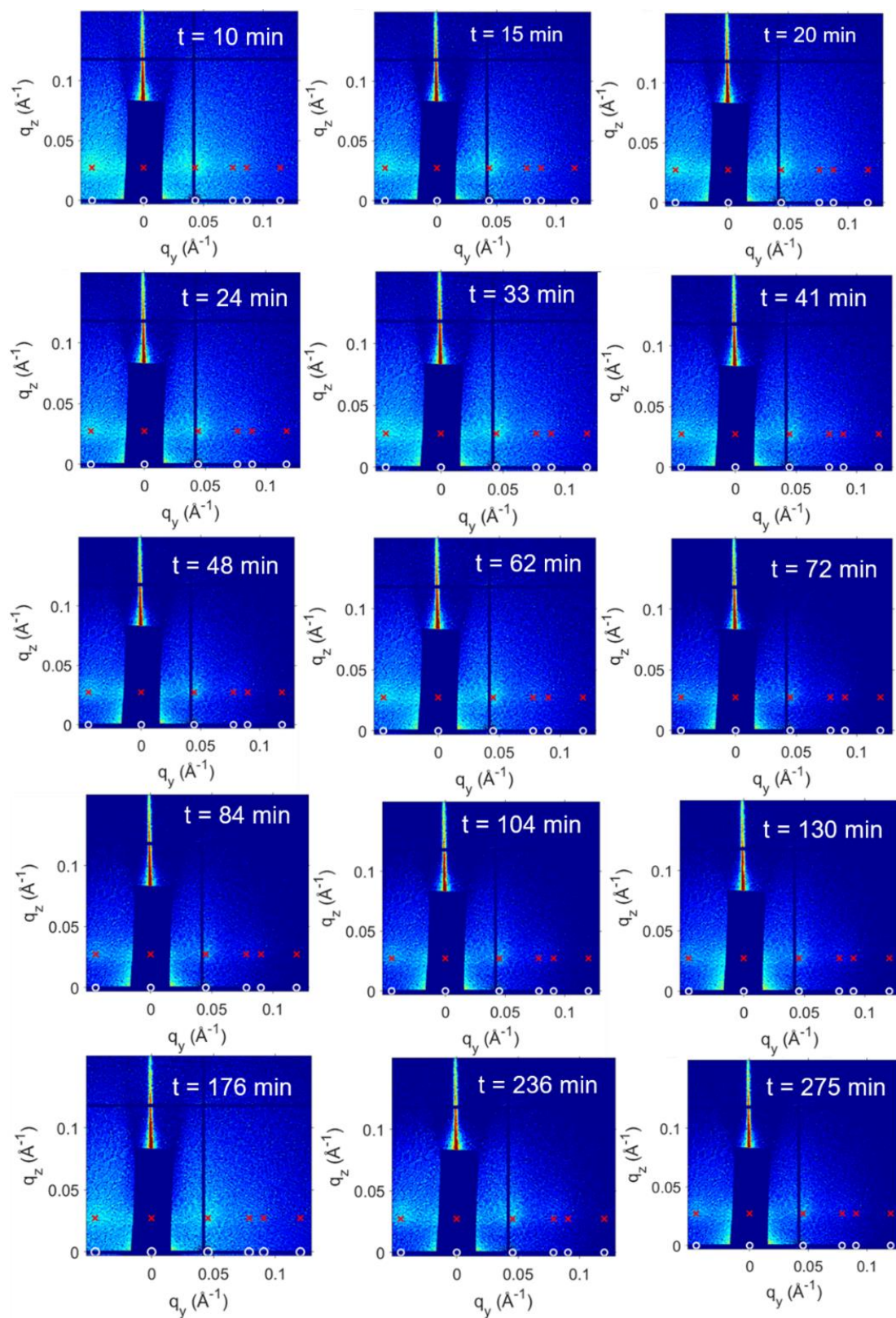


Figure S4.3 GISAXS patterns from the self-assembly during ligand exchange process at different intermediate times marked at the right corner of each images. The pink and red spots are the simulated diffraction peak position of bcc superlattice considering DWBA method.

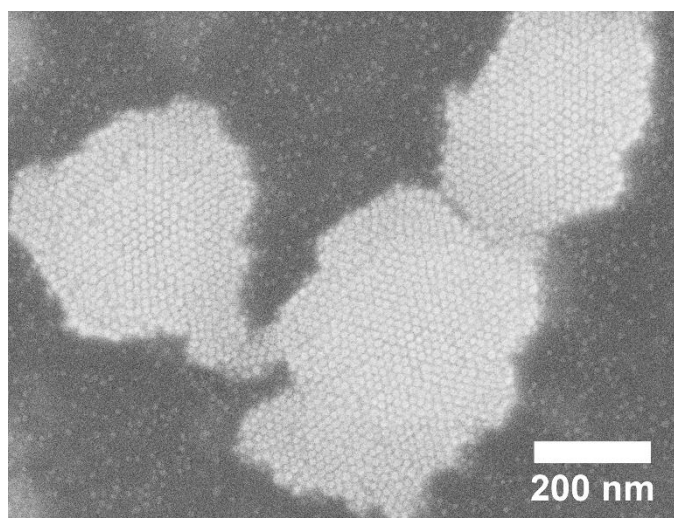


Figure S4.4 STEM image of $\text{Cu}_{1.1}\text{S}$ NC superlattice

Further material characterization

Atomic force micrograph of the ligand-exchange nanocrystal superlattice

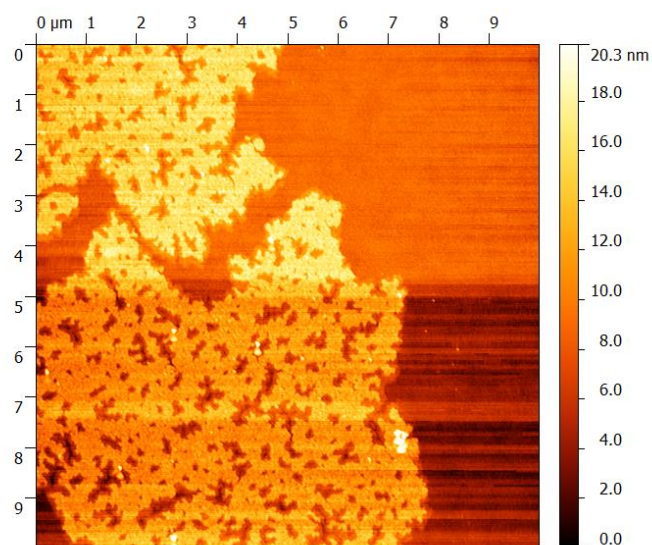


Figure S4.5 Atomic force micrograph of the nanocrystal superlattice after complete ligand-exchange and drying on a silicon substrate. The average height of the superlattice is ~ 11 nm.

- Supplementary Table

Table 2. Superlattice parameters

Waiting time (min)	a = b = c (Å)	$\alpha = \beta$ (deg)	γ (deg)	SG Symmetry
-42	171	90	120	P6mm
0	169	90	120	P6mm
6	168	90	120	P6mm
10	166	90	120	P6mm
15	165	90	120	P6mm
20	164	90	120	P6mm
24	163	90	120	P6mm
29	162,5	90	120	P6mm
33	162	90	120	P6mm
36	161,5	90	120	P6mm
41	161	90	120	P6mm
48	160,5	90	120	P6mm
62	160	90	120	P6mm
72	160	90	120	P6mm
78	160	90	120	P6mm
84	160	90	120	P6mm
93	160	90	120	P6mm
104	160	90	120	P6mm
114	160	90	120	P6mm
130	160	90	120	P6mm
176	160	90	120	P6mm
236	160	90	120	P6mm
276	160	90	120	P6mm

List of Symbols and Abbreviations

eV	Electron Volt
E_g	Bulk energy gap
k	Wave vector
m^*	Effective mass of the electron or hole
\hbar	Reduced Planck constant
R	Nano particle size
e	Charge of an electron
ϵ_∞	Dielectric constant outside the nanocrystal
k_B	Boltzmann Constant
COIN	Coupled Organic-Inorganic Nanostructure
STEM	Scanning Transmission Electron Microscopy
TEM	Transmission Electron Microscopy
EDX	Energy-Dispersive X-ray Spectroscopy
Δx	Distance between organic monolayers / distance between stacking planes
$\rho(x)$	Charge density
n	Number of molecules per unit area and per discretization interval Δx
$V(x)$	Electrostatic potential at the position x from the substrate
ϵ_0	Vacuum permittivity
R	Resistance
R_s	Sheet resistance
L	Length of the channel
w	Width of the channel
R_0	Baseline Resistance
K_b	Binding Constant
θ	Electron off-axis angle with respect to the surface normal
NCs	Nanocrystals
NP	Nanoparticle
QDs	Quantum Dots
NIR	Near Infra Red
LSPR	Localized Surface Plasmon Resonance

FET	Field-Effect Transistor
LED	Light- Emitting Diode
PVCs	Photovoltaic Cells
0D	Zero-Dimensional
1D	One-Dimensional
2D	Two-Dimensional
3D	Three-Dimensional
VRH	Variable-Range Hopping
HOMO	Highest Occupied Molecular Orbital
LUMO	Lowest Unoccupied Molecular Orbital
FWHM	Full Width at Half Maximum
GISAXS	Grazing-Incidence Small-Angle Scattering
α_c	Critical angle
S(q)	Structure factor
P(q)	Form factor
DWBA	Distorted wave Born approximation
UV–vis–NIR	Ultraviolet–Visible–Near Infrared
FTIR	Fourier Transform Infrared (spectroscopy)
OLm/Olm	Oleylamine
DMSO	Dimethyl Sulfoxide
XRD	X-ray Diffraction
σ	Electronic conductivity
n	Density of conducting electrons
τ	Mean free time
ρ	Resistivity
ρ_0	Residual resistivity
G	Conductance
ξ	Localization length
r	Hopping distance
ΔE	Energy difference
g_0	Density of states near the Fermi surface
D	Dimension

ESVRH Efros-Shklovskii Variable Range Hopping

MVRH Mott variable range hopping

η Quantum efficiency

N_λ Number of photons of wavelength λ

G_i Internal (photoconductive) gain

τ Free carrier lifetime

T_i Transit time

R_i Responsivity

i_{ph} Photocurrent

P_{in} Input optical power

f Modulation frequency

4M2P 4-methyl-2-pentanone

TLM Transmission Line Method

Pc Phthalocyanine

OSC Organic Semiconductor

DOS Density of States

GIXD Grazing Incidence X-ray Diffraction

AFM Atomic Force Microscopy

CuS Copper Sulfide

Cu₂Se Copper Selenide

Cu₂Se_yS_{1-y} Copper Selenide Sulfide

List of Tables

Table 1. The experimental sensor responses i.e. relative changes of resistance at saturation $[R/R_0]_s$ and binding constants K_b obtained from the Langmuir fits for $\text{Cu}_{1.1}\text{S}/\text{Cu}_4\text{APc}$ thin films at room temperature.	47
Table 2. Superlattice parameters.....	103

List of Figures

Figure 1. Overview of the thesis will describe.....	13
Figure 2. A schematic illustration of the change of the electronic properties when the size of a semiconductor decreases. At the left, an energy band diagram for a macrocrystalline semiconductor is shown, $E_{g(\infty)}$ being the bandgap. While the picture on the right represents the situation when the dimensions of the semiconductor are smaller than those of the exciton, $E_{g(NCs)}$ is the energy of the lowest excited state (adapted from Steigerwald and Brus) ²⁶	15
Figure 3. (a) & (b) TEM images of $Cu_{1.1}S$ NCs.....	18
Figure 4. (a) & (b) TEM images of $Cu_{2-x}Se_yS_{1-y}$ NCs.	19
Figure 5. Energy level diagram of a COIN interface. In this example, the inorganic IS_h state is tuned by the QD diameter to align with the HOMO of the OSC as for instance (adopted from Scheele at al. ⁵¹)	20
Figure 6. Schematic representation of a possible mechanism for hole and electron transport in a COIN system.	21
Figure 7. (a) Two-dimensional confinement of the self-assembly process, as is studied mostly throughout this thesis. The NCs are confined at a liquid-air/ N_2 interface, which can result in superlattices which have a thickness of an NC monolayer. (b) STEM image of $Cu_{1.1}S$ NCs superlattice prepared at liquid-air interface.	25
Figure 8. Typical experimental geometry of grazing-incidence X-ray scattering experiments.	27
Figure 9. (a) Typical GISAXS pattern obtained from ex-situ $Cu_{2-x}Se$ NCs superlattice film. Here, the incoming X-ray photons have an energy of 8 keV and hit the surface at a glancing angle of 0.2° (b) GISAXS patterns of $Cu_{1.1}S$ NDs superlattices film at the liquid/air interface. The red circles and pink boxes are the simulated diffraction patterns considering a hexagonal superlattice along the in-plane direction. Note that the direct beam, i.e. the reflection at $q_y=0$ and $q_z=0$, is usually blocked with a beamstop to prevent damage to the detector since it is very intense.	28
Figure 10. Schematic of interparticle contraction observed by GISAXS.	29
Figure 11. The density of states vs energy for a doped semiconductor exhibiting a soft Coulomb gap. The gap width is Δ . ⁸⁴	31
Figure 12. a) A sketch of typical thin film photoconductive photodetector. Interdigitate electrode structure is deposited onto the surface of active semiconductor. (b) A photodetector	

geometry that is typically used for NC-based devices: thin NC layer is deposited on top of the pre-patterned electrode structure. Au is shown as an example of metal contact material. (adapted from Talapin et al.)⁷⁰33

Figure 13. (a) Schematic representation of Cu-chalcogenide based CONIs assembly exciting with the suitable light source. (b) Photocurrent response upon exposure of different laser source with different optical power at a bias voltage of +200mV.34

Figure 2.1. (a) SEM image and (b) height profile of a typical Cu_{1.1}S /Cu4APc film determined by atomic force microscopy (see **Figure S2.3b** for the original image). (c) UV-ViS-NIR absorption spectra of as-prepared Cu_{1.1}S superlattice before and after ligand exchange (orange and dark red curves, respectively). (d) Raman spectra of as-prepared Cu_{1.1}S nanocrystal thin films before and after ligand exchange (same color code as in (c)). The inset highlights the spectral regime around the S-S stretching bands. 41

Figure 2. 2(a) GISAXS patterns of self-assembled Cu_{1.1}S NDs coated with OA. (b) GISAXS pattern of Cu4APc ligand induced assembly Cu_{1.1}S NDs. Both patterns show long-range highly ordered 2D hexagonal superlattices. (c) The extracted line profiles from the corresponding GISAXS images along in-plane wave vector q_y. To improve the statistics of the line profiles the signals were integrated along the q_z direction. (d) X-ray reflectivity profile of Cu_{1.1}S /Cu4APc film.42

Figure 2. 3(a) Temperature-dependent electrical conductivity measurement of Cu_{1.1}S nanocrystal films from 30 to 320 K. Red circles: OLM-capped Cu_{1.1}S NC films and blue circles: Cu_{1.1}S NC films crosslinked with Cu4APc. Inset: linear plot of the Cu4APc-capped Cu_{1.1}S film for better visualization. (b) Ln σ vs. T^{-1/x} for x =1-4 as assigned by the color legend for Cu_{1.1}S NC films crosslinked with Cu4APc. Dashed lines are linear fits for a fixed temperature window of 30 – 120 K. (c) Derivative d(log σ)/d(log T) vs. log T for the same dataset as in (b). Solid lines are linear fits for fixed temperature windows of 30 – 120 K and 120 – 210 K, respectively..44

Figure 2.4. (a) Transient vapor response traces of Cu_{1.1}S/Cu4APc film toward 100 to 5000 ppm of 4M2P at 0% relative humidity. (b) Responses of the Cu_{1.1}S/Cu4APc films to exposure with 5000 ppm 4M2P vapor, toluene vapor, water vapor, and 1-propanol vapor. (c) Response amplitudes plotted versus the gas-phase concentration of 4M2P and toluene. (d) Response amplitudes plotted versus the gas-phase concentration of 1-propanol and water. The solid lines are the Langmuir fits according to a 1st order adsorption model (i.e. equation 2.1) and the dashed lines are the Langmuir fits according to a 2nd order adsorption model (i.e. equation 2.2).46

Figure 3.1 TEM images of (a) 7.0 ± 0.8 nm $\text{Cu}_2\text{S}_y\text{Se}_{1-y}$ NCs and (b) 12.2 ± 1.9 nm Cu_2Se NCs. (c) EDX spectrum of the $\text{Cu}_2\text{S}_y\text{Se}_{1-y}$ NCs. (d) Raman spectra of as-prepared Cu_2Se and $\text{Cu}_2\text{Se}_y\text{S}_{1-y}$ nanocrystal thin films (orange curve and green curve, respectively). (e) Raman spectra of CuSeS nanocrystal thin films before and after ligand exchange (green curve and blue curve, respectively). 57

Figure 3.2 GISAXS patterns of self-assembled (a) $\text{Cu}_2\text{Se}/\text{OLm}$, (b) $\text{Cu}_2\text{Se}/\text{CoTAPc}$, (d) $\text{Cu}_2\text{Se}_y\text{S}_{1-y}/\text{OLm}$ and (e) $\text{Cu}_2\text{Se}_y\text{S}_{1-y}/\text{CoTAPc}$ films. (c) and (f) extracted line profiles from the corresponding GISAXS images on the left in (a)/(b) and (d)/(e), respectively, as a function of the in-plane scattering vector q_y . To improve the statistics of the line profiles, the ROI (white dotted box) was integrated along the q_z direction.59

Figure 3.3(a) Current-voltage (I - V) curves of $\text{Cu}_2\text{Se}_y\text{S}_{1-y}$ as well as $\text{Cu}_{2-x}\text{Se}_y\text{S}_{1-y}$ and (b) of Cu_2Se and Cu_{2-x}Se . (c) Corresponding optical absorption spectra of the ternary and (d) binary copper chalcogenides. The color code is the same in all four panels: green = Olm capping, reduced; yellow = Olm capping, oxidized; blue = CoTAPc capping, reduced; red = CoTAPc capping, oxidized.62

Figure 3.4(a) Temperature-dependent resistivity of $\text{Cu}_2\text{Se}_y\text{S}_{1-y}$ functionalized with CoTAPc. (b) Time-dependent current at 200 mV of a $\text{Cu}_2\text{Se}_y\text{S}_{1-y}/\text{CoTAPc}$ film during three excitation periods to 21 μW of 408 nm light (blue), 20 μW of 637 nm light (orange) and 21 μW of 848 nm (green).63

Figure 4.1a) GISAXS patterns of the NDs during self-assembly for a waiting period of (a) 5 min. and (b) 240 min. The white circles (transmitted) and red crosses (reflected) are the simulated diffraction patterns considering a hexagonal superlattice along the in-plane direction. (c) Temporal evolution of the lattice constants. (d) In-plane line profiles along $-q_y$ through the $\{10\}$ peak of the GISAXS patterns. 69

Figure 4.2 GISAXS patterns of the NDs during ligand exchange for a waiting period of (a) -42 min, (b) 6 min, (c) 24 min, and (d) 276 min. The red crosses and white circles are the simulated diffraction patterns considering a hexagonal superlattice along the in-plane direction. (e) In-plane line profiles along $-q_y$ through the $\{10\}$ peak of the GISAXS patterns. Peak intensities have been scaled up for clarity. (f) Temporal evolution of the lattice constants with elapsed time.71

Figure 4.3a) Raman spectra of Cu _{1.1} S nanodisc thin films before (blue) and after ligand exchange (red). b) Current-voltage (I-V) characteristics of Cu _{1.1} S ND films. Blue circles: Oleic-capped Cu _{1.1} S ND films and red circles: Cu _{1.1} S ND film after ligand exchange. The graph is plotted on a logarithmic scale for better comparison. Inset: photograph of a substrate with Au contacts for I-V measurements.....	72
Figure 5.1(a) Raman spectroscopy data after ligand exchange films. (b) Current-voltage (I-V) characteristics of PbS NC films: OA-capped (black); exchange film with CoTAPc (blue) and CuTAPc (green); the graph is plotted on a logarithmic scale for better comparison.	80
Figure 6.1 Schematically presentation of hybrid PbS-PAE-1 thin film fabrication. Individual steps are described in the continuous text.	82
Figure 6.2(a) Raman spectrum of a PbS-PPE-1 film, using a 1.96 eV laser. While the Oleic acid-capped PbS NCs do not exhibit any distinct Raman bands, after ligand exchange with PPE-1, the C-O as well as the phenyl-stretching bands of the polymer are clearly visible.....	83
Figure S2.1 Structural formula of Cu-4,4',4'',4''',4''''-tetraaminophthalocyanine (Cu4APc) with M = Cu.....	84
Figure S2.2 Ligand exchange at the liquid-air interface.	85
Figure S2.3 TEM image of Cu _{1.1} S nanodiscs of an average diameter of 12.7 ± 1.7 nm, and a thickness of 5.8 ± 0.7 nm. (b) AFM image of Cu _{1.1} S nanocrystal film after ligand exchange.	85
Figure S2.4(a) Current-voltage (I-V) curves of Cu _{1.1} S nanocrystal films prepared by interface method before and after ligand exchange (black and red curves, respectively). The curves were recorded under ambient conditions. (b) Plot of the total resistance vs. channel length Cu _{1.1} S nanocrystal film after ligand exchange with Cu4APc. The contact resistance is extracted by a linear fit to this data	86
Figure S2.5 Plot of the total resistance vs. channel length Cu _{1.1} S nanocrystal film after ligand exchange with Cu4APc. The contact resistance is extracted by a linear fit to this data.	87
Figure S2.6 a) Atomic force micrograph and b) extracted height profile of a thicker sample with 5-10 monolayers. c) I/V characteristics of a thick film at different contacts and channel lengths. The conductivity is 2-3 orders of magnitude smaller than in the monolayered films shown in the main body of the manuscript.	88

Figure S3.1 XRD pattern of as-synthesized $\text{Cu}_2\text{S}_y\text{Se}_{1-y}$ NCs. The reference structural data shows hexagonal Cu_2S (PDF card #: 84-0209). The reflections at 29° , 37° and 48° are absent in the cubic structure, and therefore characteristic for the hexagonal phase here.	90
Figure S3.2 AFM images and extracted height profile of $\text{Cu}_2\text{Se}_y\text{S}_{1-y}$ (top) and Cu_{2-x}Se (bottom).	91
Figure S3.3 FT-IR spectra of a) Cu_2Se and b) $\text{Cu}_2\text{Se}_y\text{S}_{1-y}$ NC films, both before and after ligand exchange with CoTAPc. Characteristic bands for oleylamine, which disappear during ligand exchange have been encircled in red. Note: Since CoTAPc also contains $-\text{NH}_2$ and $-\text{CH}$ vibrations, no quantitative description of the exchange efficiency can be made from this experiment.....	92
Figure S3.4 UV/VIS absorption spectrum of pure CoTAPc.....	93
Figure S3.5 Current/Voltage characteristics of a $\text{Cu}_{2-x}\text{Se}_y\text{S}_{1-y}/\text{CoTAPc}$ thin film at varying exposure times to air. The current was measured once the device was removed from the inert atmosphere of the glovebox and subsequently recorded from 5 minutes to 7 days.	94
Figure S3.6 Current–voltage characteristics of a $\text{Cu}_2\text{Se}/\text{Olm}$ film after a first oxidation in air (yellow), after treatment with $5\ \mu\text{L}$ of a $0.04\ \text{mmol/L}$ solution of $[\text{Cu}(\text{CH}_3\text{CN})_4]\text{PF}_6$ (blue), after treatment with $10\ \mu\text{L}$ of the same solution and after 15 min of oxidation in air.....	95
Figure S3.7 Current–voltage characteristics of a typical $\text{Cu}_{2-x}\text{Se}_y\text{S}_{1-y}/\text{Olm}$ film at different absorbed optical power values provided by a $408\ \text{nm}$ laser diode.	96
Figure S4.1 a) TEM image of Olm-passivated $\text{Cu}_{1.1}\text{S}$ NDs. b) Structural formula of CoTAPc.	99
Figure S4.2 a-f) GISAXS patterns from the self-assembly without ligand exchange at different intermediate times marked at the right corner of each images. The pink and red spots are the simulated diffraction peak position of bcc superlattice considering DWBA method.	100
Figure S4.3 GISAXS patterns from the self-assembly during ligand exchange process at different intermediate times marked at the right corner of each images. The pink and red spots are the simulated diffraction peak position of bcc superlattice considering DWBA method.	101
Figure S4.4 STEM image of $\text{Cu}_{1.1}\text{S}$ NC superlattice	102
Figure S4.5 Atomic force micrograph of the nanocrystal superlattice after complete ligand-exchange and drying on a silicon substrate. The average height of the superlattice is $\sim 11\ \text{nm}$	102

List of Publications

1. Electronically Coupled, Two-Dimensional Assembly of Cu_{1.1}S Nanodiscs for Selective Vapor Sensing Applications; Sonam Maiti, Santanu Maiti, Yvonne Joseph, Andreas Wolf, Wolfgang Brütting, Dirk Dorfs, Frank Schreiber, and Marcus Scheele *J. Phys. Chem. C* **2018**, 122, 23720–23727.
2. Dye-Sensitized Ternary Copper Chalcogenide Nanocrystals: Optoelectronic Properties, Air Stability and Photosensitivity; Sonam Maiti, Santanu Maiti, Ali H. Khan, Andreas Wolf, Dirk Dorfs, Ivan Moreels, Frank Schreiber and Marcus Scheele. *Chem. Mater.* **2019**, 31, 7, 2443-2449.
3. In situ formation of electronically coupled superlattices of Cu_{1.1}S Nanodiscs at the Liquid/Air Interface; Sonam Maiti, Santanu Maiti, Andre Maier, Rupak Banerjee, Chen Shen, Bridget M. Murphy, Marcus Scheele and Frank Schreiber. *Chem. Comm.* **2019**, 55, 4805-4808.
4. Understanding the formation of conductive mesocrystalline superlattices with cubic PbS nanocrystals at the liquid/air interface; S. Maiti, S. Maiti, A. Maier, J. Hagenlocher, A. Chumakov, F. Schreiber, and M. Scheele. *J. Phys. Chem. C* **2019**, 123, 1519–1526.
5. Correlated, Dual-Beam Optical Gating in Coupled Organic-Inorganic Nanostructures; K.M. Wurst, M. Bender, J. Lauth, S. Maiti, T. Chassé, A. Meixner, L. D. A. Siebbeles, U. H. F. Bunz, K. Braun, M. Scheele; *Angewandte Chemie*, **2018**, 130, 36.

Acknowledgments

On publication of this work, I would like to offer my gratitude to each and every individual who made this thesis possible.

First, I would like to express my gratitude to my thesis supervisor Prof. Dr. Frank Schreiber for providing the opportunity to study at the University of Tübingen as a PhD candidate, for his academic guidance, constant encouragement and financial support. The experience gained under his supervision paved my scientific way and will significantly influence my future career.

My sincere thanks to Dr. Marcus Scheele for supervising the experimental details. I am grateful for the freedom and encouragement he gave me during my candidature. The opportunities I had in his lab were exceptional. I want to gratefully thank for the scientific environment he provided, a greatly equipped laboratory and motivating discussions. His high integrity and dedication in scientific research has been of special value and inspiration for me.

Next the person without him this dissertation would not have been possible. My colleague/husband Santanu, his enthusiasm is very contagious. I'm very happy that he always succeeded to explain the difficult concepts of Physics with ease to me. He gave an important contribution to this thesis and doing experiments with him was a pure pleasure. He always had simple and creative tricks to execute X-ray scattering experiments. Thank you for supporting me at work and in life.

I am grateful to my many collaborators for their contributions and support. I would like to thank Dirk Dorfs, Yvonne Joseph, and Ivan Moreels for providing feedback for my manuscripts. I extend special thanks to Andreas and Ali for providing me with specially shaped particles and challenging me to think more deeply. Many thanks to Andrei for the measurement at the ESRF. Sincere thanks to Ms. Elke Nadler for spending long hours assisting me with SEM and EDAX analyses. I have also greatly benefited from facilities and staff support of Soft Matter group.

Next I would like to thank my labmates, research colleagues of Scheele's group for their support, enthusiasm and lively atmosphere in the laboratory. I wish to express my sincere thanks to the whole Soft Matter group for their kind help and support. I had a lot of fun in the group and learned a lot from you. I would also like to thank my office mates Jan, Santanu, and all the master's students came during my tenure in Soft Matter group, and Björn, Mishelle, and Kai from A4 for the fun time and the (non) scientific conversations. I would like to express my

heartiest thanks to Mahdi, Andre, Krishan, and Alex. I learned lot of small but smart experimental tricks from them which helped me afterwards.

I would like to thank Olga, Jan, Berthold and Madeline for their anonymous support and help. I gratefully acknowledge to Andre Maier who helped me to translate the English abstract of this dissertation to German language and Navid Hussain for very helpful proofreading of my thesis. Special thanks Hanna Maurer and Aleksandra Rötschke for their thoughtful assistance with administrative tasks and Ralph who always came up with prompt and smart solutions of technical problems with Raman Spectrometer.

I have made many friends at Uni Tübingen during my tenure and wish everyone best of luck for their research journey.

Finally, I would like to express my appreciation and love to my family, especially my parents, mother-in law and my brothers for their strong support, love, and understanding.

References

1. Trindade, T.; O'Brien, P.; Pickett, N. L., Nanocrystalline semiconductors: Synthesis, properties, and perspectives. *Chem Mater* **2001**, *13*, 3843-3858.
2. Bekenstein, Y.; Elimelech, O.; Vinokurov, K.; Millo, O.; Banin, U., Charge Transport in Cu₂S Nanocrystals Arrays: Effects of Crystallite Size and Ligand Length. *Z Phys Chem* **2015**, *229*, 179-190.
3. Deka, S.; Genovese, A.; Zhang, Y.; Miszta, K.; Bertoni, G.; Krahne, R.; Giannini, C.; Manna, L., Phosphine-Free Synthesis of p-Type Copper(I) Selenide Nanocrystals in Hot Coordinating Solvents. *J Am Chem Soc* **2010**, *132*, 8912.
4. Dong, A. G.; Ye, X. C.; Chen, J.; Murray, C. B., Two-Dimensional Binary and Ternary Nanocrystal Superlattices: The Case of Monolayers and Bilayers. *Nano Lett* **2011**, *11*, 1804-1809.
5. Hessel, C. M.; Pattani, V. P.; Rasch, M.; Panthani, M. G.; Koo, B.; Tunnell, J. W.; Korgel, B. A., Copper Selenide Nanocrystals for Photothermal Therapy. *Nano Lett* **2011**, *11*, 2560-2566.
6. Li, W. H.; Shavel, A.; Guzman, R.; Rubio-Garcia, J.; Flox, C.; Fan, J. D.; Cadavid, D.; Ibanez, M.; Arbiol, J.; Morante, J. R.; Cabot, A., Morphology evolution of Cu_{2-x}S nanoparticles: from spheres to dodecahedrons. *Chem Comm* **2011**, *47*, 10332-10334.
7. Paik, T.; Murray, C. B., Shape-Directed Binary Assembly of Anisotropic Nanoplates: A Nanocrystal Puzzle with Shape-Complementary Building Blocks. *Nano Lett* **2013**, *13*, 2952-2956.
8. Riha, S. C.; Johnson, D. C.; Prieto, A. L., Cu₂Se nanoparticles with tunable electronic properties due to a controlled solid-state phase transition driven by copper oxidation and cationic conduction. *J Am Chem Soc* **2011**, *133*, 1383-90.
9. Brus, L., Chemical approaches to semiconductor nanocrystals. *J Phys Chem Solids* **1998**, *59*, 459-465.
10. Murray, C. B.; Kagan, C. R.; Bawendi, M. G., Synthesis and characterization of monodisperse nanocrystals and close-packed nanocrystal assemblies. *Annu Rev Mater Sci* **2000**, *30*, 545-610.
11. Rao, C. N. R.; Müller, A.; Cheetham, A. K., *Nanomaterials chemistry : recent developments and new directions*. Wiley-VCH: Weinheim, 2007; 403.

12. Jones, W.; Rao, C. N. R., *Supramolecular organization and materials design*. Cambridge University Press: Cambridge ; New York, 2002; 446.
13. Lieber, C. M., Nanowires as building blocks for nanoelectronics and nanophotonics. *2003 Ieee International Electron Devices Meeting, Technical Digest* **2003**, 300-302.
14. Guo, Q.; Ford, G. M.; Hillhouse, H. W.; Agrawal, R., Sulfide Nanocrystal Inks for Dense Cu(In_{1-x}Ga_x)(S_{1-y}Se_y)₂ Absorber Films and Their Photovoltaic Performance. *Nano Lett* **2009**, *9*, 3060-3065.
15. Guo, Q. J.; Hillhouse, H. W.; Agrawal, R., Synthesis of Cu₂ZnSnS₄ Nanocrystal Ink and Its Use for Solar Cells. *J Am Chem Soc* **2009**, *131*, 11672.
16. Regulacio, M. D.; Han, M. Y., Composition-Tunable Alloyed Semiconductor Nanocrystals. *Acc Chem Res* **2010**, *43*, 621-630.
17. Yin, Y.; Alivisatos, A. P., Colloidal nanocrystal synthesis and the organic-inorganic interface. *Nature* **2005**, *437*, 664-670.
18. Alfassi, Z.; Bahnemann, D.; Henglein, A., Photochemistry of Colloidal Metal Sulfides .3. Photoelectron Emission from Cds and Cds-Zns Co-Colloids. *J Phys Chem* **1982**, *86*, 4656-4657.
19. Nozik, A. J., Photoelectrochemistry - Applications to Solar-Energy Conversion. *Annu Rev Phys Chem* **1978**, *29*, 189-222.
20. Bawendi, M. G.; Steigerwald, M. L.; Brus, L. E., The Quantum-Mechanics of Larger Semiconductor Clusters (Quantum Dots). *Annu Rev Phys Chem* **1990**, *41*, 477-496.
21. Brus, L. E., Electron Electron and Electron-Hole Interactions in Small Semiconductor Crystallites - the Size Dependence of the Lowest Excited Electronic State. *J Chem Phys* **1984**, *80*, 4403-4409.
22. Chestnoy, N.; Harris, T. D.; Hull, R.; Brus, L. E., Luminescence and Photophysics of Cds Semiconductor Clusters - the Nature of the Emitting Electronic State. *J Phys Chem-US* **1986**, *90*, 3393-3399.
23. Rossetti, R.; Nakahara, S.; Brus, L. E., Quantum Size Effects in the Redox Potentials, Resonance Raman-Spectra, and Electronic-Spectra of Cds Crystallites in Aqueous-Solution. *J Chem Phys* **1983**, *79*, 1086-1088.
24. Brus, L. E., A Simple-Model for the Ionization-Potential, Electron-Affinity, and Aqueous Redox Potentials of Small Semiconductor Crystallites. *J Chem Phys* **1983**, *79*, 5566-5571.
25. Kayanuma, Y., Wannier Exciton in Microcrystals. *Solid State Comm* **1986**, *59*, 405-408.

26. Steigerwald, M. L.; Brus, L. E., Semiconductor Crystallites - a Class of Large Molecules. *Acc Chem Res* **1990**, *23*, 183-188.
27. Shavel, A.; Arbiol, J.; Cabot, A., Synthesis of Quaternary Chalcogenide Nanocrystals: Stannite $\text{Cu}_2\text{Zn}_x\text{Sn}_y\text{Se}_{1+x+2y}$. *J Am Chem Soc* **2010**, *132*, 4514.
28. Wang, J. J.; Xue, D. J.; Guo, Y. G.; Hu, J. S.; Wan, L. J., Bandgap engineering of monodispersed $\text{Cu}_{2-x}\text{S}(y)\text{Se}_{1-y}$ nanocrystals through chalcogen ratio and crystal structure. *J Am Chem Soc* **2011**, *133*, 18558-61.
29. Coughlan, C.; Ibanez, M.; Dobrozhan, O.; Singh, A.; Cabot, A.; Ryan, K. M., Compound Copper Chalcogenide Nanocrystals. *Chem Rev* **2017**, *117*, 5865-6109.
30. Liu, Y.; Dong, Q.; Wei, H.; Ning, Y.; Sun, H.; Tian, W.; Zhang, H.; Yang, B., Synthesis of Cu_{2-x}Se Nanocrystals by Tuning the Reactivity of Se. *J Phys Chem C* **2011**, *115*, 9909-9916.
31. Kriegel, I.; Jiang, C.; Rodriguez-Fernandez, J.; Schaller, R. D.; Talapin, D. V.; da Como, E.; Feldmann, J., Tuning the excitonic and plasmonic properties of copper chalcogenide nanocrystals. *J Am Chem Soc* **2012**, *134*, 1583-90.
32. Zhao, Y. X.; Pan, H. C.; Lou, Y. B.; Qiu, X. F.; Zhu, J. J.; Burda, C., Plasmonic Cu_{2-x}S Nanocrystals: Optical and Structural Properties of Copper-Deficient Copper(I) Sulfides. *J Am Chem Soc* **2009**, *131*, 4253-4261.
33. Zhang, Y. B.; Wang, Y. W.; Zhang, J. W.; Xi, L. L.; Zhang, P. H.; Zhang, W. Q., Pinning down high-performance Cu-chalcogenides as thin-film solar cell absorbers: A successive screening approach. *J Chem Phys* **2016**, *144*, 19.
34. Maiti, S.; Maiti, S.; Joseph, Y.; Wolf, A.; Brütting, W.; Dorfs, D.; Schreiber, F.; Scheele, M., Electronically Coupled, Two-Dimensional Assembly of $\text{Cu}_{1.1}\text{S}$ Nanodiscs for Selective Vapor Sensing Applications. *J Phys Chem C* **2018**, *122*, 23720-23727.
35. Chung, J. S.; Sohn, H. J., Electrochemical behaviors of CuS as a cathode material for lithium secondary batteries. *J Power Sources* **2002**, *108*, 226-231.
36. Xie, Y.; Riedinger, A.; Prato, M.; Casu, A.; Genovese, A.; Guardia, P.; Sottini, S.; Sangregorio, C.; Miszta, K.; Ghosh, S.; Pellegrino, T.; Manna, L., Copper sulfide nanocrystals with tunable composition by reduction of covellite nanocrystals with Cu^+ ions. *J Am Chem Soc* **2013**, *135*, 17630-7.
37. Sun, S. D.; Li, P. J.; Liang, S. H.; Yang, Z. M., Diversified copper sulfide (Cu_{2-x}S) micro-/nanostructures: a comprehensive review on synthesis, modifications and applications. *Nanoscale* **2017**, *9*, 11357-11404.

38. Zhu, D.; Tang, A.; Kong, Q.; Zeng, B.; Yang, C.; Teng, F., Roles of Sulfur Sources in the Formation of Alloyed $\text{Cu}_{2-x}\text{S}_y\text{Se}_{1-y}$ Nanocrystals: Controllable Synthesis and Tuning of Plasmonic Resonance Absorption. *J Phys Chem C* **2017**, *121*, 15922-15930.
39. Xu, J.; Yang, X.; Yang, Q. D.; Huang, X.; Tang, Y.; Zhang, W.; Lee, C. S., Controllable Synthesis of Bandgap-Tunable $\text{CuS}_x\text{Se}_{(1-x)}$ Nanoplate Alloys. *Chem Asian J* **2015**, *10*, 1490-1495.
40. Xu, J.; Tang, Y.-B.; Chen, X.; Luan, C.-Y.; Zhang, W.-F.; Zapien, J. A.; Zhang, W.-J.; Kwong, H.-L.; Meng, X.-M.; Lee, S.-T.; Lee, C.-S., Synthesis of Homogeneously Alloyed $\text{Cu}_{2-x}(\text{S}_y\text{Se}_{1-y})$ Nanowire Bundles with Tunable Compositions and Bandgaps. *Adv Func Mater* **2010**, *20*, 4190-4195.
41. Kou, H.; Jiang, Y.; Li, J.; Yu, S.; Wang, C., Enhanced photoelectric performance of Cu_{2-x}Se nanostructure by doping with In^{3+} . *J Mater Chem* **2012**, *22*, 1950-1956.
42. Lee, J.; Yang, J.; Park, C.; Kim, J. H.; Kang, M. S., Electronic Properties of Cu_{2-x}Se Nanocrystal Thin Films Treated with Short Ligand (S^{2-} , SCN^- , and Cl^-) Solutions. *J Phys Chem C* **2016**, *120*, 14899-14905.
43. Otelaja, O. O.; Ha, D. H.; Ly, T.; Zhang, H.; Robinson, R. D., Highly conductive Cu_{2-x}S nanoparticle films through room-temperature processing and an order of magnitude enhancement of conductivity via electrophoretic deposition. *ACS Appl Mater Interfaces* **2014**, *6*, 18911-20.
44. Wang, X.; Ke, Y.; Pan, H.; Ma, K.; Xiao, Q.; Yin, D.; Wu, G.; Swihart, M. T., Cu-Deficient Plasmonic Cu_{2-x}S Nanoplate Electrocatalysts for Oxygen Reduction. *ACS Catalysis* **2015**, *5*, 2534-2540.
45. Dorfs, D.; Hartling, T.; Miszta, K.; Bigall, N. C.; Kim, M. R.; Genovese, A.; Falqui, A.; Povia, M.; Manna, L., Reversible tunability of the near-infrared valence band plasmon resonance in $\text{Cu}(2-x)\text{Se}$ nanocrystals. *J Am Chem Soc* **2011**, *133*, 11175-11180.
46. Luther, J. M.; Jain, P. K.; Ewers, T.; Alivisatos, A. P., Localized surface plasmon resonances arising from free carriers in doped quantum dots. *Nat Mater* **2011**, *10*, 361-366.
47. Dilena, E.; Dorfs, D.; George, C.; Miszta, K.; Povia, M.; Genovese, A.; Casu, A.; Prato, M.; Manna, L., Colloidal $\text{Cu}_{2-x}(\text{S}_y\text{Se}_{1-y})$ alloy nanocrystals with controllable crystal phase: synthesis, plasmonic properties, cation exchange and electrochemical lithiation. *J Mater Chem* **2012**, *22*, 26.
48. Saldanha, P. L.; Brescia, R.; Prato, M.; Li, H.; Povia, M.; Manna, L.; Lesnyak, V., Generalized One-Pot Synthesis of Copper Sulfide, Selenide-Sulfide, and Telluride-Sulfide Nanoparticles. *Chem Mater* **2014**, *26*, 1442-1449.

49. Xu, J.; Yang, X.; Yang, Q.; Zhang, W.; Lee, C. S., Phase conversion from hexagonal CuS(y)Se(1-y) to cubic Cu(2-x)S(y)Se(1-y): composition variation, morphology evolution, optical tuning, and solar cell applications. *ACS Appl Mater Interfaces* **2014**, *6*, 16352-9.
50. Lai, C.-H.; Huang, K.-W.; Cheng, J.-H.; Lee, C.-Y.; Hwang, B.-J.; Chen, L.-J., Direct growth of high-rate capability and high capacity copper sulfide nanowire array cathodes for lithium-ion batteries. *J Mater Chem* **2010**, *20*, 6638-6645.
51. Scheele, M.; Hanifi, D.; Zhrebetsky, D.; Chourou, S. T.; Axnanda, S.; Rancatore, B. J.; Thorkelsson, K.; Xu, T.; Liu, Z.; Wang, L. W.; Liu, Y.; Alivisatos, A. P., PbS Nanoparticles Capped with Tetrathiafulvalenetetracarboxylate: Utilizing Energy Level Alignment for Efficient Carrier Transport. *Acs Nano* **2014**, *8*, 2532-2540.
52. Scheele, M.; Brutting, W.; Schreiber, F., Coupled organic-inorganic nanostructures (COIN). *Phys Chem Chem Phys* **2015**, *17*, 97-111.
53. Maiti, S.; Andre, A.; Banerjee, R.; Hagenlocher, J.; Konovalov, O.; Schreiber, F.; Scheele, M., Monitoring Self-Assembly and Ligand Exchange of PbS Nanocrystal Superlattices at the Liquid/Air Interface in Real Time. *J Phys Chem Lett* **2018**, *9*, 739-744.
54. Maiti, S.; Maiti, S.; Maier, A.; Hagenlocher, J.; Chumakov, A.; Schreiber, F.; Scheele, M., Understanding the Formation of Conductive Mesocrystalline Superlattices with Cubic PbS Nanocrystals at the Liquid/Air Interface. *J Phys Chem C* **2018**, *123*, 1519-1526.
55. Andre, A.; Theurer, C.; Lauth, J.; Maiti, S.; Hodas, M.; Khoshkhoo, M. S.; Kinge, S.; Meixner, A. J.; Schreiber, F.; Siebbeles, L. D. A.; Braun, K.; Scheele, M., Structure, transport and photoconductance of PbS quantum dot monolayers functionalized with a copper phthalocyanine derivative. *Chem Commun* **2017**, *53*, 1700-1703.
56. Boker, A.; He, J.; Emrick, T.; Russell, T. P., Self-assembly of nanoparticles at interfaces. *Soft Matter* **2007**, *3*, 1231-1248.
57. Diroll, B. T.; Greybush, N. J.; Kagan, C. R.; Murray, C. B., Smectic Nanorod Superlattices Assembled on Liquid Subphases: Structure, Orientation, Defects, and Optical Polarization. *Chem Mater* **2015**, *27*, 2998-3008.
58. Dong, A. G.; Chen, J.; Vora, P. M.; Kikkawa, J. M.; Murray, C. B., Binary nanocrystal superlattice membranes self-assembled at the liquid-air interface. *Nature* **2010**, *466*, 474-477.
59. Boles, M. A.; Engel, M.; Talapin, D. V., Self-Assembly of Colloidal Nanocrystals: From Intricate Structures to Functional Materials. *Chem Rev* **2016**, *116*, 11220-11289.
60. Talapin, D. V.; Lee, J. S.; Kovalenko, M. V.; Shevchenko, E. V., Prospects of colloidal nanocrystals for electronic and optoelectronic applications. *Chem Rev* **2010**, *110*, 389-458.

61. Evers, W. H.; De Nijs, B.; Filion, L.; Castillo, S.; Dijkstra, M.; Vanmaekelbergh, D., Entropy-driven formation of binary semiconductor-nanocrystal superlattices. *Nano Lett* **2010**, *10*, 4235-4241.
62. Pickering, S. U. CXCVI.-Emulsions. *J. Chem. Soc., Trans.* **1907**, *91*, 2001.
63. Rogach, A. L.; Gaponik, N.; Lupton, J. M.; Bertoni, C.; Gallardo, D. E.; Dunn, S.; Pira, N. L.; Paderi, M.; Repetto, P.; Romanov, S. G.; O'Dwyer, C.; Torres, C. M. S.; Eychmuller, A., Light-emitting diodes with semiconductor nanocrystals. *Angew Chem* **2008**, *47*, 6538-6549.
64. Ye, X.; Millan, J. A.; Engel, M.; Chen, J.; Diroll, B. T.; Glotzer, S. C.; Murray, C. B., Shape alloys of nanorods and nanospheres from self-assembly. *Nano Lett* **2013**, *13*, 4980-8.
65. Paik, T.; Murray, C. B., Shape-directed binary assembly of anisotropic nanoplates: a nanocrystal puzzle with shape-complementary building blocks. *Nano Lett* **2013**, *13*, 2952-2956.
66. Dong, A.; Ye, X.; Chen, J.; Murray, C. B., Two-dimensional binary and ternary nanocrystal superlattices: the case of monolayers and bilayers. *Nano Lett* **2011**, *11*, 1804-1809.
67. Talapin, D. V.; Shevchenko, E. V.; Bodnarchuk, M. I.; Ye, X.; Chen, J.; Murray, C. B., Quasicrystalline order in self-assembled binary nanoparticle superlattices. *Nature* **2009**, *461*, 964-967.
68. Dong, A.; Chen, J.; Vora, P. M.; Kikkawa, J. M.; Murray, C. B., Binary nanocrystal superlattice membranes self-assembled at the liquid-air interface. *Nature* **2010**, *466*, 474-477.
69. Min, Y.; Akbulut, M.; Kristiansen, K.; Golan, Y.; Israelachvili, J., The role of interparticle and external forces in nanoparticle assembly. *Nat Mater* **2008**, *7*, 527-38.
70. Talapin, D. V.; Lee, J. S.; Kovalenko, M. V.; Shevchenko, E. V., Prospects of Colloidal Nanocrystals for Electronic and Optoelectronic Applications. *Chem Rev* **2010**, *110*, 389-458.
71. Li, X. M.; Shen, H. B.; Niu, J. Z.; Zhang, Y. G.; Wang, H. Z.; Li, L. S., Columnar Self-Assembly of Cu₂S Hexagonal Nanoplates Induced by Tin(IV)-X Complex as Inorganic Surface Ligand. *J Am Chem Soc* **2010**, *132*, 12778-12779.
72. Shen, H. B.; Niu, J. Z.; Li, X. M.; Wang, H. Z.; Xing, M.; Chen, X.; Li, L. S., Fabrication of "strong" columnar Cu_{2-x}Se superstructures assisted by inorganic ligands. *Nanoscale* **2012**, *4*, 2741-2747.

73. Dong, A. G.; Jiao, Y. C.; Milliron, D. J., Electronically Coupled Nanocrystal Superlattice Films by in Situ Ligand Exchange at the Liquid-Air Interface. *Acs Nano* **2013**, *7*, 10978-10984.
74. Murray, C. B.; Kagan, C. R.; Bawendi, M. G., Self-Organization of Cdse Nanocrystallites into 3-Dimensional Quantum-Dot Superlattices. *Science* **1995**, *270*, 1335-1338.
75. Shevchenko, E. V.; Kortright, J. B.; Talapin, D. V.; Aloni, S.; Alivisatos, A. P., Quasi-ternary nanoparticle superlattices through nanoparticle design. *Advanced Materials* **2007**, *19*, 4183.
76. Shevchenko, E. V.; Talapin, D. V.; Kotov, N. A.; O'Brien, S.; Murray, C. B., Structural diversity in binary nanoparticle superlattices. *Nature* **2006**, *439*, 55-59.
77. Beverly, K. C.; Sample, J. L.; Sampaio, J. F.; Remacle, F.; Heath, J. R.; Levine, R. D., Quantum dot artificial solids: Understanding the static and dynamic role of size and packing disorder. *P Natl Acad Sci USA* **2002**, *99*, 6456-6459.
78. Choi, J.; Kang, N.; Yang, H. Y.; Kim, H. J.; Son, S. U., Colloidal Synthesis of Cubic-Phase Copper Selenide Nanodiscs and Their Optoelectronic Properties. *Chem Mater* **2010**, *22*, 3586-3588.
79. Mott, N. F., *Conduction in non-crystalline materials*. 2nd ed.; Clarendon Press ; Oxford University Press: Oxford, Oxford ; New York, 1993; 150.
80. Shklovskii, B. I.; Éfros, A. L., *Electronic properties of doped semiconductors*. Springer-Verlag: Berlin ; New York, 1984; 388.
81. Zabet-Khosousi, A.; Dhirani, A. A., Charge transport in nanoparticle assemblies. *Chem Rev* **2008**, *108*, 4072-4124.
82. Houtepen, A. J.; Kockmann, D.; Vanmaekelbergh, D., Reappraisal of Variable-Range Hopping in Quantum-Dot Solids. *Nano Lett* **2008**, *8*, 3516-3520.
83. Tran, T. B.; Beloborodov, I. S.; Lin, X. M.; Bigioni, T. P.; Vinokur, V. M.; Jaeger, H. M., Multiple cotunneling in large quantum dot arrays. *Phys Rev Lett* **2005**, *95*, 7.
84. Zabet-Khosousi, A.; Dhirani, A. A., Charge transport in nanoparticle assemblies. *Chem Rev* **2008**, *108*, 4072-124.
85. Wehrenberg, B. L.; Yu, D.; Ma, J. S.; Guyot-Sionnest, P., Conduction in charged PbSe nanocrystal films. *J Phys Chem B* **2005**, *109*, 20192-20199.
86. Yu, D.; Wang, C. J.; Wehrenberg, B. L.; Guyot-Sionnest, P., Variable range hopping conduction in semiconductor nanocrystal solids. *Phys Rev Lett* **2004**, *92*, 21.

87. Talapin, D. V.; Murray, C. B., PbSe nanocrystal solids for n- and p-channel thin film field-effect transistors. *Science* **2005**, *310*, 86-89.
88. Mentzel, T. S.; Porter, V. J.; Geyer, S.; MacLean, K.; Bawendi, M. G.; Kastner, M. A., Charge transport in PbSe nanocrystal arrays. *Phys Rev B* **2008**, *77*, 7.
89. Otelaja, O. O.; Ha, D. H.; Ly, T.; Zhang, H. T.; Robinson, R. D., Highly Conductive Cu_{2-x}S Nanoparticle Films through Room-Temperature Processing and an Order of Magnitude Enhancement of Conductivity via Electrophoretic Deposition. *Acs Appl Mater Inter* **2014**, *6*, 18911-18920.
90. Shabaev, A.; Efros, A. L.; Efros, A. L., Dark and photo-conductivity in ordered array of nanocrystals. *Nano Lett* **2013**, *13*, 5454-61.
91. Vogel, N.; Retsch, M.; Fustin, C.-A.; del Campo, A.; Jonas, U., Advances in Colloidal Assembly: The Design of Structure and Hierarchy in Two and Three Dimensions. *Chem Rev* **2015**, *115*, 6265-6311.
92. Wohltjen, H.; Snow, A. W., Colloidal Metal-Insulator-Metal Ensemble Chemiresistor Sensor. *Anal Chem* **1998**, *70*, 2856-2859.
93. Zhang, J.; Qin, Z.; Zeng, D.; Xie, C., Metal-Oxide-Semiconductor Based Gas Sensors: Screening, Preparation, and Integration. *Phys Chem Chem Phys* **2017**, *19*, 6313-6329.
94. Potyrailo, R. A., Toward High Value Sensing: Monolayer-Protected Metal Nanoparticles in Multivariable Gas and Vapor Sensors. *Chem Soc Rev* **2017**, *46*, 5311-5346.
95. Potyrailo, R. A., Multivariable Sensors for Ubiquitous Monitoring of Gases in the Era of Internet of Things and Industrial Internet. *Chem Rev* **2016**, *116*, 11877-11923.
96. Saha, K.; Agasti, S. S.; Kim, C.; Li, X.; Rotello, V. M., Gold Nanoparticles in Chemical and Biological Sensing. *Chem Rev* **2012**, *112*, 2739-2779.
97. Calderón, M. F.; Zelaya, E.; Benitez, G. A.; Schilardi, P. L.; Creus, A. H.; Orive, A. G.; Salvarezza, R. C.; Ibañez, F. J., New Findings for the Composition and Structure of Ni Nanoparticles Protected with Organomercaptan Molecules. *Langmuir* **2013**, *29*, 4670-4678.
98. Dalfovo, M. C.; Salvarezza, R. C.; Ibañez, F. J., Improved Vapor Selectivity and Stability of Localized Surface Plasmon Resonance with a Surfactant-Coated Au Nanoparticles Film. *Analytical Chemistry* **2012**, *84*, 4886-4892.
99. Moreno, M.; Ibañez, F. J.; Jasinski, J. B.; Zamborini, F. P., Hydrogen Reactivity of Palladium Nanoparticles Coated with Mixed Monolayers of Alkyl Thiols and Alkyl Amines for Sensing and Catalysis Applications. *J Am Chem Soc* **2011**, *133*, 4389-4397.

100. Dovgolevsky, E.; Konvalina, G.; Tisch, U.; Haick, H., Monolayer-Capped Cubic Platinum Nanoparticles for Sensing Nonpolar Analytes in Highly Humid Atmospheres. *J Phys Chem C* **2010**, *114*, 14042-14049.
101. Drake, C.; Deshpande, S.; Bera, D.; Seal, S., Metallic Nanostructured Materials Based Sensors. *Int Mater Rev* **2007**, *52*, 289-317.
102. Franke, M. E.; Koplin, T. J.; Simon, U., Metal and Metal Oxide Nanoparticles in Chemiresistors: Does the Nanoscale Matter? *Small* **2006**, *2*, 36-50.
103. Joseph, Y.; Peić, A.; Chen, X.; Michl, J.; Vossmeier, T.; Yasuda, A., Vapor Sensitivity of Networked Gold Nanoparticle Chemiresistors: Importance of Flexibility and Resistivity of the Interlinkage. *J Phys Chem C* **2007**, *111*, 12855-12859.
104. Huang, X.; Tan, C. L.; Yin, Z. Y.; Zhang, H., 25th Anniversary Article: Hybrid Nanostructures Based on Two-Dimensional Nanomaterials. *Adv Mater* **2014**, *26*, 2185-2204.
105. Nasilowski, M.; Mahler, B.; Lhuillier, E.; Ithurria, S.; Dubertret, B., Two-Dimensional Colloidal Nanocrystals. *Chem Rev* **2016**, *116*, 10934-10982.
106. Zhao, Y. X.; Burda, C., Development of plasmonic semiconductor nanomaterials with copper chalcogenides for a future with sustainable energy materials. *Energ Environ Sci* **2012**, *5*, 5564-5576.
107. Wang, Q. H.; Kalantar-Zadeh, K.; Kis, A.; Coleman, J. N.; Strano, M. S., Electronics and optoelectronics of two-dimensional transition metal dichalcogenides. *Nat Nanotechnol* **2012**, *7*, 699-712.
108. Maiti, S.; Sanyal, M. K.; Varghese, N.; Satpati, B.; Dasgupta, D.; Daillant, J.; Carriere, D.; Konovolov, O.; Rao, C. N. R., Formation of single-crystalline CuS at the organic-aqueous interface. *J Phys-Condens Mat* **2013**, *25*, 39.
109. Kelly, A. G.; Hallam, T.; Backes, C.; Harvey, A.; Esmaily, A. S.; Godwin, I.; Coelho, J.; Nicolosi, V.; Lauth, J.; Kulkarni, A.; Kinge, S.; Siebbeles, L. D. A.; Duesberg, G. S.; Coleman, J. N., All-printed thin-film transistors from networks of liquid-exfoliated nanosheets. *Science* **2017**, *356*, 69-72.
110. Aggarwal, M.; Khan, S.; Husain, M.; Ming, T. C.; Tsai, M. Y.; Perng, T. P.; Khan, Z. H., Variable-range hopping in Fe₇₀Pt₃₀ catalyzed multi-walled carbon nanotubes film. *Eur Phys J B* **2007**, *60*, 319-324.
111. Efros, A. L.; Shklovskii, B. I., Coulomb Gap and Low-Temperature Conductivity of Disordered Systems. *J Phys C Solid State* **1975**, *8*, L49-L51.

112. Khondaker, S. I.; Shlimak, I. S.; Nicholls, J. T.; Pepper, M.; Ritchie, D. A., Two-dimensional hopping conductivity in a delta-doped GaAs/Al_xGa_{1-x}As heterostructure. *Phys Rev B* **1999**, *59*, 4580-4583.
113. Joung, D.; Khondaker, S. I., Efros-Shklovskii variable-range hopping in reduced graphene oxide sheets of varying carbon sp² fraction. *Phys Rev B* **2012**, *86*, 23.
114. Khoshkhoo, M. S.; Maiti, S.; Schreiber, F.; Chasse, T.; Scheele, M., Surface Functionalization with Copper Tetraaminophthalocyanine Enables Efficient Charge Transport in Indium Tin Oxide Nanocrystal Thin Films. *Acs Appl Mater Inter* **2017**, *9*, 14197-14206.
115. van der Stam, W.; Gudjonsdottir, S.; Evers, W. H.; Houtepen, A. J., Switching between Plasmonic and Fluorescent Copper Sulfide Nanocrystals. *J Am Chem Soc* **2017**, *139*, 13208-13217.
116. Vinokurov, K.; Elimelech, O.; Millo, O.; Banin, U., Copper Sulfide Nanocrystal Level Structure and Electrochemical Functionality towards Sensing Applications. *Chemphyschem* **2016**, *17*, 675-680.
117. Brewer, A. S.; Arnold, M. S., Field-effect measurements of mobility and carrier concentration of Cu₂S colloidal quantum dot thin films after ligand exchange. *Thin Solid Films* **2014**, *567*, 91-95.
118. Aigner, W.; Nenova, G. K.; Sliem, M. A.; Fischer, R. A.; Stutzmann, M.; Pereira, R. N., Electronic Changes Induced by Surface Modification of Cu_{2-x}S Nanocrystals. *J Phys Chem C* **2015**, *119* (28), 16276-16285.
119. Bekenstein, Y.; Vinokurov, K.; Keren-Zur, S.; Hadar, I.; Schilt, Y.; Raviv, U.; Millo, O.; Banin, U., Thermal Doping by Vacancy Formation in Copper Sulfide Nanocrystal Arrays. *Nano Lett* **2014**, *14*, 1349-1353.
120. Jung, S. H.; Choi, J. H.; Yang, S. M.; Cho, W. J.; Ha, C. S., Syntheses and characterization of soluble phthalocyanine derivatives for organic electroluminescent devices. *Mat Sci Eng B-Solid* **2001**, *85*, 160-164.
121. Sharma, R.; Sawvel, A. M.; Barton, B.; Dong, A. G.; Buonsanti, R.; Llordes, A.; Schaible, E.; Axnanda, S.; Liu, Z.; Urban, J. J.; Nordlund, D.; Kisielowski, C.; Milliron, D. J., Nanocrystal Superlattice Embedded within an Inorganic Semiconducting Matrix by in Situ Ligand Exchange: Fabrication and Morphology. *Chem Mater* **2015**, *27*, 2755-2758.
122. Joseph, Y.; Guse, B.; Vossmeier, T.; Yasuda, A., Gold nanoparticle/organic networks as chemiresistor coatings: The effect of film morphology on vapor sensitivity. *J Phys Chem C* **2008**, *112*, 12507-12514.

123. Wolf, A.; Kodanek, T.; Dorfs, D., Tuning the LSPR in copper chalcogenide nanoparticles by cation intercalation, cation exchange and metal growth. *Nanoscale* **2015**, *7*, 19519-19527.
124. Gu, F.; Xu, G. Q.; Ang, S. G., Fabrication of CuTAPc polymer nanowires and nanotubes by electropolymerization. *Nanotechnology* **2008**, *19*, 14.
125. Kumar, P.; Nagarajan, R., An Elegant Room Temperature Procedure for the Precise Control of Composition in the Cu-S System. *Inorg Chem* **2011**, *50*, 9204-9206.
126. Surovtsev, N. V.; Adichtchev, S. V.; Duda, T. A.; Pokrovsky, L. D.; Sveshnikova, L. L., New Surface-Enhanced Raman Scattering Active Substrate Fabricated by Use of the Langmuir-Blodgett Technique. *J Phys Chem C* **2010**, *114*, 4803-4807.
127. Renaud, G.; Lazzari, R.; Leroy, F., Probing surface and interface morphology with Grazing Incidence Small Angle X-Ray Scattering. *Surf Sci Rep* **2009**, *64*, 255-380.
128. Maiti, S.; Sanyal, M. K.; Jana, M. K.; Runge, B.; Murphy, B. M.; Biswas, K.; Rao, C. N. R., Evidence of contact epitaxy in the self-assembly of HgSe nanocrystals formed at a liquid-liquid interface. *J Phys-Condens Mat* **2017**, *29*, 9.
129. Ren, B.; Wang, L.; Huang, J.; Tang, K.; Yang, Y. M.; Wang, L. J., Metal-semiconductor transition in CuS-Cu_{1.8}S mixed phase thin films. *Vacuum* **2015**, *112*, 70-72.
130. Liu, H.; Pourret, A.; Guyot-Sionnest, P., Mott and Efros-Shklovskii Variable Range Hopping in CdSe Quantum Dots Films. *Acs Nano* **2010**, *4*, 5211-5216.
131. Gainov, R. R.; Dooglav, A. V.; Pen'kov, I. N.; Mukhamedshin, I. R.; Mozgova, N. N.; Evlampiev, I. A.; Bryzgalov, I. A., Phase transition and anomalous electronic behavior in the layered superconductor CuS probed by NQR. *Phys Rev B* **2009**, *79*, 7.
132. Jain, P. K.; Huang, W. Y.; El-Sayed, M. A., On the universal scaling behavior of the distance decay of plasmon coupling in metal nanoparticle pairs: A plasmon ruler equation. *Nano Lett* **2007**, *7*, 2080-2088.
133. Wei, H. M.; Grundmann, M.; Lorenz, M., Confinement-driven metal-insulator transition and polarity-controlled conductivity of epitaxial LaNiO₃/LaAlO₃ (111) superlattices. *Appl Phys Lett* **2016**, *109*, 8.
134. Joseph, Y.; Guse, B.; Yasuda, A.; Vossmeier, T., Chemiresistor coatings from Pt- and Au-nanoparticle/nonanedithiol films: sensitivity to gases and solvent vapors. *Sensor Actuat B-Chem* **2004**, *98*, 188-195.
135. Olichwer, N.; Meyer, A.; Yesilmen, M.; Vossmeier, T., Gold nanoparticle superlattices: correlating chemiresistive responses with analyte sorption and swelling. *J Mater Chem C* **2016**, *4*, 8214-8225.

136. Belghachi, A.; Collins, R. A., Humidity Response of Phthalocyanine Gas Sensors. *J Phys D Appl Phys* **1988**, *21*, 1647-1651.
137. Hassinen, A.; Moreels, I.; De Nolf, K.; Smet, P. F.; Martins, J. C.; Hens, Z., Short-Chain Alcohols Strip X-Type Ligands and Quench the Luminescence of PbSe and CdSe Quantum Dots, Acetonitrile Does Not. *J Am Chem Soc* **2012**, *134*, 20705-20712.
138. Garcia-Berrios, E.; Gao, T.; Woodka, M. D.; Maldonado, S.; Brunshwig, B. S.; Ellsworth, M. W.; Lewis, N. S., Response versus Chain Length of Alkanethiol-Capped Au Nanoparticle Chemiresistive Chemical Vapor Sensors. *J Phys Chem C* **2010**, *114*, 21914-21920.
139. Fu, K.; Li, S. H.; Jiang, X. Q.; Wang, Y.; Willis, B. G., DNA Gold Nanoparticle Nanocomposite Films for Chemiresistive Vapor Sensing. *Langmuir* **2013**, *29*, 14335-14343.
140. Hubble, L. J.; Cooper, J. S.; Sosa-Pintos, A.; Kiiveri, H.; Chow, E.; Webster, M. S.; Wiczorek, L.; Raguse, B., High-Throughput Fabrication and Screening Improves Gold Nanoparticle Chemiresistor Sensor Performance. *Acs Comb Sci* **2015**, *17*, 120-129.
141. Rigoni, F.; Drera, G.; Pagliara, S.; Pergem, E.; Pintossi, C.; Goldoni, A.; Sangaletti, L., Gas sensing at the nanoscale: engineering SWCNT-ITO nano-heterojunctions for the selective detection of NH₃ and NO₂ target molecules. *Nanotechnology* **2017**, *28*, 3.
142. Khoshkhoo, M. S.; Joseph, Y.; Maiti, S.; Schreiber, F.; Chasse, T.; Scheele, M., Tunable Charge Transport in Hybrid Superlattices of Indium Tin Oxide Nanocrystals and Metal Phthalocyanines-Toward Sensing Applications. *Adv Mater Interfaces* **2018**, *5*, 9.
143. Lupan, O.; Postica, V.; Grottrup, J.; Mishra, A. K.; de Leeuw, N. H.; Carreira, J. F. C.; Rodrigues, J.; Ben Sedrine, N.; Correia, M. R.; Monteiro, T.; Cretu, V.; Tiginyanu, I.; Smazna, D.; Mishra, Y. K.; Adelung, R., Hybridization of Zinc Oxide Tetrapods for Selective Gas Sensing Applications. *Acs Appl Mater Inter* **2017**, *9*, 4084-4099.
144. Dovgolevsky, E.; Konvalina, G.; Tisch, U.; Haick, H., Mono layer-Capped Cubic Platinum Nanoparticles for Sensing Nonpolar Analytes in Highly Humid Atmospheres. *J Phys Chem C* **2010**, *114*, 14042-14049.
145. Wang, X. J.; Wang, W.; Liu, Y. L., Enhanced acetone sensing performance of Au nanoparticles functionalized flower-like ZnO. *Sensor Actuat B-Chem* **2012**, *168*, 39-45.
146. Lesnyak, V.; George, C.; Genovese, A.; Prato, M.; Casu, A.; Ayyappan, S.; Scarpellini, A.; Manna, L., Alloyed Copper Chalcogenide Nanoplatelets via Partial Cation Exchange Reactions. *Acs Nano* **2014**, *8*, 8407-8418.
147. Lynch, J.; Kotiuga, M.; Doan-Nguyen, V. V. T.; Queen, W. L.; Forster, J. D.; Schlitz, R. A.; Murray, C. B.; Neaton, J. B.; Chabynyc, M. L.; Urban, J. J., Ligand Coupling Symmetry

Correlates with Thermopower Enhancement in Small-Molecule/Nanocrystal Hybrid Materials. *Acs Nano* **2014**, *8*, 10528-10536.

148. Liu, L.; Zhou, B.; Deng, L.; Fu, W.; Zhang, J.; Wu, M.; Zhang, W.; Zou, B.; Zhong, H., Thermal Annealing Effects of Plasmonic Cu_{1.8}S Nanocrystal Films and Their Photovoltaic Properties. *J Phys Chem C* **2014**, *118*, 26964-26972.

149. Wang, F.; Li, Q.; Lin, L.; Peng, H.; Liu, Z.; Xu, D., Monodisperse Copper Chalcogenide Nanocrystals: Controllable Synthesis and the Pinning of Plasmonic Resonance Absorption. *J Am Chem Soc* **2015**, *137*, 12006-12.

150. Liu, S.; Zhang, Z.; Bao, J.; Lan, Y.; Tu, W.; Han, M.; Dai, Z., Controllable Synthesis of Tetragonal and Cubic Phase Cu₂Se Nanowires Assembled by Small Nanocubes and Their Electrocatalytic Performance for Oxygen Reduction Reaction. *J Phys Chem C* **2013**, *117*, 15164-15173.

151. Liu, H.; Shi, X.; Xu, F.; Zhang, L.; Zhang, W.; Chen, L.; Li, Q.; Uher, C.; Day, T.; Snyder, G. J., Copper ion liquid-like thermoelectrics. *Nat Mater* **2012**, *11*, 422-425.

152. Liu, X.; Wang, X.; Zhou, B.; Law, W.-C.; Cartwright, A. N.; Swihart, M. T., Size-Controlled Synthesis of Cu_{2-x}E (E = S, Se) Nanocrystals with Strong Tunable Near-Infrared Localized Surface Plasmon Resonance and High Conductivity in Thin Films. *Adv Funct Mater* **2013**, *23*, 1256-1264.

153. Miller, T. A.; Wittenberg, J. S.; Wen, H.; Connor, S.; Cui, Y.; Lindenberg, A. M., The mechanism of ultrafast structural switching in superionic copper (I) sulphide nanocrystals. *Nat Commun* **2013**, *4*, 1369.

154. Korala, L.; McGoffin, J. T.; Prieto, A. L., Enhanced Conductivity in CZTS/Cu_(2-x)Se Nanocrystal Thin Films: Growth of a Conductive Shell. *ACS Appl Mater Interfaces* **2016**, *8*, 4911-7.

155. Wolf, A.; Kodanek, T.; Dorfs, D., Tuning the LSPR in copper chalcogenide nanoparticles by cation intercalation, cation exchange and metal growth. *Nanoscale* **2015**, *7*, 19519-27.

156. Marbella, L. E.; Gan, X. Y.; Kaseman, D. C.; Millstone, J. E., Correlating Carrier Density and Emergent Plasmonic Features in Cu_{2-x}Se Nanoparticles. *Nano Lett* **2017**, *17*, 2414-2419.

157. Balitskii, O. A.; Sytnyk, M.; Stangl, J.; Primetzhofer, D.; Groiss, H.; Heiss, W., Tuning the localized surface plasmon resonance in Cu_(2-x)Se nanocrystals by postsynthetic ligand exchange. *ACS Appl Mater Interfaces* **2014**, *6*, 17770-5.

158. Jain, P. K.; Manthiram, K.; Engel, J. H.; White, S. L.; Faucheaux, J. A.; Alivisatos, A. P., Doped nanocrystals as plasmonic probes of redox chemistry. *Angew Chem* **2013**, *52*, 13671-5.
159. White, S. L.; Banerjee, P.; Jain, P. K., Liquid-like cationic sub-lattice in copper selenide clusters. *Nat Commun* **2017**, *8*, 14514.
160. Cheng, J.; Jia, H.; Lei, Y.; Liu, S.; Gao, Y.; Hou, H.; Zheng, Z., A facile room temperature route to ternary $\text{Cu}_7.2\text{S}_2\text{Se}_2$ compounds and their photovoltaic properties based on elemental copper. *Mater Chem Phys* **2017**, *193*, 267-273.
161. Ozel, F.; Sarilmaz, A.; Istanbulu, B.; Aljabour, A.; Kus, M.; Sonmezoglu, S., Pentenary chalcogenides nanocrystals as catalytic materials for efficient counter electrodes in dye-synthesized solar cells. *Sci Rep* **2016**, *6*, 29207.
162. Li, W. L.; Zou, H. Y.; Lan, J.; Wang, Q.; Li, Y. F.; Huang, C. Z., H_2S bubbles-assisted synthesis of hollow $\text{Cu}_{2-x}\text{Se}_y\text{S}_{1-y}$ /reduced graphene oxide nanocomposites with tunable compositions and localized surface plasmon resonance. *RSC Adv* **2015**, *5*, 91206-91212.
163. Elimelech, O.; Liu, J.; Plonka, A. M.; Frenkel, A. I.; Banin, U., Size Dependence of Doping by a Vacancy Formation Reaction in Copper Sulfide Nanocrystals. *Angew Chem* **2017**, *56*, 10335-10340.
164. Lin, Z. Y.; He, Q. Y.; Yin, A. X.; Xu, Y. X.; Wang, C.; Ding, M. N.; Cheng, H. C.; Papandrea, B.; Huang, Y.; Duan, X. F., Cosolvent Approach for Solution-Processable Electronic Thin Films. *Acs Nano* **2015**, *9*, 4398-4405.
165. Bekenstein, Y.; Vinokurov, K.; Keren-Zur, S.; Hadar, I.; Schilt, Y.; Raviv, U.; Millo, O.; Banin, U., Thermal doping by vacancy formation in copper sulfide nanocrystal arrays. *Nano Lett* **2014**, *14*, 1349-53.
166. Brewer, A. S.; Arnold, M. S., Field-effect measurements of mobility and carrier concentration of Cu_2S colloidal quantum dot thin films after ligand exchange. *Thin Solid Films* **2014**, *567*, 91-95.
167. Liu, L.; Liu, C.; Fu, W.; Deng, L.; Zhong, H., Phase Transformations of Copper Sulfide Nanocrystals: Towards Highly Efficient Quantum-Dot-Sensitized Solar Cells. *Chemphyschem* **2016**, *17*, 771-6.
168. Shen, H.; Wang, H.; Yuan, H.; Ma, L.; Li, L. S., Size-, shape-, and assembly-controlled synthesis of Cu_{2-x}Se nanocrystals via a non-injection phosphine-free colloidal method. *CrystEngComm* **2012**, *14*, 555-560.

169. Jiang, Z., GIXSGUI: a MATLAB toolbox for grazing-incidence X-ray scattering data visualization and reduction, and indexing of buried three-dimensional periodic nanostructured films. *J Appl Crystallogr* **2015**, *48*, 917-926.
170. Filippo, E.; Manno, D.; Serra, A., Synthesis and growth mechanism of dendritic Cu₂-xSe microstructures. *J Alloy Compd* **2012**, *538*, 8-10.
171. Ishii, M.; Shibata, K.; Nozaki, H., Anion Distributions and Phase-Transitions in Cu_{1-x}Sex(X = 0-1) Studied by Raman-Spectroscopy. *J Solid State Chem* **1993**, *105*, 504-511.
172. Kotz, R.; Yeager, E., Raman-Spectroscopy of Cobalt Phthalocyanine Adsorbed on a Silver Electrode. *J Electroanal Chem* **1980**, *113*, 113-125.
173. Scheele, M., To Be or not to Be: Band-Like Transport in Quantum Dot Solids. *Z Phys Chem* **2015**, *229*, 167-178.
174. Hull, S., Superionics: crystal structures and conduction processes. *Rep Prog Phys* **2004**, *67*, 1233-1314.
175. Gao, F.; Leng, S. L.; Zhu, Z.; Li, X. J.; Hu, X.; Song, H. Z., Preparation and Thermoelectric Properties of Cu₂Se Hot-Pressed from Hydrothermal Synthesis Nanopowders. *J Electron Mater* **2018**, *47*, 2454-2460.
176. Geetha, G.; Priya, M.; Sagadevan, S., Investigation of the Optical and Electrical Properties of Tin Sulfide Thin Films. *Chalcogenide Lett* **2015**, *12*, 609-617.
177. Boles, M. A.; Engel, M.; Talapin, D. V., Self-Assembly of Colloidal Nanocrystals: From Intricate Structures to Functional Materials. *Chem Rev* **2016**, *116*, 11220-11289.
178. Brunner, J.; Baburin, I. A.; Sturm, S.; Kvashnina, K.; Rossberg, A.; Pietsch, T.; Andreev, S.; Sturm, E.; Colfen, H., Self-Assembled Magnetite Mesocrystalline Films: Toward Structural Evolution from 2D to 3D Superlattices. *Adv Mater Interfaces* **2017**, *4*, 1.
179. Geuchies, J. J.; van Overbeek, C.; Evers, W. H.; Goris, B.; de Backer, A.; Gantapara, A. P.; Rabouw, F. T.; Hilhorst, J.; Peters, J. L.; Konovalov, O.; Petukhov, A. V.; Dijkstra, M.; Siebbeles, L. D. A.; van Aert, S.; Bals, S.; Vanmaekelbergh, D., In situ study of the formation mechanism of two-dimensional superlattices from PbSe nanocrystals. *Nat Mater* **2016**, *15*, 1248-1254.
180. Paik, T.; Ko, D. K.; Gordon, T. R.; Doan-Nguyen, V.; Murray, C. B., Studies of Liquid Crystalline Self-Assembly of GdF₃ Nanoplates by In-Plane, Out-of-Plane SAXS. *Acc Nano* **2011**, *5*, 8322-8330.
181. Rabani, E.; Reichman, D. R.; Geissler, P. L.; Brus, L. E., Drying-mediated self-assembly of nanoparticles. *Nature* **2003**, *426*, 271-274.

182. Smilgies, D. M.; Heitsch, A. T.; Korgel, B. A., Stacking of Hexagonal Nanocrystal Layers during Langmuir-Blodgett Deposition. *J Phys Chem B* **2012**, *116*, 6017-6026.
183. Vanmaekelbergh, D., Self-assembly of colloidal nanocrystals as route to novel classes of nanostructured materials. *Nano Today* **2011**, *6*, 419-437.
184. Bian, K. F.; Li, R. P.; Fan, H. Y., Controlled Self-Assembly and Tuning of Large PbS Nanoparticle Supercrystals. *Chem Mater* **2018**, *30*, 6788-6793.
185. Weidman, M. C.; Nguyen, Q.; Smilgies, D. M.; Tisdale, W. A., Impact of Size Dispersity, Ligand Coverage, and Ligand Length on the Structure of PbS Nanocrystal Superlattices. *Chem Mater* **2018**, *30*, 807-816.
186. Wenger, W. N.; Bates, F. S.; Aydile, E. S., Functionalization of Cadmium Selenide Quantum Dots with Poly(ethylene glycol): Ligand Exchange, Surface Coverage, and Dispersion Stability. *Langmuir* **2017**, *33*, 8239-8245.
187. Whitham, K.; Smilgies, D. M.; Hanrath, T., Entropic, Enthalpic, and Kinetic Aspects of Interfacial Nanocrystal Superlattice Assembly and Attachment. *Chem Mater* **2018**, *30*, 54-63.
188. Jones, M. R.; Macfarlane, R. J.; Prigodich, A. E.; Patel, P. C.; Mirkin, C. A., Nanoparticle Shape Anisotropy Dictates the Collective Behavior of Surface-Bound Ligands. *J Am Chem Soc* **2011**, *133*, 18865-18869.
189. Kan, S.; Mokari, T.; Rothenberg, E.; Banin, U., Synthesis and size-dependent properties of zinc-blende semiconductor quantum rods. *Nat Mater* **2003**, *2*, 155-158.
190. Sigman, M. B.; Ghezelbash, A.; Hanrath, T.; Saunders, A. E.; Lee, F.; Korgel, B. A., Solventless synthesis of monodisperse Cu₂S nanorods, nanodisks, and nanoplatelets. *J Am Chem Soc* **2003**, *125*, 16050-16057.
191. Tate, M. P.; Urade, V. N.; Kowalski, J. D.; Wei, T. C.; Hamilton, B. D.; Eggiman, B. W.; Hillhouse, H. W., Simulation and interpretation of 2D diffraction patterns from self-assembled nanostructured films at arbitrary angles of incidence: From grazing incidence (above the critical angle) to transmission perpendicular to the substrate. *J Phys Chem B* **2006**, *110*, 9882-9892.
192. Sinha, S. K.; Sirota, E. B.; Garoff, S.; Stanley, H. B., X-Ray and Neutron-Scattering from Rough Surfaces. *Phys Rev B* **1988**, *38*, 2297-2311.
193. Imadadulla, M.; Nemakal, M.; Sannegowda, L. K., Solvent dependent dispersion behaviour of macrocycle stabilized cobalt nanoparticles and their applications. *New J Chem* **2018**, *42*, 11364-11372.

194. Saunders, A. E.; Ghezelbash, A.; Smilgies, D. M.; Sigman, M. B.; Korgel, B. A., Columnar self-assembly of colloidal nanodisks. *Nano Lett* **2006**, *6*, 2959-2963.
195. Sanyal, M. K.; Sinha, S. K.; Huang, K. G.; Ocko, B. M., X-Ray-Scattering Study of Capillary-Wave Fluctuations at a Liquid Surface. *Phys Rev Lett* **1991**, *66*, 628-631.
196. Bresme, F.; Oettel, M., Nanoparticles at fluid interfaces. *J Phys-Condens Mat* **2007**, *19*, 41.
197. Seeck, O. H.; Deiter, C.; Pflaum, K.; Bertam, F.; Beerlink, A.; Franz, H.; Horbach, J.; Schulte-Schrepping, H.; Murphy, B. M.; Greve, M.; Magnussen, O., The high-resolution diffraction beamline P08 at PETRA III. *J Synchrotron Radiat* **2012**, *19*, 30-38.
198. Murphy, B. M.; Greve, M.; Runge, B.; Koops, C. T.; Elsen, A.; Stettner, J.; Seeck, O. H.; Magnussen, O. M., A novel X-ray diffractometer for studies of liquid-liquid interfaces. *J Synchrotron Radiat* **2014**, *21*, 45-56.
199. Murphy, B. M.; Greve, M.; Runge, B.; Koops, C. T.; Elsen, A.; Stettner, J.; Seeck, O. H.; Magnussen, O. M., A new Diffractometer for Studies of Liquid - Liquid Interfaces. *Aip Conf Proc* **2010**, *1234*, 155.